LANCASTER UNIVERSITY

Exploiting quantum paraelectricity for advancing cryogenic quantum measurements

---

by

Deepanjan Das, MSc

This thesis is submitted in partial fulfilment of the requirements for the degree of Doctor of Philosophy

in the

Faculty of Science and Technology
Department of Physics

July, 2025

Exploiting quantum paraelectricity for advancing cryogenic quantum measurements

Deepanjan Das

Abstract

Over a few decades, superconducting quantum devices have been at the forefront of many advanced research and technologies in various disciplines such as quantum computing and communication, high precision measurements, quantum information processing and metrology, quantum sensing, detection techniques, and so on. Although there has always been continuous endeavour to improve the readout signal from these sensitive quantum devices, there are still many issues to be solved. Signal power loss due to impedance mismatch along the readout line is one of them. Another is that a very weak signal always requires amplification with least thermal noise to be detected at room temperature equipment. Therefore, developing a novel ultra-low noise cryogenic amplifier which can work in the presence of a strong magnetic field, would be beneficial in advancing existing cryo-measurement setups.

The work presented in this thesis explores the potential of quantum paraelectricity to improve the quality of radio-frequency (rf) and microwave measurements at low temperatures. The quantum paraelectricity has been studied by characterising an on-chip variable capacitor on top of a quantum paraelectric material (i.e. strontium titanate and potassium tantalate). The initial study gives us an overview of its dielectric nature in the presence of an external electric field in a cryogenic environment ($\sim$ 10 mK). After that, the material has been used to develop a lumped element based impedance matching network that can be incorporated into a readout line for rf and microwave measurements in a dry dilution refrigerator. The inherent non-linearity has also been exploited through wave mixing techniques in order to discover its ability towards parametric amplification.

Acknowledgements

The completion of this thesis would not have been possible without the support of an incredible group of individuals. I would like to take this opportunity to express my heartfelt gratitude to each of them.

First, I would like to thank my supervisor, Prof. Edward Laird, for granting me the opportunity to join the world-class Ultra-Low Temperatures group at Lancaster University and for providing an exceptionally productive working environment. Edward has patiently guided me through numerous aspects of quantum science, from operating a dilution refrigerator to exploring dark matter detection techniques. His unwavering support has been invaluable and has helped me overcome many challenges throughout my Ph.D. journey. I also thank Prof. Yuri Pashkin and Dr. Sergey Kafanov for many helpful scientific discussions and offering me great advice from time to time.

I must thank Dr. Ed Romans and his group in UCL for their help in device fabrication. A big thank you to Garry for keeping the cleanroom in excellent working condition. I have greatly benefited from the support provided by the electrical and mechanical workshops.

A huge thank you to Patrick for always helping me with all lab-related issues and for insightful discussions that greatly contributed to my understanding of the experiments. Special thanks to Sam and George, whose companionship was a constant source of encouragement and I truly appreciate the fun activities we shared, including climbing, camping, cycling, running, and more. I also thank Matthew, Saba, Searbhan, and Scott for making the lab environment more enjoyable and collaborative. My heartfelt thanks go to Kranti di, Pavel da, Kaushik da, Rupa di, and Ranjita di, whose warmth and kindness made me feel at home, even when I was away from home.

Above all, I am incredibly grateful to my parents and Amrita for their belief in me and for always being there, no matter the circumstances. I could not have reached this point without your love, understanding and unconditional support.

Declaration

I hereby declare that unless explicitly acknowledged, the research work presented in this thesis is solely the author's own work and has not been submitted either wholly or partially, for the award of a higher degree at this or any other university. This thesis does not exceed the maximum permitted word length of 80,000 words, including appendices and footnotes, but excluding the bibliography. A rough estimate of the word count is: 20585 .

Deepanjan Das

BLANK PAGE

Contents

BLANK PAGE

Chapter 1

Introduction

In recent years, the quantum-limited parametric amplifier (PA) [1–5] has become an indispensable tool for sensitive quantum measurements at cryogenic temperatures. These ultra-low-noise amplifiers (Josephson parametric amplifier (JPA) [6–8], kinetic inductance parametric amplifier (KIPA) [9–13], and Josephson travelling wave parametric amplifier (JTWPA) [14, 15]) have the potential for fast and high-fidelity readout from a quantum device (such as qubits, quantum dots, etc.) [16–18] operating at ultra-low temperatures. This type of amplifier is superior to a state-of-the-art commercially available semiconducting low-noise microwave amplifier for two reasons.

1. Unlike a semiconducting amplifier, a superconducting PA can be integrated on-chip with quantum devices and can operate with near-zero power dissipation at millikelvin temperatures. Thus, a PA can be used to avoid cable losses and noise in between the device and the amplifier stage.

2. The noise temperature (which plays a vital role in determining the fidelity of the measurement) of the superconducting PA is very low. This allows the device to operate near the standard quantum limit (SQL).

However, a significant drawback of the Josephson junction (JJ) based amplifier is that it cannot function in the presence of a high magnetic field as the external magnetic flux interferes with the nonlinear inductance of the JJ. Recently, a KITWPA (kinetic inductance travelling wave parametric amplifier) [19] has shown a remarkable improvement in this context.

1.1 Research motive

Eliminating the issue of the detection of an extremely weak signal could potentially help to solve one of the greatest challenges in physics, the identification of dark matter [20–23]. Assuming that dark matter is made of axions, it can be detected with the help of an ultra-low noise parametric amplifier in the following way. In a strong magnetic field, axions decay into photons, resulting in an extremely weak electromagnetic signal. To measure such a tiny signal, a low-noise amplifier which can be operated in an external magnetic field, is highly desirable to meet the SQL. This experiment [QSHS] is a step towards identifying dark matter.

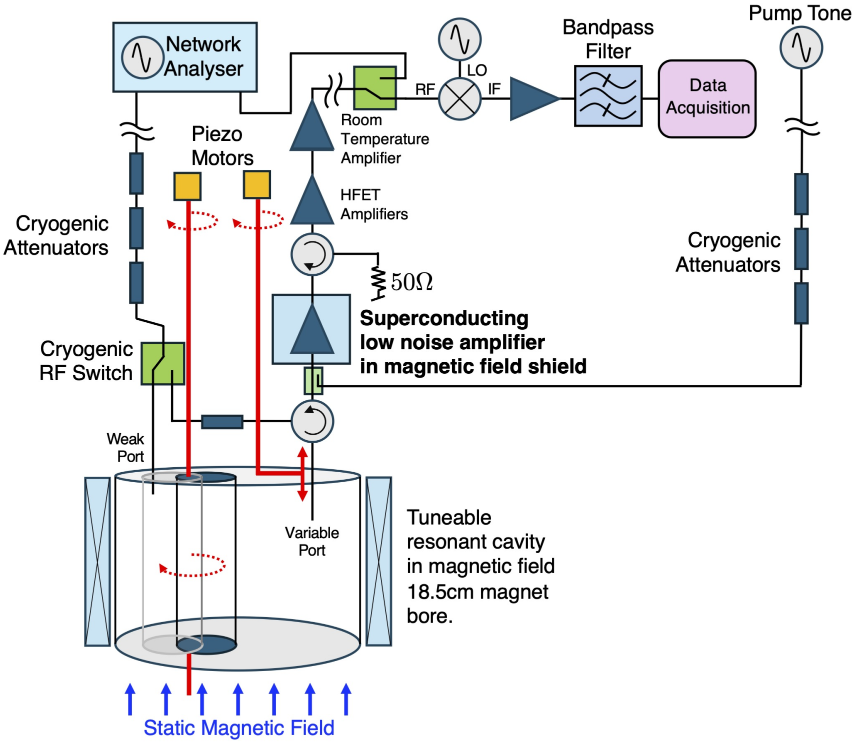

Figure 1.1: Schematic of the experimental setup for axion detection. The resonance frequency of the cavity can be tuned by changing the position of a tuning rod inside the cavity. Figure reproduced from [24] with author's consent.

Figure 1.1 shows the experimental setup, where the signal-receiving electronics are connected to a resonant cavity maintained at the base temperature (below 10 mK) of a dry dilution refrigerator. The cavity's resonance frequency is tunable via a rod controlled by a piezoelectric motor mounted on the 4 K stage. A superconducting magnet surrounds the cavity, providing a strong external magnetic field. In this field, axions can convert into photons via the axion–photon coupling. When the photon frequency matches the cavity's resonance, a signal is generated and collected by an antenna (indicated as the variable port in figure 1.1). This signal is first amplified by a superconducting low-noise amplifier at 10 mK. Additional amplification stages at higher temperatures further improve the signal-to-noise ratio (SNR), enabling detection with room-temperature electronics.

Since the superconducting low-noise amplifier is located in proximity to the external magnetic field, it is essential that it operates reliably within this field while still achieving performance at the SQL. This motivates me to conduct research on developing a new kind of amplifier where instead of a nonlinear inductor, a nonlinear capacitor can be a driving factor towards amplification which cannot be affected by an external magnetic field. In this regard, a quantum paraelectric material [25–27] could be the best fit due to its nonlinear permittivity at cryogenic temperatures.

The research presented in this thesis is a novel approach to using a quantum paraelectric medium in the development of a parametric amplifier. Initially, the cryogenic properties of this quantum paraelectric material were studied to comprehend the underlying physics behind the nonlinear behaviour of the medium. The investigation is extended further to the design of an impedance matching device [28–32], which is essential for any measurement readout system to prevent power loss in the output signal caused by impedance mismatch. Finally, the nonlinearity of the quantum paraelectric medium is assessed for the parametric wave mixing process by probing a superconducting resonator. Thus, this research work is inspired to harness quantum paraelectricity for the advancement of cryogenic quantum experiments.

1.2 Thesis layout

This thesis describes a thorough investigation of quantum paraelectricity in a cryogenic environment. The dielectric response and microwave properties of quantum paraelectric materials [strontium titanate ($SrTiO_3$) and potassium tantalate ($KTaO_3$)] have been studied to utilise them for developing a novel cryo-setup for radio frequency (rf) and microwave applications of sensitive quantum systems.

Chapter 2 contains the principle of impedance matching, an introduction to quantum paraelectricity, and the fundamentals of wave mixing in a nonlinear medium (including parametric amplification).

A detailed electrostatic study of the quantum paraelectric material is presented in chapter 3. Characterisation is performed through a concentric planar capacitor made on top of the $SrTiO_3$ chip. The impact of temperature and external electric field on the dielectric nature of this material has been demonstrated in this chapter.

The evolution of a lumped element impedance matching device is described in chapter 4. This chapter contains the simulation and experimental results of impedance matching devices of different generations.

Chapter 5 focuses on exploring the nonlinearity of this material for wave mixing processes. In this chapter a four-wave mixing scheme in a half-wave superconducting coplanar waveguide resonator based on $KTaO_3$ is studied.

The discussion in chapter 6 is oriented toward the future improvement of a superconducting resonator design on a quantum paraelectric material to characterise it as a parametric amplifier working in a three-wave mixing regime.

Chapter 2

Literature review

In this thesis, mainly the two key problems associated with the reading of signals from quantum systems that are sensitive to background noise along with cryogenic measurement setups will be addressed. An ideal measuring unit has zero power loss and the highest gain along the output line to detect an extremely weak signal originated at low temperatures, with room-temperature equipment with high background noise. Here, I address three challenges that will benefit from high-fidelity readout.

1. Reading out a qubit via its quantum capacitance often suffers from impedance mismatch, which can be eliminated by integrating a matching circuit into the readout line. Moreover, to study the quantum state of these qubits requires a fast and high-fidelity readout, which has been shown to be possible with the help of a quantum limited parametric amplifier.

2. Searching for axions via their photon emissions in the presence of a high magnetic field demands a novel cryo-setup including a lossless readout line and an ultra-low noise amplification chain with high gain. The conventional parametric amplifiers based on the Josephson junction (JJ) cannot be used in this context, as they are not feasible to operate in an external magnetic field.

3. Cryogenic characterisation of nanomechanical devices based on carbon nan-

otubes (CNTs) also requires impedance matching for maximum signal propagation and a high-gain amplification for enhancing the signal-to-noise ratio (SNR).

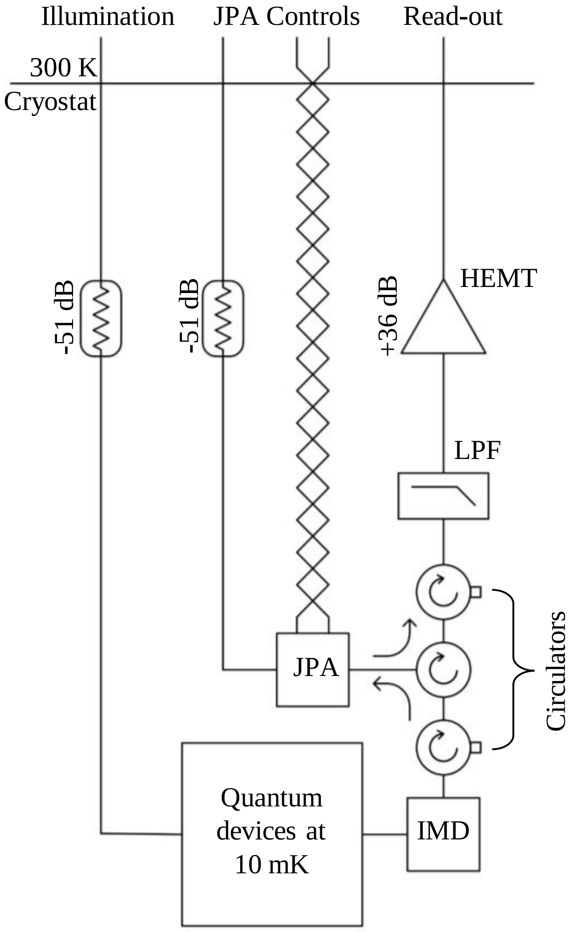

Figure 2.1: Schematic of a cryogenic measurement setup equipped with a JPA (Josephson parametric amplifier) and an IMD (impedance matching device). LPF: low-pass filter, HEMT: high electron mobility transistor amplifier

In order to develop a novel cryogenic setup (figure 2.1), I would first like to give a brief overview of impedance matching networks. Then the next section discusses how the quantum paraelectricity plays a role in making a matching circuit along with a description of its cryogenic properties. This chapter ends with a review of wave mixing and parametric amplification which is another possible application of quantum paraelectric materials.

Go to Contents↑

2.1 Impedance matching

In this section, the basic concept of impedance matching is illustrated along with its importance in the field of radio-frequency (rf) and microwave engineering. I will discuss different types of impedance matching networks [33] in different implementations. The matching network [28–32] is placed between a load impedance and a transmission line to avoid unnecessary loss of signal power by eliminating reflections between unmatched segments of an electrical circuit. This network can ideally give a perfect match (zero reflection) at a single frequency. The importance of this matching network can be realised by the following points:

1. The impedance matching network enables the circuit to provide the maximum power to the load.
2. This could potentially reduce the amplitude and phase errors of the signal.

There are several ways to design an impedance matching network depending on the complexity, bandwidth, implementation, and adjustability. In this section, I will explicitly discuss the matching networks with lumped elements (L-networks), while giving brief overviews on other types of matching networks.

2.1.1 Matching with lumped elements (L-networks)

Probably the simplest form of a matching network is based on lumped elements, where two reactive elements are used to match an arbitrary load impedance (Z_{L}) to a transmission line. This matching configuration consists of a series reactance (jX_1) and a shunt reactance (jX_2) as shown in figure 2.2. The shunt element is generally placed in parallel with the load impedance.

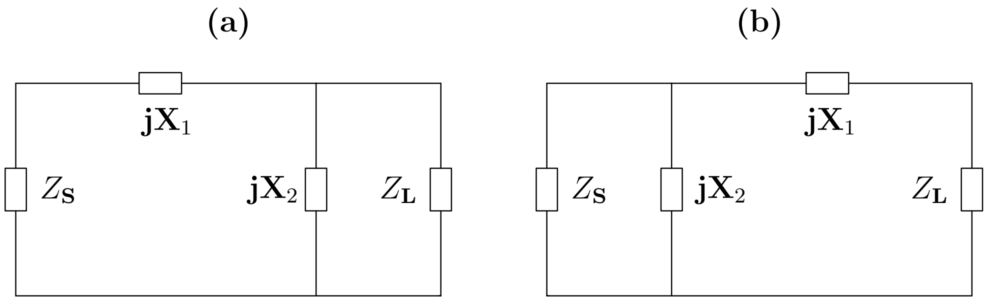

Figure 2.2: (a) L-section Type-A, (b) L-section Type-B matching networks between a source impedance (Z_S) and a load impedance (Z_L).

In either of the configurations, the reactive elements can be inductors (L) or capacitors (C). If the series component is a capacitor and the parallel component is an inductor, it is a high pass configuration, as shown in figure 2.3a. In the low-pass configuration, a shunt capacitor is used as a short at high frequency as shown in figure 2.3b.

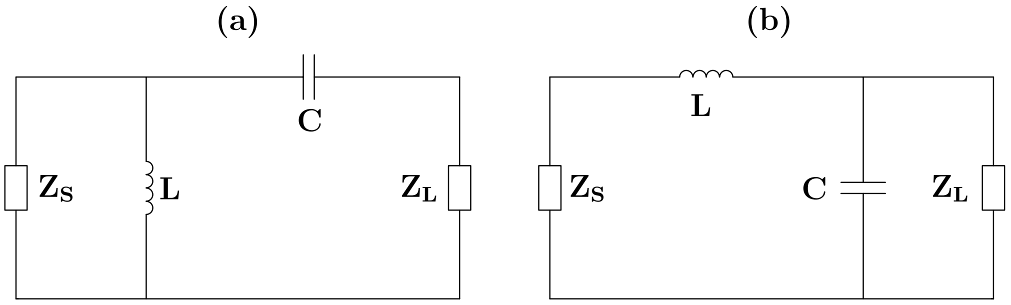

Figure 2.3: (a) High pass configuration, (b) Low pass configuration

Matching network for a resistive source (R_S) and a resistive load (R_L): Maximum power transfer from the source to the load can only be ensured when $R_S = R_L$. To make it possible, a matching network can be placed as shown in figure 2.4. The matching of the two resistive elements using only reactive elements can be done in the following way:

1. Place the right reactance (jX_2) in parallel with R_L so that the real (resistive) part of the combination ($jX_2 || R_L$) is equal to R_S.

2. Place an equal but opposite (in sign) reactive element jX_1 in series to cancel

out the imaginary (reactive) part of the combination ($jX_2||R_L$).

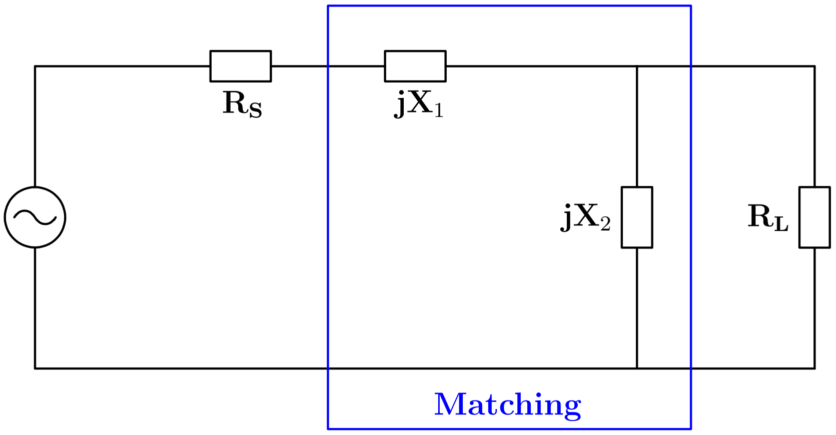

Figure 2.4: Matching network for resistive circuit

L-section matching for a complex source and load: As shown in figure 2.2, we have two different network configurations to match the complex load Z_L with the characteristic impedance Z_0 of the system. The choice of configuration depends on the resistive part of the load (R_L) and the characteristic impedance (Z_0).

If $R_L > Z_0$: Type-A L-section (the shunt element is next to the load)

If $R_L < Z_0$: Type-B L-section (the shunt element is next to the source)

2.1.2 Other techniques for impedance matching

In this section I will briefly discuss different techniques for impedance matching for different cases.

Single-stub tuning is a popular matching technique to avoid lumped elements, since this uses a single open-circuited or short-circuited length of a transmission line (called a stub). In this technique, the two tuning parameters are the distance between the stub and the load, and the length of the stub section (since the susceptance or reactance depends on the stub length). Depending on the connection of this stub with the transmission feed line, there are **shunt stub** (where the stub is connected in parallel with the feed line) and **series stub** (where the stub is connected in series with the feed line). Shunt stubs are preferred for the microstrip line or strip-line, while series stubs are preferred for slotline or coplanar waveguide.

Double-stub tuning is another way to perfect impedance matching where two tuning stubs are used in fixed positions and the load could be at an arbitrary distance from the first stub. This technique overcomes the disadvantage of the single-stub tuner, which requires a variable length of line between the load and the stub if an adjustable tuner is expected.

The quarter-wave transformer is used to match a real load impedance to a transmission line. If impedance matching is required only for a very narrow bandwidth, a single section of this transformer may be sufficient. For applications demanding a broader bandwidth, it can be extended to a multi-section transformer. The working principle of this kind of transformer is based on the theory of small reflections [34]. There are binomial and Chebyshev multisection matching transformers available in the field of impedance matching techniques. The binomial transformers are used for a gradual impedance matching with very minimal ripple in the passband while the Chebyshev transformers allow for ripple in the passband for faster and steeper transition between impedance levels.

Another unique way to match an arbitrary real load impedance to a transmission line over an expected bandwidth is the application of **Tapered lines**. There are several types of taper, such as exponential taper, triangular taper, and Klopfenstein taper [35, 36]. Among them, the Klopfenstein impedance taper is arguably the best in terms of the optimum reflection coefficient over the passband.

To develop an L-section matching network, the choice of the right reactive element is very crucial. In this regard, a dielectric material can be introduced to make a reactive element (such as a capacitor). The following section focuses on finding the right material for this purpose.

2.2 Quantum paraelectricity

Dielectric materials can be classified into ferroelectric, paraelectric, and quantum paraelectric, based on their behaviour under the influence of an external electric field and their ability to exhibit spontaneous polarisation.

- Ferroelectric materials exhibit spontaneous polarisation even in the absence of an external electric field, which means that the electric dipoles are naturally aligned in a particular orientation. However, the polarisation can be reversed by applying an external electric field. Moreover, the material shows a hysteric response since the polarisation depends on the history of the applied field.

- On the other hand, paralectric materials do not exhibit spontaneous polarisation at zero field. But they become polarised under the influence of an external electric field, and the polarisation disappears upon the removal of the field. Unlike ferroelectric materials, the paraelectric materials do not show hysteresis.

- As a special class, the quantum paraelectric material unveils its characteristics only at low temperatures. The cryogenic study of these quantum materials near a quantum critical point has led to intriguing research in condensed matter physics. Quantum paraelectric materials (such as $SrTiO_3$, $KTaO_3$) are arguably one of the most studied materials of the perovskite family [25–27]. In this material, the development of spontaneous polarisation is suppressed by quantum fluctuations [27], which prevent the material from being ferroelectric even near the phase transition temperature. This phase transition temperature is known as Curie temperature (T_0) which defines the boundary between ferroelectricity and paraelectricity. Above T_0, ferroelectric materials become paraelectric in nature. These incipient ferroelectric materials are characterised by high dielectric susceptibility [37] at low temperatures, which does not quite follow the classical Curie behaviour below a few tens of kelvin [38, 39]. The ferroelectric state can be achieved with external perturbations such as pressure, oxygen isotope substitution [40, 41] and strain [42].

Due to their exceptionally high susceptibility, quantum paraelectric materials appear to be well suited as the foundation of the reactive elements in the matching networks. However, further research is needed to properly evaluate their potential.

2.2.1 Paraelectric phase transitions

During the last few decades, careful measurements of the dielectric constants of strontium titanate ($SrTiO_3$) and potassium tantalate ($KTaO_3$) were made at different temperatures between 325 K and 4 K to determine the most appropriate classical or quantum model which fit the experimental data to explain ferroelectric phase transitions at low temperatures. This section is mainly about the evolution of the models [43] to explain the phase transition.

A classical model, known as the Curie-Weiss formula, was initially used to explain the phase transitions. The formula of the dielectric constant (ϵ) can be described as follows:

$$\epsilon = C/(T - T_0) + \epsilon_0 \tag{2.1}$$

where C is the Curie constant, T_0 is the Curie temperature, T is the sample temperature, and ϵ_0 is a temperature-independent constant that was not included in the original formula. In 1952, Barrett [43] modified the classical model by introducing a quantum-mechanical treatment of ionic polarizability in the following way.

$$\epsilon(T) = \frac{C}{(T_1/2)\coth(T_1/2T) - T_0} + \epsilon_0 \tag{2.2}$$

where, $T_1 = h\nu/k_\mathrm{B}$, where k_B is the Boltzmann constant, h is the Planck constant and $h\nu$ is the energy level difference of the harmonic part in the potential energy. In 1997 Vendik [43], introducing a measure of the density of defects and inhomogeneity, modified the model further which can be described as

$$\epsilon(T) = \frac{C/T_0}{[\sqrt{\xi^2+\eta^3}+\xi]^{2/3}+[\sqrt{\xi^2+\eta^3}-\xi]^{2/3}-\eta} + \epsilon_0 \tag{2.3}$$

where $\xi^2 = \xi_B^2 + \xi_S^2$, ξ_B is the normalized bias field, ξ_S is a measure of the density of defects and inhomogeneity, and η is a parameter directly associated with the interaction between two sublattices coupled by a nonlinear elastic interaction.

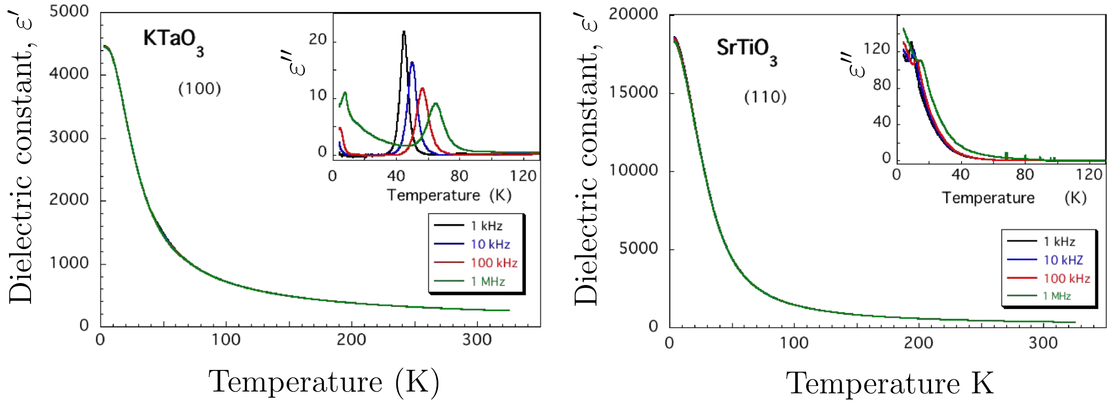

(a) (b)

Figure 2.5: Dielectric response of (a) $KTaO_3$ and (b) $SrTiO_3$. For both (a) and (b) the main plot is the real part (ε') and the inset is the imaginary part (ε'') of the dielectric constant. Figure reproduced from [43] with publisher's consent.

Figure 2.5a shows the temperature dependence of the real and imaginary dielectric constant of the $KTaO_3$ along (100). The real part (ε') increases significantly as the temperature goes below 100 K. But for the imaginary part (ε'') , there are different peaks between $\sim$ 45 K and $\sim$ 65 K which are dependent on the measured frequency. Again, it is enhanced below $\sim$ 10 K. The real part of the dielectric constant was analysed on the basis of Barrett's and Vendik's models with and without considering ξ. Introducing ξ to Vendik's formula greatly improved the fitting of the nonlinear curve, especially below 10 K. In this sense, it could be concluded that Vendik's formula can more appropriately describe the permittivity of $KTaO_3$ than Barrett's formula.

Figure 2.5b describes the impact of temperature on ε' (the real part of the dielectric constant) of $SrTiO_3$ along (110). ε'' is also plotted in the inset. Similarly to $KTaO_3$, ε' for $SrTiO_3$ also goes higher as the temperature drops below 100 K, although the highest values of that are different. From the plot below [figure 2.6], we could say that Vendik's formula with $\xi \neq 0$ fits the best to the experimental data. Significant enhancement of the imaginary dielectric constant below 20 K and small peaks between 10-20 K could be caused by a few extrinsic factors such as impurities and conditions of sample preparation or oxygen vacancies. The quantum paraelectric state of $SrTiO_3$ is stabilised by structural distortion, and if there are no distortions, $SrTiO_3$ would undergo a ferroelectric phase transition around 30 K.

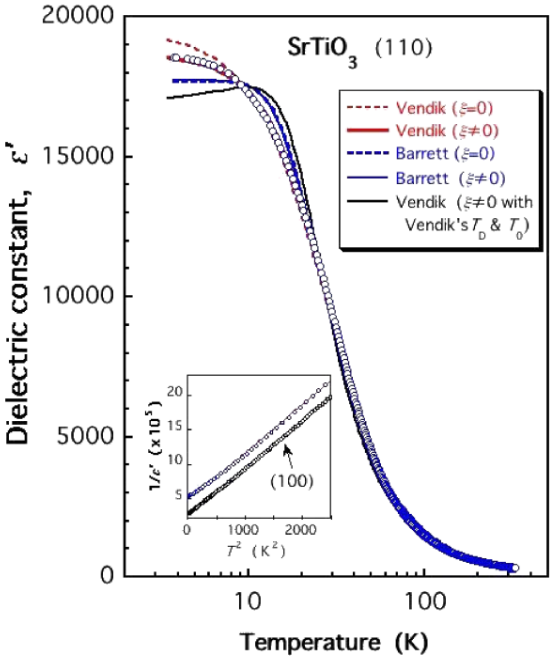

Figure 2.6: Comparison of fits between Vendik's formula and Barrett's formula to ε' of $SrTiO_3$ along (110). Figure reproduced from [43] with publisher's consent.

2.2.2 Microwave properties of the paraelectrics

The microwave dielectric properties of single-crystal quantum paraelectrics ($KTaO_3$ and $SrTiO_3$) at cryogenic temperatures are studied in order to use them in the field of low-loss tunable microwave filters. In section 2.2.1 , the discussion is mainly focused on characterising the permittivity at different temperatures. Here I am going to discuss how the loss tangent of these paraelectric materials depends on frequency and temperature.

Figure 2.7a describes the dielectric loss tangent ($\tan\delta$, defined as the ratio between the imaginary (ε'') and real part (ε') of the relative permittivity) as a function of frequency (f) at different temperatures for a highly pure single crystal $SrTiO_3$. The loss tangent generally incorporates both surface losses (originating from amorphous interfaces) and substrate losses. Figure 2.7c shows that as the temperature decreases from 300 K to 5.4 K, the loss tangent of $SrTiO_3$ initially decreases and below ~ 60 K it starts to increase again. At room temperature, the

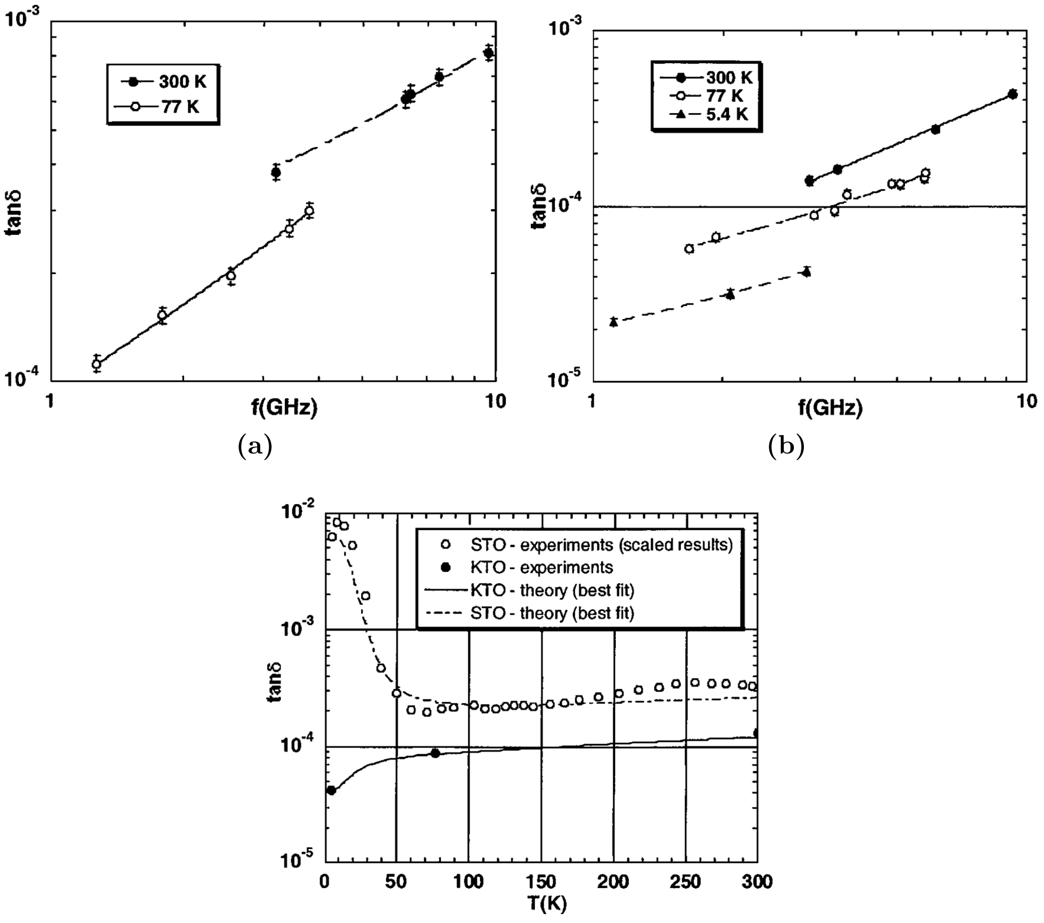

(a) (b)

(c)

Figure 2.7: (a) $\tan\delta$ vs frequency for $SrTiO_3$ at different temperatures, (b) $\tan\delta$ for $KTaO_3$, (c) Comparison between $SrTiO_3$ and $KTaO_3$. Figure reproduced from [44] with publisher's consent.

perovskite $SrTiO_3$ has a cubic structure with $a = 0.3904\,\mathrm{nm}$. A phase transition from cubic to tetragonal occurs at 110 K. At 77 K oxygen octahedra start rotating relative to the ion sublattice causing an increase in dielectric loss followed by a rhombic transition below 65 K. Another transition to the rhombohedral phase at $\sim 10\,\mathrm{K}$ explains the maximum loss around 10 K, as shown in figure 2.7c.

Figure 2.7b shows that as temperatures decrease the loss in $KTaO_3$ decreases, which implies that $KTaO_3$ does not undergo any phase transition at cryogenic temperatures. Figure 2.7c is a comparison between $SrTiO_3$ and $KTaO_3$. In general, it seems that $KTaO_3$ is a better potential candidate in the field of microwave application than $SrTiO_3$ at cryogenic temperature. Vendik gave an interpretation of the loss tangent associated to different factors [44] in a form of an equation,

$$\tan\delta = \tan\delta_1 + \tan\delta_2 + \tan\delta_3 \tag{2.4}$$

where, $\tan\delta_1$ represents the dominant loss due to multiphonon scattering of the soft ferroelectric mode, $\tan\delta_2$ and $\tan\delta_3$ are associated with the transformation of microwave electric-field oscillations into acoustic oscillations due to residual ferroelectric polarisation and charged defects respectively.

2.2.3 Electric field-dependent dielectric constant

An experimental proof [45] has shown that in the presence of an external electric field (E), the dielectric constant ($\epsilon_r^{\mathrm{STO}}$) of a single crystal $SrTiO_3$ (STO) changes as a function of E at 10 mK. The experimental data can be explained by Landau-Ginzburg-Devonshire (LGD) theory, which can be described as

$$\epsilon_r^{\mathrm{STO}}(E) = 1 + \frac{\epsilon_r^{\mathrm{STO}}(0)}{[1 + (E/E_0)^2]^{1/3}} \tag{2.5}$$

where, E_0 is a parameter related to the tunability of the dielectric constant with electric field. The dielectric response of $SrTiO_3$ is probed by a superconducting coplanar waveguide resonator fabricated on top of a $SrTiO_3$ substrate as shown in figure 2.8a. The external electric field is introduced by applying a dc voltage (V_{dc}) on the central strip-line of the resonator. The reduction of the highest value of the dielectric constant at 0 V (figure 2.8b) indicates a decrease in the polarizability of the STO. It is observed that after applying the voltage, it is difficult to restore the initial sample condition to get the same value of the dielectric constant at 0 V. In order to restore the sample, it requires a thermal cycle up to room temperature, although partial recovery is possible by applying the field polarity. The negative voltage is shown to affect the sample more than the positive voltage, which could be explained by the presence of oxygen vacancies.

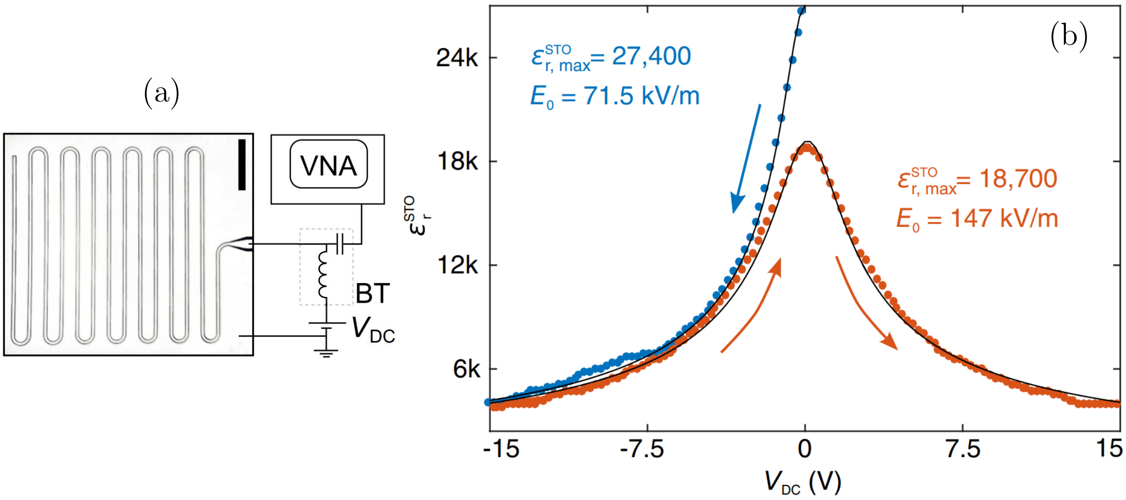

Figure 2.8: (a) Schematic of the measurement setup where the device is a $\lambda/2$ coplanar waveguide resonator. (b) Dielectric response of $SrTiO_3$ at 3.5 K to an external dc voltage (V_{dc}). Figure reproduced from [45] with publisher's consent.

The dielectric response and microwave properties of quantum paraelectric materials could possibly provide valuable insight into the wave mixing process (see below). The study then could be extended further to utilise this material as a base for parametric amplification. Due to its non-responsive nature towards external magnetic field, the parametric amplifier made from this material could potentially work even in the presence of a high magnetic field, unlike the traditional Josephson junction based parametric amplifiers. The following section covers the basics of wave mixing and how it relates to parametric amplification.

2.3 Study of parametric wave mixing and amplification

Wave mixing [46–49] has been a well established topic in the field of nonlinear optics. In this phenomenon, two or more optical waves couple with each other while interacting with the nonlinear medium and result in the generation of new waves at different frequencies. As a consequence of this phenomenon, two processes arise: sum frequency generation and difference frequency generation.

For **sum frequency generation**, two optical waves at frequencies ω_1 and ω_2 interact in a lossless nonlinear medium to produce an extra wave at frequency ω_3 which is the sum of ω_1 and ω_2. Hence, $\omega_3 = \omega_1 + \omega_2$.

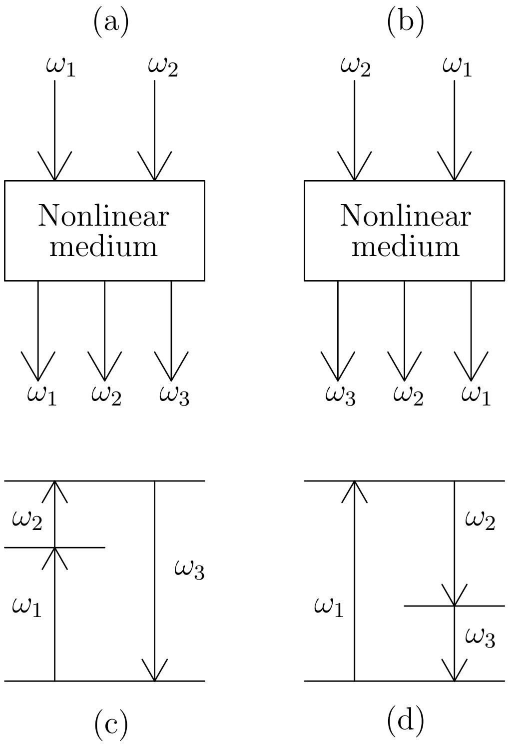

Figure 2.9: Schematic representation of nonlinear wave-mixing. (a) and (c) show the mixing scheme and the corresponding energy-level diagram for sum frequency generation. (b) and (d) show the mixing scheme and the corresponding energy-level diagram for difference frequency generation.

Similarly for **difference frequency generation**, two optical waves at frequencies ω_1 and ω_2 interact in a lossless nonlinear medium to produce an extra wave at frequency ω_3 which is the difference of ω_1 and ω_2. Hence, $\omega_3 = \omega_1 - \omega_2$. An analogy can be drawn between difference frequency generation and parametric amplification as they both share the same frequency relation.

The principle of parametric amplification could be illustrated as follows. If a medium with nonlinear polarisation is illuminated with a strong electromagnetic field (pump tone), a weak electromagnetic field gains amplification while passing through the medium. In this process, the energy of the pump tone with frequency ω_p is transferred to the signal mode with frequency ω_s resulting in the amplification of the signal and the generation of a third mode (known as the idler mode) with frequency ω_i. The amplification could be achieved through either of the following processes:

- Three-wave mixing (3WM): where three electromagnetic waves participate in a fashion where $\omega_\mathrm{p} = \omega_\mathrm{s} + \omega_\mathrm{i}$.
- Four-wave mixing (4WM): where four electromagnetic waves participate in a fashion where $2\omega_\mathrm{p} = \omega_\mathrm{s} + \omega_\mathrm{i}$.

Nonlinear Wave Mixing: Mathematical Analysis

If a nonlinear medium responds to the electric field E with a nonlinear polarisation $P(E)$ or a nonlinear voltage response, generally the response can be expressed as a Taylor series expansion:

$$P(E) = \chi^{(1)}E + \chi^{(2)}E^2 + \chi^{(3)}E^3 + \cdots$$

Here, $\chi^{(n)}$ represents the n-th order susceptibility, characterising the strength of the medium's nonlinear response at that order. The second-order term $\chi^{(2)}$ is responsible for processes like second-harmonic generation and three-wave mixing, while the third-order term $\chi^{(3)}$ governs phenomena such as four-wave mixing, self-phase modulation, and third-harmonic generation.

Wave Mixing Due to Superposed Fields: Let us consider two input waves with distinct frequencies ω_1 and ω_2:

$$V_1 = A_1 e^{i\omega_1 t}, \quad V_2 = A_2 e^{i\omega_2 t}$$

$$E(t) = V_1 + V_2$$

For materials with non-zero $\chi^{(2)}$, the superposed field contains the term,

$$|E|^2 = (V_1 + V_2)(V_1^* + V_2^*) = |V_1|^2 + |V_2|^2 + V_1 V_2^* + V_1^* V_2$$

This expansion includes:

- DC components: $|V_1|^2$, $|V_2|^2$
- Beat terms: $V_1 V_2^* = A_1 A_2^* e^{i(\omega_1 - \omega_2)t}$, and its conjugate

These generate difference frequency signals at $\omega_1 - \omega_2$ and $\omega_2 - \omega_1$, which are the basis for three-wave mixing in media with non-zero $\chi^{(2)}$.

For materials with non-zero $\chi^{(3)}$, $P(E)$ contains the component,

$$E|E|^2 = (V_1 + V_2)(|V_1|^2 + |V_2|^2 + V_1 V_2^* + V_1^* V_2)$$

Expanding yields:

$$\begin{aligned} E|E|^2 = {} & V_1|V_1|^2 + V_1|V_2|^2 + V_1^2 V_2^* + V_1 V_1^* V_2 \\ & + V_2|V_1|^2 + V_2|V_2|^2 + V_2^2 V_1^* + V_2 V_1^* V_2 \end{aligned}$$

Each of these terms gives rise to different nonlinear phenomena. For example:

- $V_1^2 V_2^*$ and $V_2^2 V_1^*$ generate frequency components at $2\omega_1 - \omega_2$ and $2\omega_2 - \omega_1$, respectively — four-wave mixing (FWM).
- $V_1|V_2|^2$ and $V_2|V_1|^2$ represent cross-phase modulation (XPM) effects.

- $|V_1|^2$ and $|V_2|^2$ contribute to a constant (DC) background.
- $V_1 V_2^*$ and $V_1^* V_2$ represent difference frequency generation (DFG).
- Higher order terms like V_1^3, V_2^3 contribute to third harmonic generation (THG) at $3\omega_1$ and $3\omega_2$.

Four-Wave Mixing (Idler Generation): In four-wave mixing (FWM), the nonlinear interaction generates a new frequency (idler) by combining two pump photons and one signal photon. For example, if $\omega_p = \omega_1$ and $\omega_s = \omega_2$, the idler frequency is: $\omega_i = 2\omega_p - \omega_s = 2\omega_1 - \omega_2$. This term arises from the cubic interaction $V_1^2 V_2^*$ and is a hallmark of coherent four-wave mixing processes in nonlinear optics.

Therefore, by expanding the electric field interaction in a nonlinear medium, we observe the emergence of various new frequencies beyond the original signals. Second-order ($\chi^{(2)}$) effects give rise to beat notes and difference frequency signals (three-wave mixing), while third-order ($\chi^{(3)}$) interactions produce rich frequency mixing including idlers, harmonics, and modulation effects (four-wave mixing).

Based on these principles, in recent years, a lot of research has been conducted for the development of a Josephson junction-based parametric amplifier. Being an ultra-low noise amplifier and meeting the standard quantum limit, this parametric amplifier has proven to be crucial in various fields of cutting edge research such as quantum computation, qubit readout [5, 16], electron spin resonance detection [50], astronomy instrumentation [51, 52], axion-like dark matter detection [20–23] and so on. Depending on the nature of the electromagnetic wave, there are two different approaches to parametric amplification that have been developed.

- Resonant parametric amplifier [2, 53–59]: The mechanism is based on a standing wave interacting with the nonlinear medium, incorporated in a cavity where the interaction time is the inverse of the cavity line width. In this way, this kind of amplifier is restricted to a very narrow amplification bandwidth. The gain is achieved when the wave is trapped inside the cavity.

- Travelling wave parametric amplifier [1, 9, 10, 14, 60–63]: The signal gains amplification while propagating through the segments of the transmission line made of nonlinear medium. The gain profile is determined by the physical length of the nonlinear medium. Although this removes the constraint of narrow bandwidth for amplification, this has other drawbacks such as signal loss due to impedance mismatch along the physical length, low saturation power, limited operating microwave frequency range (the usual range it covers is from 4 to 12 GHz, while below 1 GHz is often used for handling spin qubits [16] and frequency above 12 GHz is useful for dark matter search experiments [20]).

To achieve maximum gain, it is important to increase the interaction time between the pump, the signal, and the nonlinear medium. It is done in the following way: a linear resonator is combined with a nonlinear medium to construct a nonlinear resonator (NLR), whose resonance frequency ω_0 can be tuned by adjusting a parameter of the nonlinear medium. There are different schemes for parametric amplification relying on the evolution of signal and idler mode in the same or different spatial mode.

For the sake of simplicity, we will consider a resonant parametric amplifier working in a reflectometry setup. For both 3WM and 4WM process, there are two

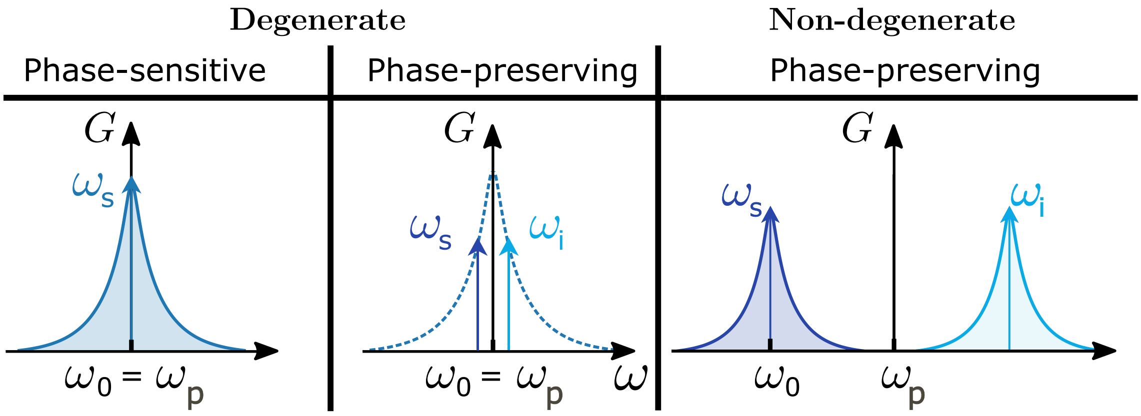

Figure 2.10: Classifications of wave mixing depending on phase sensitivity. Figure reproduced from [64] with author's consent.

modes of operation - degenerate and non-degenerate.When the idler evolves at a different frequency than the signal, the amplifier is called non-degenerate. However, in the case of a degenerate amplifier, both the signal and the idler mode evolve in the same spatial mode. Moreover, there are cases where the amplifier gain is sensitive to the phase difference between the pump and the signal. They are known as phase-sensitive and phase-preserving modes of operation. When $\omega_\mathrm{s} = \omega_\mathrm{i}$, the signal gains in a phase-sensitive way. When $\omega_\mathrm{s} \neq \omega_\mathrm{i}$, even if both the signal and the idler appear in the same spatial mode, the mode of operation is known as phase-preserving. A clear distinction can be found in figure 2.10.

Hence, to summarise, there are four different trends of parametric amplifications based on the 3WM/4WM process and the degenerate/non-degenerate state. The following sections describe the key features and implementations of all possible schemes [64].

Three-wave mixing and degenerate: This occurs when an NLR is coupled with a pump oscillator. As shown in figure 2.11, maximum amplification can be obtained when the pump frequency (ω_p) is double the NLR frequency (ω_0) and the signal frequency (ω_s) coincides with ω_0. An excellent implementation could be found in this article [65] where the Josephson parametric amplifier (JPA) [discussed in a later part of this section] is developed by embedding SQUIDs (Superconducting Quantum Interference Devices) in a resonator operating in a reflectometry setup.

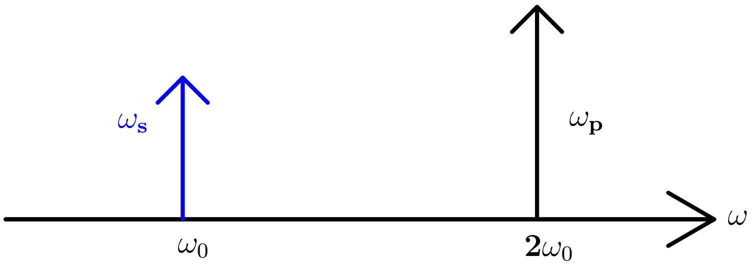

Figure 2.11: Frequency landscape of 3-wave mixing and degenerate process.

Three-wave mixing and non-degenerate: This occurs when two NLRs and a pump oscillator are coupled to each other. Maximum amplification is achieved when ω_s is closer to one NLR frequency ($\omega_{0,1}$). By satisfying the energy conservation,

$\omega_\mathrm{i} = \omega_\mathrm{p} - \omega_\mathrm{s}$, the idler mode appears in a spatially distant position from ω_s as shown in figure 2.12. This amplification scheme can be implemented in cavity quantum electrodynamics (cQED), either as a Josephson ring modulator [54, 58, 59] or as a highly asymmetric SQUID (also known as the superconducting nonlinear asymmetric inductive element (SNAIL)) [66].

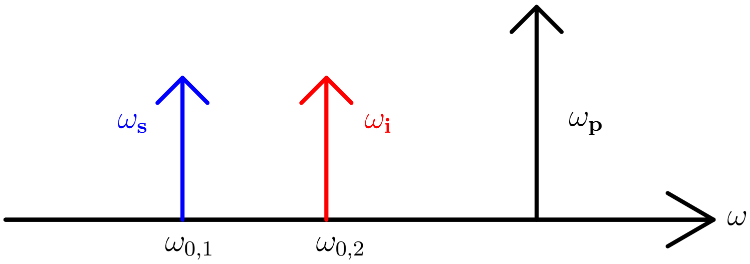

Figure 2.12: Frequency landscape of 3-wave mixing and non-degenerate process.

Four-wave mixing and degenerate: This process can be performed when an NLR is capacitively coupled to a pump oscillator. As shown in figure 2.13, the amplification occurs when ω_s and ω_p coincide with each other and are both detuned by $2K|\alpha|^2$ (where K is the Kerr coefficient that quantifies the nonlinearity and α is the pump complex amplitude) from the NLR (ω_0). A good example of this scheme is a JPA that uses fourth-order Kerr nonlinearity to drive the system to the right regime of amplification.

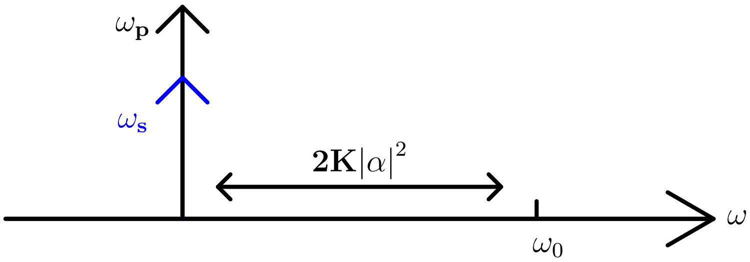

Figure 2.13: Frequency landscape of 4-wave mixing and degenerate process.

Four-wave mixing and non-degenerate: When two NLRs are capacitively coupled and a pump oscillator is also capacitively coupled to any one of the NLRs, this scheme can give amplification. The maximum amplification occurs when ω_s is detuned by $2K|\alpha|^2$ from $\omega_{0,1}$ and the energy conservation $\omega_\mathrm{s} + \omega_\mathrm{i} = 2\omega_\mathrm{p}$ is fulfilled, the idler mode appears spatially separated from ω_s by an amount of $2g_2$ (when g_2 is the coupling rate between two NLRs). Note that ω_p is also separated from ω_i by g_2. A cQED application of 4WM non-degenerate JPAs is found in references [67, 68].

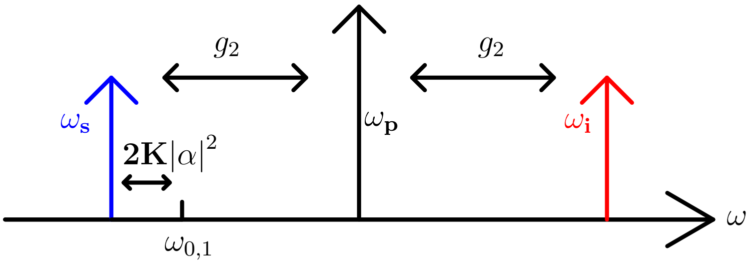

Figure 2.14: Frequency landscape of 4-wave mixing and non-degenerate process.

After discussing most possible amplification scenarios, it is evident from the frequency perspective that the three-wave mixing operation is more efficient than four-wave mixing in separating the pump and signal tones, simplifying the pump-filtering process [55].

2.3.1 Origin of nonlinearity in parametric amplifiers

Conventional and commercially available parametric amplifiers are mainly based on Josephson junctions [69] or high kinetic inductance [61]. With promising performance near the standard quantum limit [1, 70], these devices have the potential for high-fidelity and fast readout, making them an essential tool for sensitive experiments in the field of quantum information technology [71–73].

The conventional resonant parametric amplifiers, such as Josephson parametric amplifiers (JPAs) where Josephson junctions are embedded in superconducting cavities, suffer from the inherent gain-bandwidth trade-off. To overcome this issue, Josephson travelling wave parametric amplifiers (JTWPAs) [1, 14, 60, 62, 70] are introduced to allow a higher dynamic range for frequency multiplexing readout of quantum systems.

In JTWPAs, the nonlinearity comes from the Josephson inductance, $L_\mathrm{J}(I) \approx \Phi_0(1+\tilde{\gamma}I^2/I_\mathrm{C}^2)/(2\pi I_\mathrm{C})$ [where Φ_0 is the magnetic flux quantum, I_C is Josephson critical current, and $\widetilde{\gamma} = \frac{1}{6}\cos\varphi_{\mathrm{dc}}$, where φ_{dc} is the phase drop across the Josephson junction (JJ) as shown in figure 2.15] and the Josephson supercurrent, $I_{\mathrm{J}} = I_{\mathrm{C}}\sin\varphi$ [where φ is the variation of the JJ phase associated with the ac current I]. The Taylor expansion of I_{J} provides the nonlinear term ($\propto \varphi^3$). The nonlinearity introduced by the cubic term is known as Kerr nonlinearity. Due to this centrosymmetric nonlinearity [as $I_{\mathrm{J}}(-\varphi) = -I_{\mathrm{J}}(\varphi)$] of the supercurrent [in other words, symmetric nonlinearity of Josephson inductance (as $L_{\mathrm{J}}(-I) = L_{\mathrm{J}}(I)$)], JTWPAs can only be operated in four-wave mixing mode.

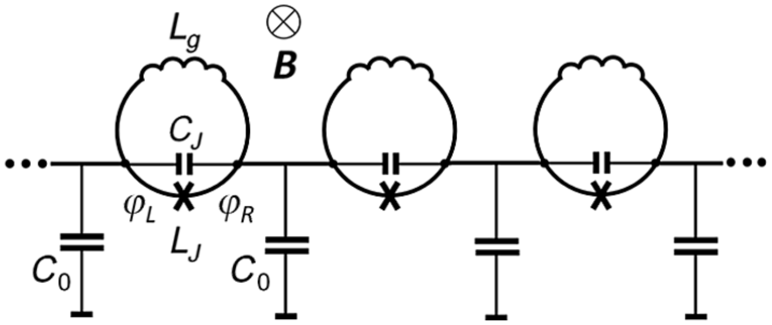

Figure 2.15: Schematic diagram of the transmission line consisting of an array of one-junction SQUIDs. Figure reproduced from [63] with publisher's consent.

In 2016, A. B. Zorin proposed a model [63] where a quadratic nonlinearity (φ^2) appears along with the Kerr nonlinearity which makes a parametric amplifier favourable for three-wave mixing mode. In this ladder type transmission line model (figure 2.15), the modified current phase relation looks like,

$$I/I_{\mathrm{C}} = (\beta_{\mathrm{L}}^{-1} + \cos\varphi_{\mathrm{dc}})\varphi - \widetilde{\beta}\varphi^2 - \widetilde{\gamma}\varphi^3 - \ldots \tag{2.6}$$

with, $\widetilde{\beta} = \frac{1}{2}\sin\varphi_{\mathrm{dc}}$, $\beta_{\mathrm{L}} \equiv 2\pi L_{\mathrm{g}} I_{\mathrm{C}}/\Phi_0$ (where L_{g} is the geometrical inductance). In equation 2.6 $\widetilde{\beta}$ and $\widetilde{\gamma}$ are associated with quadratic and cubic (Kerr) nonlinearity.

Due to the quadratic term (φ^2), the asymmetry appears (as $I(-\varphi) \neq -I(\varphi)$) allowing a number of nonlinear effects inaccessible through Kerr nonlinearity, such as second harmonic generation (SHG) [74], spontaneous parametric down conversion (SPDC) and three-wave mixing mode. In this clever way, one can have full control on both quadratic (3WM) and cubic (4WM) nonlinearity in the current phase relation.

2.3.2 A pioneering work on a resonant parametric amplifier

The limitations of the dynamic bandwidth of resonant parametric amplifiers are well recognised. Addressing this problem, scientists from NIST engineered a robust resonant mode parametric amplifier [53, 75] in 2016. The specialty of this amplifier is that it has an adjustable band center. Although the amplifier is narrow-band, by tuning the resonance frequency of the nonlinear resonator, the band center can cover a range from 4 to 7.8 GHz. This is a unique way to avoid the restriction in working bandwidth of a resonant parametric amplifier. Also, the gain does not need to be compromised, unlike a TWPA for the confinement in the gain-bandwidth product.

The device has a coplanar waveguide structure where the central conductor comprises of an array of SQUIDs in series. One end of the inner conductor is shorted to ground, while the other end is capacitively coupled with a 50 Ω matched

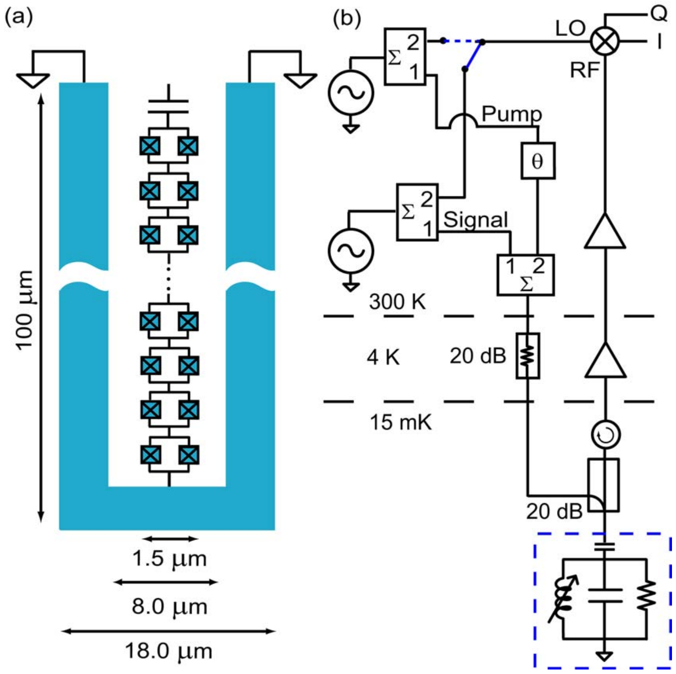

Figure 2.16: (a) Device diagram of a $\lambda/4$ superconducting coplanar resonator. The central conductor is a series array of 400 SQUIDs. (b) Simplified measurement schematic. Figure reproduced from [53] with publisher's consent.

line, constructing a quarter-wave resonator. The measurements are performed in a reflectometry fashion as shown in the figure 2.16. The nonlinearity for this device comes from the current dependent inductance of a JJ,

$$L_{\mathrm{J}}(I) = \frac{\hbar}{2eI_{\mathrm{C}}} \frac{\arcsin\left(I/I_{\mathrm{C}}\right)}{I/I_{\mathrm{C}}} \tag{2.7}$$

where I is the current flowing through the JJ and I_{C} is the critical current of the JJ. The device uses this Kerr nonlinearity to operate in a four-wave mixing regime ($\omega_{\mathrm{i}} = 2\omega_{\mathrm{p}} - \omega_{\mathrm{s}}$, where i, p, and s refer to idler, pump, and signal tone, respectively). By adjusting the flux through the SQUIDs, the inductance can be adjusted. As a consequence, the resonance frequency can be tuned by flux, as shown in figure 2.17.

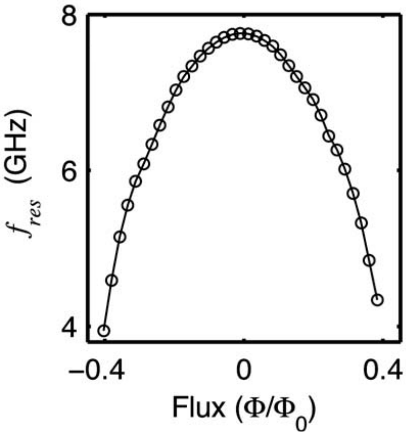

Figure 2.17: Resonance frequency as a function of flux. Figure reproduced from [53] with publisher's consent.

This widely tunable parametric amplifier has been demonstrated to work in both a non-degenerate ($\omega_{\mathrm{s}} \neq \omega_{\mathrm{p}} \neq \omega_{\mathrm{i}}$) and a doubly degenerate ($\omega_{\mathrm{s}} = \omega_{\mathrm{p}} = \omega_{i}$) mode. In the non-degenerate mode of operation, the optimum value of both the direct gain (DG, defined as the ratio between the reflected signal power with the pump on and the incident signal power) and the intermodulation gain (IG, defined as the ratio between the idler tone and the incident signal) is 18 dB with a dynamic bandwidth of 300 kHz. On the other hand, the maximum gain in a doubly degenerate state, obtained by adjusting the signal-pump phase is 28±0.2 dB.

Chapter 3

Electrostatic study of quantum paraelectric materials

In recent years, there has been a renewed interest in applications of incipient ferroelectric materials (such as single-crystal strontium titanate ($SrTiO_3$) and potassium tantalate ($KTaO_3$)) for microwave and radio frequency (rf) devices due to their chemical stability, lattice constant, and dielectric characteristics. At cryogenic temperatures, these transition metal oxides exhibit interesting dielectric properties which could potentially be used to improve rf and microwave measurement techniques. However, before integrating these materials into the cryogenic measurement setup, they require electrostatic characterisations to understand the basics of quantum paraelectricity. In this chapter, I focus mainly on two questions concerning this material – (1) How does temperature affect dielectric constant? (2) How can an external electric field influence the permittivity at low temperature (at 10 mK)?

Description of voltage (V in volts) sweeps used in this chapter

For a span of ± V_{max} ($-V_{max} \leq 0 \leq +V_{max}$), forward sweep: 0 to $+V_{max}$; reverse sweep: $+V_{max}$ to $-V_{max}$; return sweep: $-V_{max}$ to 0. For different span, V_{max} is different. Each cycle starts with a forward sweep and ends with a return sweep with an intermediate reverse sweep.

3.1 Variable capacitor

In literature review 2.2, we learnt that these materials can be used at low temperatures. Since I want to investigate the dielectric properties, making a capacitor out of this material and characterising the capacitor at low temperatures can provide insight into the material. Hence, I design and fabricate a planar capacitor on top of this material. Since the geometrical capacitance depends on the dielectric constant, any change in that should result in a change of the capacitance.

3.1.1 Device

I design concentric planar capacitors with three different separation gaps between the electrodes to investigate how the tunability of the dielectric constant depends on the separation. There are four capacitors of each kind, as shown in figure 3.1. The capacitors are placed at different places to examine the homogeneity of the substrate. Different values of the same geometrical capacitors at different places will indicate that the substrate is not homogeneous. The device used in the experiment, shown in figure 3.1, is manufactured on a single crystal $SrTiO_3$ substrate from SurfaceNet. The metal layer (dark in figure 3.1) is made from titanium (Ti) / gold (Au) (10/100 nm) using laser lithography followed by evaporation and lift-off (see appendix C.2).

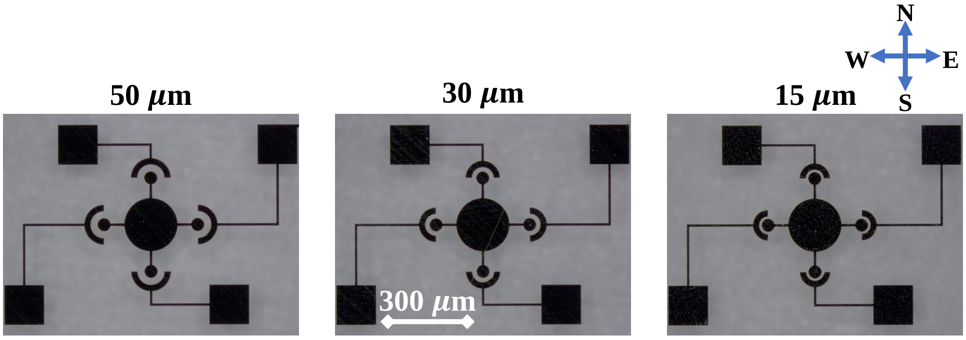

Figure 3.1: Dark field microscopic images of 50 µm, 30 µm, and 15 µm gap capacitors. E, W, N, and S refers to east, west, north, and south direction to indicate the capacitors of different gap sizes in different directions.

3.1.2 Measurement and analysis

Following wire bonding, the measurement is performed at 10 mK in a dry dilution refrigerator (Triton model, Oxford Instruments). The capacitances of five different capacitors are measured simultaneously during cool-down using lock-in amplifiers. At the base temperature (10 mK) of the refrigerator, each capacitor is individually characterised.

3.1.2.1 Temperature dependence of the capacitors

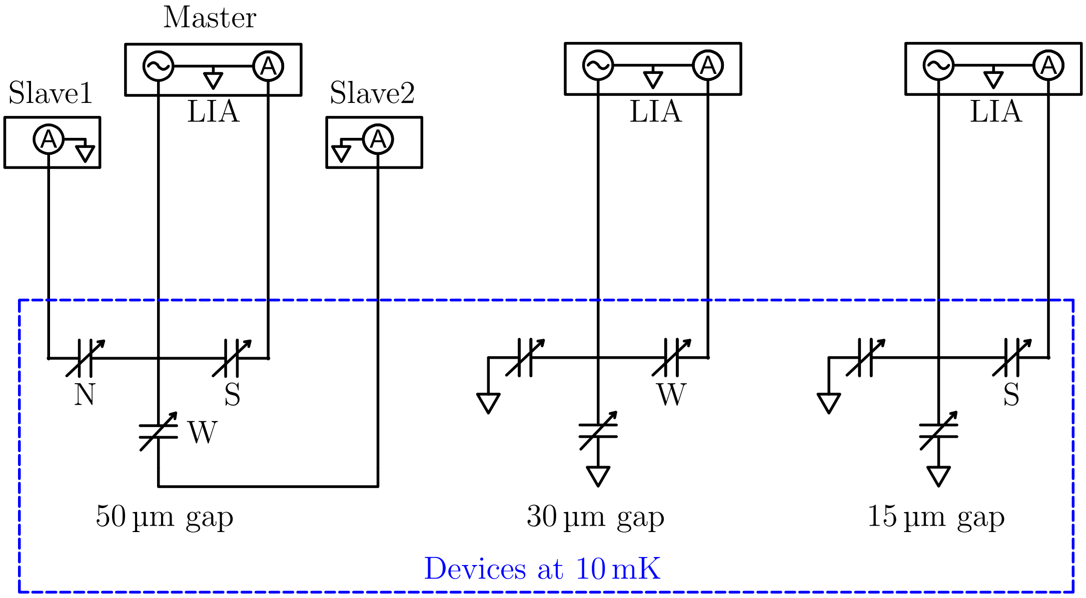

Figure 3.2: Experimental setup for measuring multiple capacitors simultaneously using lock-in amplifiers (LIAs).

The quasi-dc (direct current) measurement setup for measuring different capacitors during cool-down is shown in figure 3.2. Three 50 µm gap capacitors are measured simultaneously using three lock-in amplifiers along with a 30 µm and a 15 µm gap capacitors using two other lock-in amplifiers. Each individual capacitor is biased with an oscillating voltage signal (V_{ac}) of amplitude of 100 mV and the current is measured using a lock-in amplifier. For 50 µm, 30 µm, and 15 µm gap capacitors, the frequencies of the oscillating fields are 91.742 Hz, 74.447 Hz, and

113.089 Hz, respectively. The frequencies are chosen in such a way that they are well below the cut-off frequency of the low-pass filter installed on the dc lines inside the fridge. The frequencies are well separated to avoid cross-talk between the dc lines. The unused electrodes are kept grounded during measurement.

In this chapter, I am going to use a notation, C<x><D> to indicate different capacitors at different positions. C<x><D> refers to a capacitor (C) with a separation gap of x µm between the electrodes in the D direction, where 'x': 50 or 30 or 15 and 'D': E (east) or W (west) or N (north) or S (south). The direction in the nomenclature is indicated in figure 3.1

As shown in figure 3.2, C15S, C30W, C50W, C50N, and C50S are measured during cool-down. The lock-in amplifiers used to measure C50W, C50N, and C50S are clock synced and are set up in a master-slave configuration. To measure the capacitance, I measure the impedance (Z_{cap}) by sending an ac voltage signal of a fixed frequency and then measuring the current passing through each capacitor. As we know,

$$\begin{aligned} |Z_{\text{cap}}| &= \frac{|V_{\text{ac}}|}{|I_{\text{ac}}|}, \\ \implies \frac{1}{2\pi f C} &= \frac{|V_{\text{ac}}|}{|I_{\text{ac}}|}, \\ \implies C &= \frac{|I_{\text{ac}}|}{2\pi f\,|V_{\text{ac}}|} \qquad (3.1) \end{aligned}$$

where, C is the capacitance, f is the signal frequency, V_{ac} is the amplitude of the ac signal and I_{ac} is the measured current at the signal frequency. Using equation 3.1, I calculate the capacitance of all capacitors.

The capacitance value for individual capacitors in figure 3.3 is obtained by subtracting the parasitic capacitance of the wiring from the measured value. Figure 3.3 shows that as the temperature decreases, the capacitance increases for each capacitor. This indicates that the dielectric constant of the substrate has a higher value at low temperatures than at room temperature. Below 4 K, the dielectric constant remains the same, resulting in no further change in capacitance. These

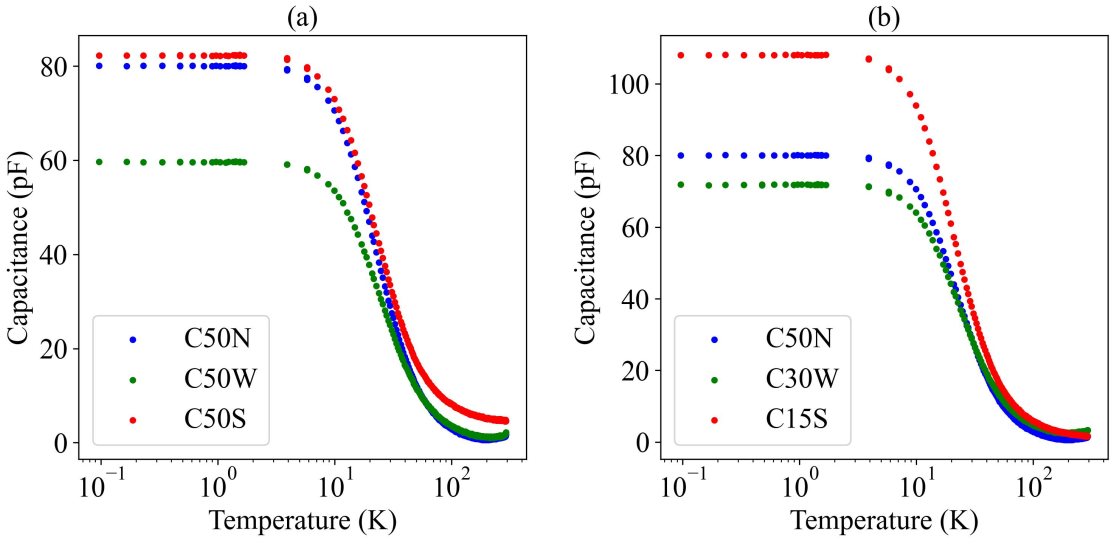

Figure 3.3: Temperature dependence of different capacitors (a) similar structure at different places, (b) different capacitors with different separation gaps between the electrodes. The data are taken during cool-down.

results agree with the results of previous experiments [27, 43, 44]. Figure 3.3a also dictates that the substrate is not uniform as the capacitors of the same gap at different locations have different values. The measured capacitance values are listed in table 3.1 which tells us that the capacitance at 10 mK is much higher than at room temperature, as is the dielectric constant.

	50 µm	30 µm	15 µm
East	-	77	102
West	59 (2)	71 (3)	35
North	80 (1)	-	-
South	82 (4)	74	108 (1)

Table 3.1: Initial capacitance values in pF for all capacitors measured at 10 mK (the capacitance values at room temperature are written in blue).

3.1.2.2 Electric field tunability of the capacitors

At the base temperature (10 mK) of the fridge, the capacitors are individually characterised. At first, I measure C50N with the application of different dc voltages on the electrodes as shown in figure 3.4, while monitoring the dc current flowing

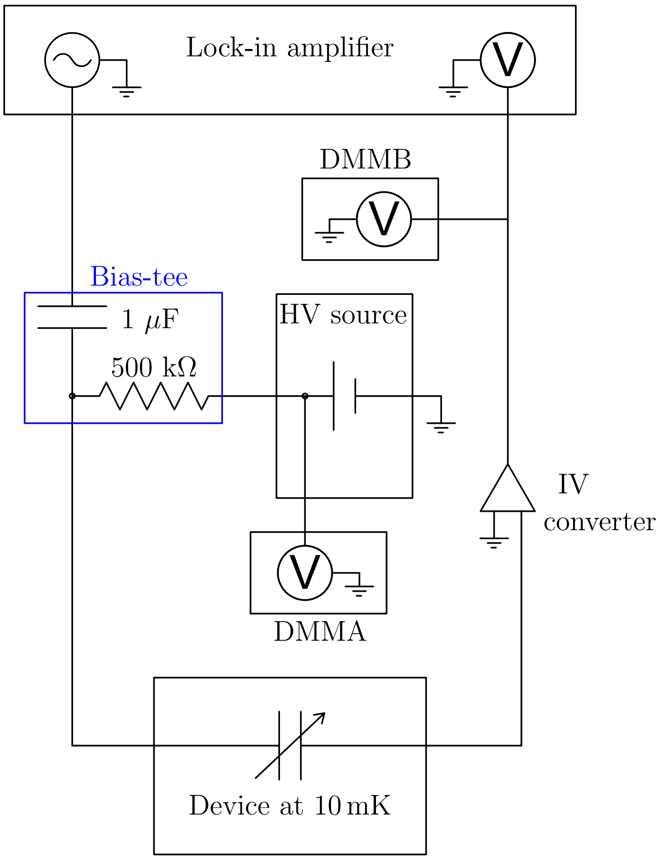

Figure 3.4: Measurement configuration for electric field dependent dielectric constant (HV: high voltage; DMM: digital multi-meter).

through the circuit using two digital multi-meters (DMMs). DMMA provides the current value drawn from the high voltage source while DMMB detects if any dc current is passing through the device capacitor. I use equation 3.1 to measure the capacitance using a lock-in amplifier.

Initially, I sweep the voltage from 0 to 5 V (forward sweep) with a step size of 0.25 V while measuring the capacitance at each set voltage. Then the voltage is swept to −5 V (reverse sweep) and finally returns to 0 V (return sweep) with the same voltage step size. This produces the plot shown in figure 3.5a. Since, on the removal of the voltage, the capacitance value does not return to its initial value, I keep sweeping the voltage of the same span as described above to see when the value at 0 V stops changing. Figure 3.5b shows that after the first cycle (which includes the

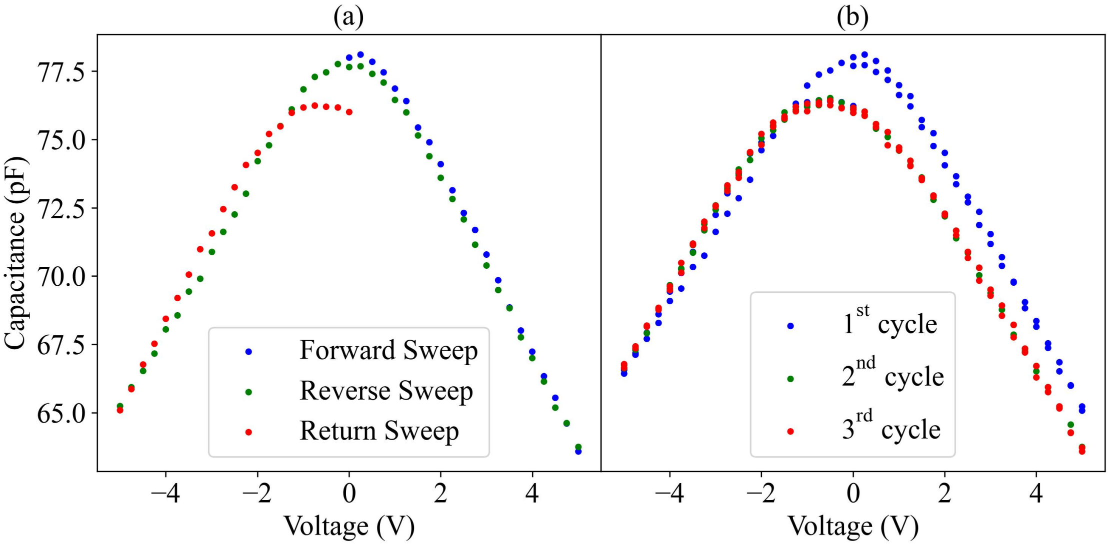

Figure 3.5: C-V characteristic of C50N (a) for different voltage sweeps in first cycle, (b) for different cycles of the same voltage span.

forward sweep, reverse sweep, and return sweep), the pattern of the capacitance vs. voltage curve does not change any more. It is a well-known fact that the substrate does not restore its initial state after the application of an external electric field, which causes a change in the capacitance value at 0 V [28, 30, 45].

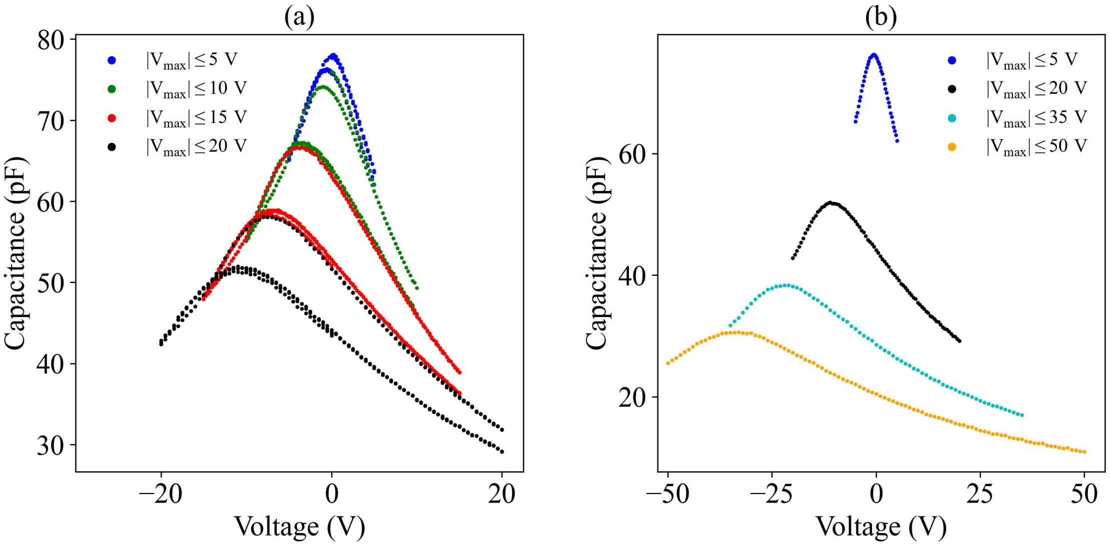

Figure 3.6: C-V characteristic of C50N for different voltage spans from ±5 V to ±50 V.

To further investigate, I continue to increase the voltage span from ±5 V to ±50 V. For each voltage span, I continue to sweep the voltage in the above-mentioned trend until the C-V curves stop changing their pattern for a specific span of voltage. From figure 3.6, we can see that the initial capacitance value cannot be recovered after applying ±50 V across the electrodes on the same cool-down.

C15S is then characterised. The capacitance value (105 pF) is slightly different from its initial value, mentioned in table 3.1. A similar measurement sequence is followed to examine how different voltages affect this capacitor. In figure 3.7a it is shown that this also follows the same pattern as C50N. However, beyond a certain voltage, the capacitor starts leaking dc current, which means that a conductive path is created through the substrate between the electrodes.

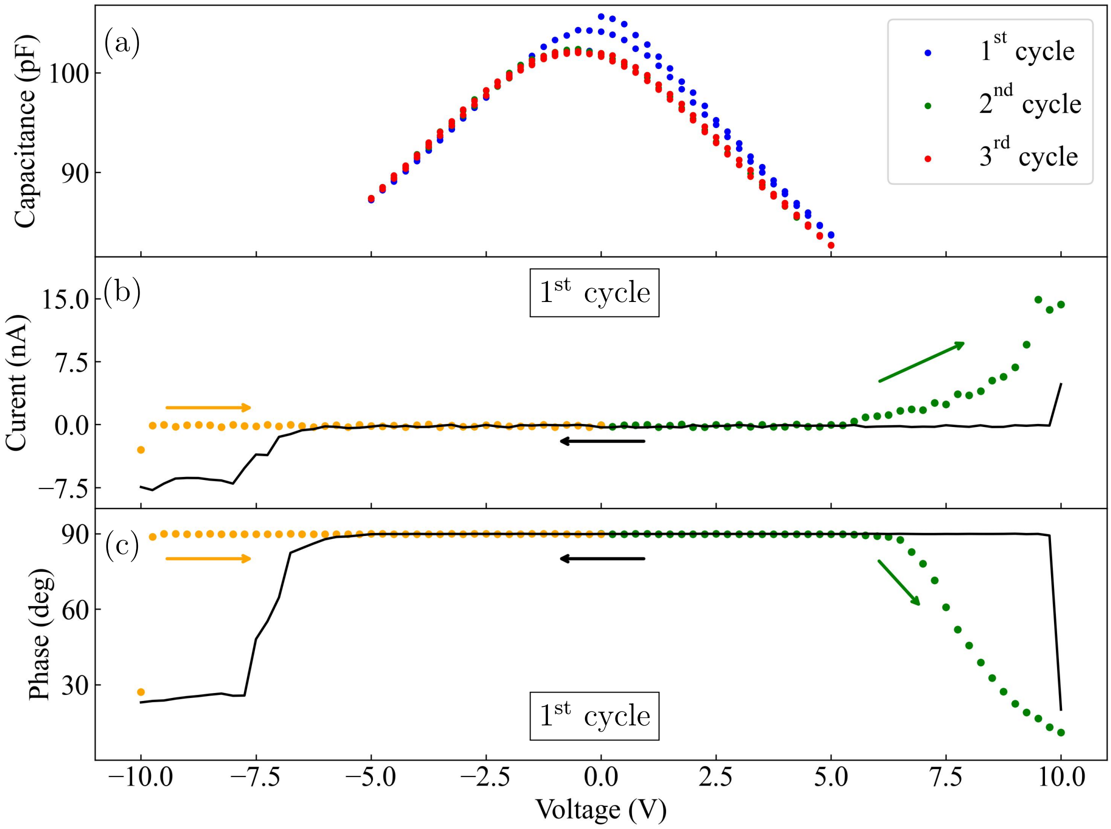

Figure 3.7: C-V characteristic of C15S. (a) for different voltage cycles. (b) and (c) present leakage current and phase respectively, for forward (green), reverse (black), and return (orange) voltage sweeps in the first cycle with a span of ±10 V.

With an increase in the voltage span from ±5 V to ±10 V, for the forward sweep the capacitor starts to leak (figure 3.7b) and the phase of the ac signal also changes (figure 3.7c). When the device is totally capacitive, the phase of the signal is 90°. The phase starts to decrease beyond +6 V, supporting the notion that a conductive path has opened up in parallel with the capacitor. Surprisingly, in the reverse sweep (figure 3.7b) current almost stops leaking above +6 V (except at +10 V). Instead, it starts to leak below −6 V, which is again supported by the phase change. During the return sweep in figure 3.7b, there is no leakage current except at −10 V (although the amount of leakage current is reduced). The leakage current vanishes for the next cycle of the same voltage span. However, it appears again when the maximum voltage is set to a higher value and vanishes again in the next few cycles. This behaviour is shown in figure 3.8.

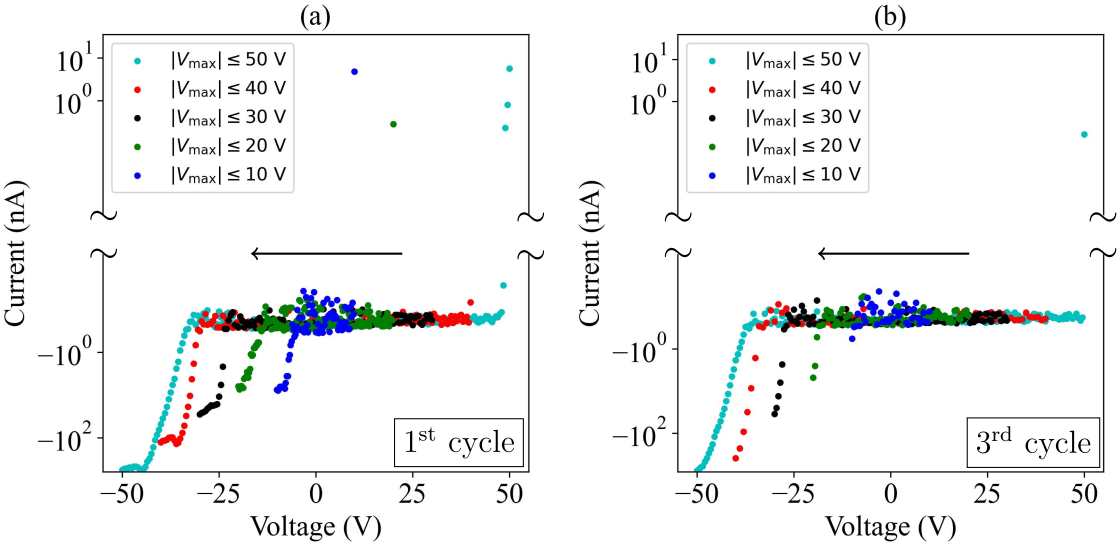

Figure 3.8: Leakage current through C15S for reverse sweep of different voltage spans for (a) 1st cycle and (b) 3rd cycle. The arrow indicates the direction of scanning.

When comparing figure 3.8a and figure 3.8b, it can be said that with increasing number of voltage sweep cycles, the cutoff voltage increases. In other words, the dc current starts to leak near the upper end of a voltage sweep. For the positive voltage in a higher cycle, the leakage current almost vanishes. However, for a negative voltage, even at a higher cycle, the leakage current exists, although the threshold voltage is higher for a higher cycle.

Evaluating the tunability of devices: The tunability of the capacitance values for different gaps is demonstrated in figure 3.9. The plot is based on the data acquired during the reverse voltage sweep of the second cycle. In figure 3.9, C_0 denotes the capacitance value in the absence of an external electric field.

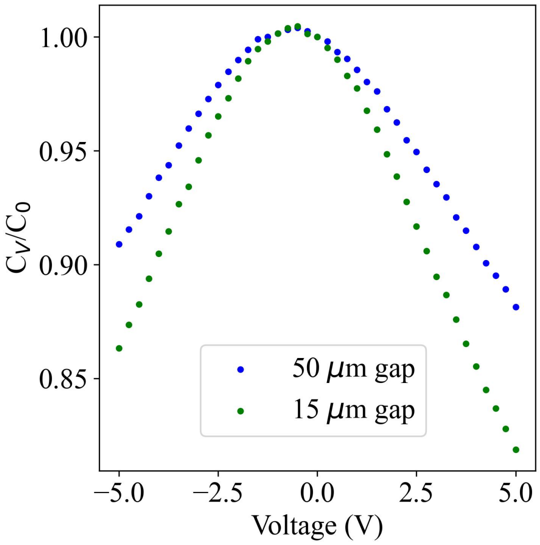

Figure 3.9: Tunability comparison between a 50 µm and a 15 µm gap capacitor. The tunability is measured by the ratio between capacitance at different voltages (C_V) and capacitance at $V = 0$ (C_0).

As expected, it is very evident from figure 3.9 that 15 µm gap devices are more tunable than 50 µm gap devices. Tunability is measured by the change in capacitance with the dc voltage. The more tunable the device, the larger the change in capacitance with the same amount of voltage.

After characterising C50N and C15S, when I measure the capacitance of C30W, the value (60 pF) has changed significantly (compared to table 3.1) due to the effect of the stray electric field from other capacitors. Although C30W is separated by ~ 2 mm from the other measured capacitors, the stray electric field is strong enough to leave an impression. As discussed earlier in this section, if a capacitor experiences any external electric field, it becomes unable to restore its initial dielectric constant.

Hence, I have characterised C30W in the same pattern as before with its new value [figure 3.10].

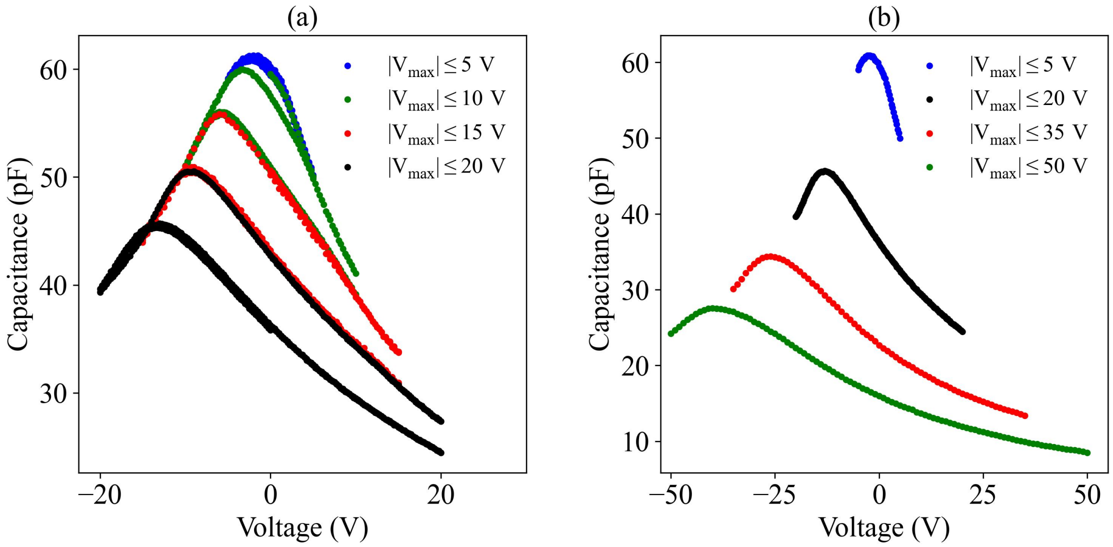

Figure 3.10: C-V characteristic of C30W for different voltage spans from ±5 V to ±50 V.

Figure 3.10 shows that C30W also follows the same trend of C-V characteristics as C50N and C15S. Hence, it can be concluded that, for all kinds of gap capacitors, the dielectric constant is more affected by the negative voltages. This is true even when all sweep directions are reversed.

1. The initial polarisation state is more affected by the negative voltages than by the positive voltages [45].
2. The maximum capacitance (and therefore dielectric constant) shifts toward the negative voltage after a full cycle (comprising forward, reverse, and return sweeps) of the voltage sweep [28].

Following the same fashion of applying voltage up to ±50 V to the capacitors, the new capacitance values become very different from their initial values due to the inability to restore their initial phase. The new values are listed in table 3.2.

To further investigate the tunability of the devices and the mechanism of restoring the initial state of the material, I continue to sweep voltage (with a

	50 µm	30 µm	15 µm
East	-	32	46
West	19	15	35
North	19	-	-
South	22	3	32

Table 3.2: Capacitance value in pF for all capacitors after experiencing maximum voltage of ±50 V.

span of ±50 V) while warming the fridge in a controlled way (using PID controller (proportional-integral-derivative) up to 90 K) to room temperature (280 K).

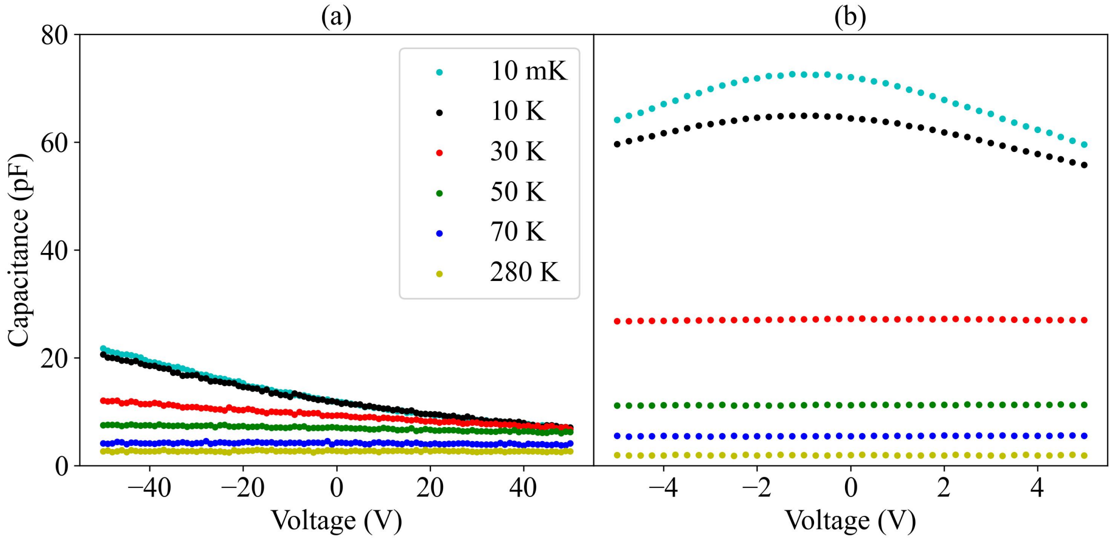

Figure 3.11: C-V characteristic of C50N for different temperatures during warming up the fridge (a) when the device experienced very high voltage of ±50 V during 1st cool-down, (b) when the device experienced a maximum of ±5 V during 2nd cool-down.

The device used for this experiment is C50N. Figure 3.11a presents the data acquired after the device (let us call it the 'Cooldown-I device') has experienced a maximum of ±50 V along with the stray fields from adjacent devices. As shown in figure 3.11a, at 10 mK the maximum capacitance cannot be achieved within the range of ±50 V. However, the change in capacitance with voltage is visible up to 50 K, indicating that beyond 50 K, the capacitance (or the dielectric constant) of a 50 µm gap capacitor is no longer electric field dependent. Moreover, the dielectric constant decreases as the temperature increases.

Figure 3.11b represents the same device (C50N) without experiencing a large electric field (let us call it the 'Cooldown-II device'). Hence, maximum capacitance can be achieved within the range of ±5 V. Similar to the Cooldown-I device, for the Cooldown-II device also, the dielectric constant decreases with the increase in temperature, resulting in lower capacitance. However, unlike the Cooldown-I device, beyond 30 K, the electric field tunability of the dielectric constant for a 50 µm gap capacitor vanishes for the application of a maximum of ±5 V. Thus, figure 3.11 provides insight into how the tunability of the dielectric constant of a quantum paraelectric material depends on the temperature.

Restoring the initial phase with a thermal cycle: Once the polarisation state of the material is distorted by a very high electric field at low temperatures, the conventional way to restore the initial condition is to thermally cycle up to room temperature [45]. For three different capacitors (as shown in figure 3.12), the capacitance values at low temperatures (below 10 K) for the 1st cool-down are more than those for the 2nd cool-down. Hence, the highest capacitance (and also dielectric constant) is not achieved in the 2nd cool-down. This indicates that a thermal cycle up to room temperature does not completely restore the initial polarisation state for these devices. This contradicts the conventional approach, necessitating further research to identify any additional contributing factors.

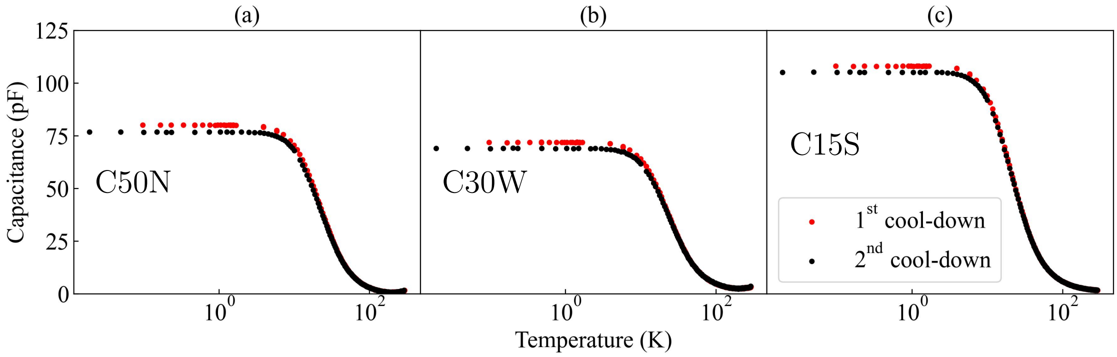

Figure 3.12: Capacitance vs. temperature for three different capacitors (a) C50N, (b) C30W, and (c) C15S.

3.2 Outlook

This chapter is a detailed investigation of the dielectric response of a quantum paraelectric material at 10 mK in the presence of an external electric field. The conclusions of this chapter can be drawn as follows.

- The experimental results of the temperature dependence of the capacitance (and therefore the dielectric constant) agree with the theoretical model (discussed in chapter 2) which tells us that the dielectric constant increases drastically at low temperatures.
- The capacitance vs. voltage curves show that the dielectric constant is a function of an external electric field which can be explained by the LDG theory [45].
- Using these characteristics, an on-chip cryogenic variable capacitor is constructed on a quantum paraelectric material ($SrTiO_3$).
- It is observed that the negative voltages have more impact on the dielectric constant of the material than the positive voltages. This means that the initial polarisation state is more affected by the voltages of negative polarity.
- The C-V characteristics for different gap capacitors have been analysed in this chapter. This reveals that when the gap is 15 µm or below, the capacitors leak current through beyond certain voltages.
- The tunability of the capacitors with respect to the applied voltages is studied, which tells us that the less the gap between electrodes, the more tunable the capacitor.

However, the chapter ends with an open question about the mechanism of restoring the initial polarisation state of these materials which is discussed in detail in chapter 6.

Chapter 4

Impedance matching device

After a thorough study of the dielectric nature of the quantum paraelectric materials through electrostatic characterisation, it is time to explore the response of these materials to high-frequency electromagnetic fields and this is carried out in this chapter by demonstrating a lumped element impedance matching network. A detailed discussion of this type of matching circuit has been described in section 2.1. From section 2.2, we know that quantum paraelectric materials show a high and tunable dielectric response at low temperatures. Chapter 3 demonstrates that an on-chip variable cryocapacitor can be made of this material. Taking advantage of these characteristics, I make an impedance matching device where the lumped elements (capacitors) are made of strontium titanate ($SrTiO_3$).

4.1 Significance of impedance matching

For measuring any quantum device (such as quantum dots [29], spin qubits [76]), we use a transmission line (either a coaxial cable or a coplanar wave guide structure) and there is generally an impedance mismatch between the device and the readout line [29, 77]. The typical impedance of a quantum system such as a single electron transistor is $\sim h/e^2 \approx 25.8\,\mathrm{k\Omega}$, while the typical impedance of a transmission line is similar to the impedance of the free space $\sim \sqrt{\frac{\mu_0}{\epsilon_0}} \simeq 377\,\Omega$. Most commercially available coaxial cables have a standard impedance of $50\,\Omega$. Therefore, to ensure an optimum power transfer, the impedance of the quantum device must match the impedance of the feedline. In this way, the best charge and capacitance sensitivities are also achievable [28]. However, unpredictable variations between device impedances often require in situ tunability in the matching circuit, which is possible by implementing a variable capacitor. Moreover, the tunability of the resonance frequency is also needed for optimal performance within certain bandwidths allowed by other high-frequency components. Therefore, coupling the quantum devices to an impedance matching circuit with an in situ tunable resonator could potentially improve the readout scheme.

4.2 Simulation using Microwave Office software

Prior to building an on-chip impedance matching network using a quantum paraelectric material, I simulate the design (as shown in figure 4.1) in AWR Microwave Office software [78] to choose the correct electrical configuration and to optimise the circuit parameters for a perfect match.

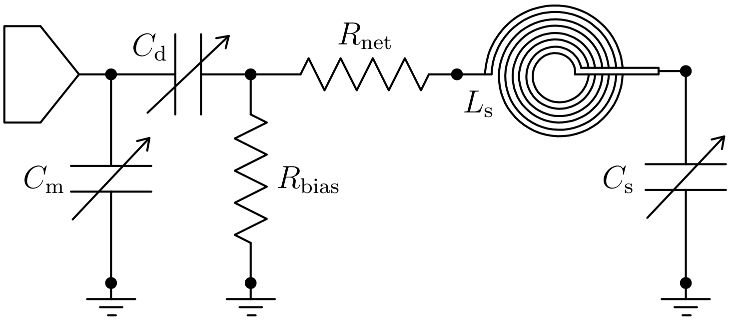

Figure 4.1: Schematic diagram of a lumped element-based impedance matching network with an in situ tunable electrical resonator. The resonator is formed from an inductor L_s and a variable capacitor C_s. The variable capacitors C_m and C_d controls the impedance of the circuit and decouples the circuit from the fridge's electrical controls respectively. Parasitic losses in the circuit are parametrized by an effective resistance R_{net}.

The matching device consisting of an in situ tunable LC resonator [29] is configured in a reflectometry setup. This matching network can be used to match a quantum device with high impedance to a 50 Ω transmission line. Now, to construct an electrical LC resonator, an inductor (L_s) is added in series with a capacitor (C_s). Therefore, the resonance frequency (f_s) is given by $1/(2\pi\sqrt{L_\mathrm{s}C_\mathrm{s}})$. To make the resonator tunable C_s is considered as a variable capacitor. In order to improve the impedance matching between the sample and the 50 Ω transmission line, a matching capacitor (C_m) and a decoupling capacitor (C_d) are introduced in the circuit in parallel and in series with the sample, respectively. The reactance of (C_m) adjusts the net impedance of the entire circuit to be closer to the perfect matching point. A parasitic resistor (R_net) has also been included. For biasing the sample with voltage, a resistive path (R_bias) has also been introduced to the circuit. However, for the sake of simplicity, R_bias is grounded in the simulation.

In the simulation, L_s is chosen to be a spiral inductor with: 5 turns; inner radius = 300 µm; turn width = 10 µm; spacing between turns = 20 µm. The value of L_s is 31.679 nH (calculated using an online tool [79]). For L_s = 31.679 nH, the value of C_s determines the resonance frequency, as shown in figure 4.2

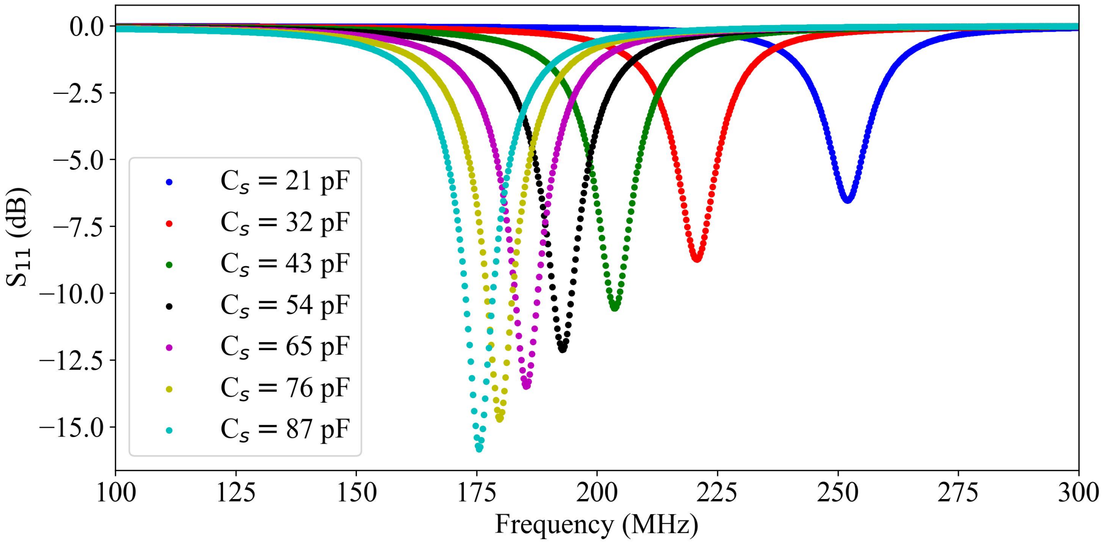

Figure 4.2: Reflection coefficient S_{11} plotted as a function of frequency for different values of C_s. In this plot I have chosen C_m = 104 pF and C_d = 75 pF.

I choose to operate the device at C_s = 54 pF. Now, keeping C_d the same as before, the value of C_m is swept from 50 pF to 104 pF. As shown in figure 4.3, the signal is the strongest for $C_\mathrm{m} = 77\,\mathrm{pF}$. Hence, the match is optimal at this point. As mentioned above, although the resonance frequency shifts slightly higher with decreasing C_m, the impact is negligible.

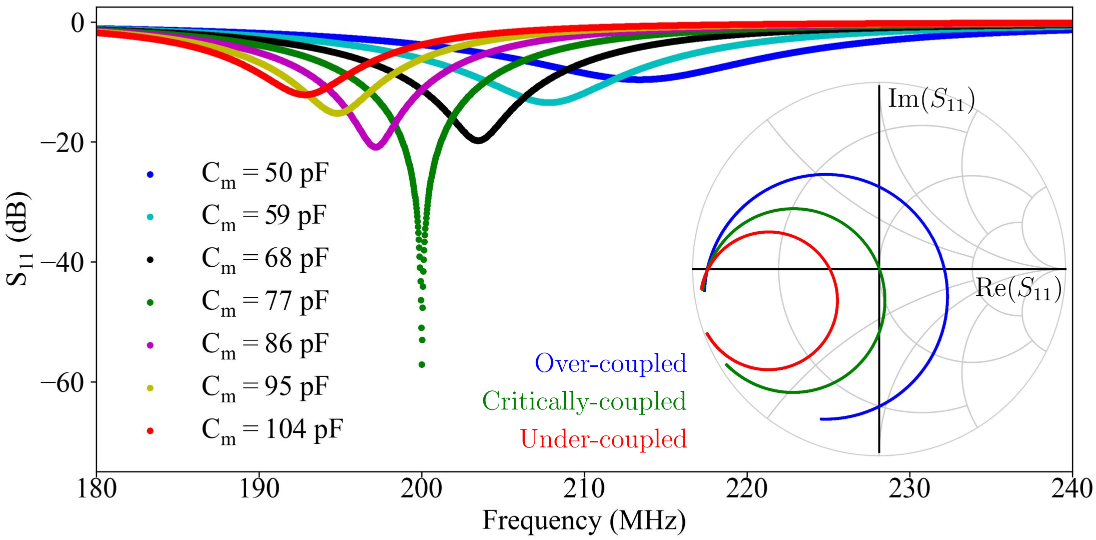

Figure 4.3: The effect of C_m on S_{11} for fixed $C_\mathrm{s} = 54\,\mathrm{pF}$. In the inset, the Smith chart shows different coupling conditions.

As shown in figure 4.2, for $L_\mathrm{s} = 31.679\,\mathrm{nH}$ and $C_\mathrm{s} = 54\,\mathrm{pF}$, f_s is 193 MHz. For this particular frequency, when the value of C_m is 77 pF (given $C_\mathrm{d} = 75\,\mathrm{pF}$), there is the best match between the 50 Ω transmission line and the tunable resonant circuit. This is directly associated with the critical coupling condition as shown in figure 4.3. Therefore, we can see that C_m controls the coupling conditions and also results in a slight change in f_s. Thus, the critical coupling as well as the best matching condition can be obtained by modifying C_m. The optimised parameters derived from the simulation for the best impedance match are listed in table 4.1.

L_s	31.679 nH
C_s	54 pF
C_m	77 pF
C_d	75 pF
R_net	2 Ω
R_bias	10 kΩ

Table 4.1: Optimised values of all circuit parameters.

Go to Contents↑

4.3 Measurement configuration and device characterisation

This section contains a detailed description of the reflectometry measurement scheme for impedance matching devices and device characterisations in the sub-GHz range at 10 mK. An overview of the device design is also provided for three different generations of the same type of devices with minor modifications. The details of the fridge wiring for reflectometry measurements of these specific devices can be found in appendix A. In the following subsections, I am not impedance matching a real sensor but testing the efficiency of the matching circuit, which could potentially be integrated with a high impedance device.

4.3.1 First generation device characterisation

The spiral inductor (L_s) as shown in figure 4.4, is made of a 165 nm thick niobium (Nb) film sputtered on a 1 µm thick silicon dioxide (SiO_2) terminated highly resistive 5 mm×5 mm silicon (Si) chip from inseto. The superconducting film is used for the propagation of the lossless signal. The rest of the device (including C_m, C_d, R_bias) is also made of 165 nm thick niobium but on a titanium dioxide (TiO_2) terminated 10 mm×10 mm $SrTiO_3$ chip. The details of the fabrication recipe can be found in appendix C.

Figure 4.4 shows how the device is electrically connected to the room temperature equipment. A vector network analyser (VNA) is used to monitor the reflected signal S_{11}, while high voltage sources are used to tune the variable capacitors C_s, C_m, and C_d. To avoid the escape of the radio frequency (rf) signal through dc ports, the variable capacitors (varactors) are biased via on-chip low pass filters (LPFs) (consisting of a spiral inductor and finger capacitors). A bias tee (on the PCB) is used to adjust C_d.

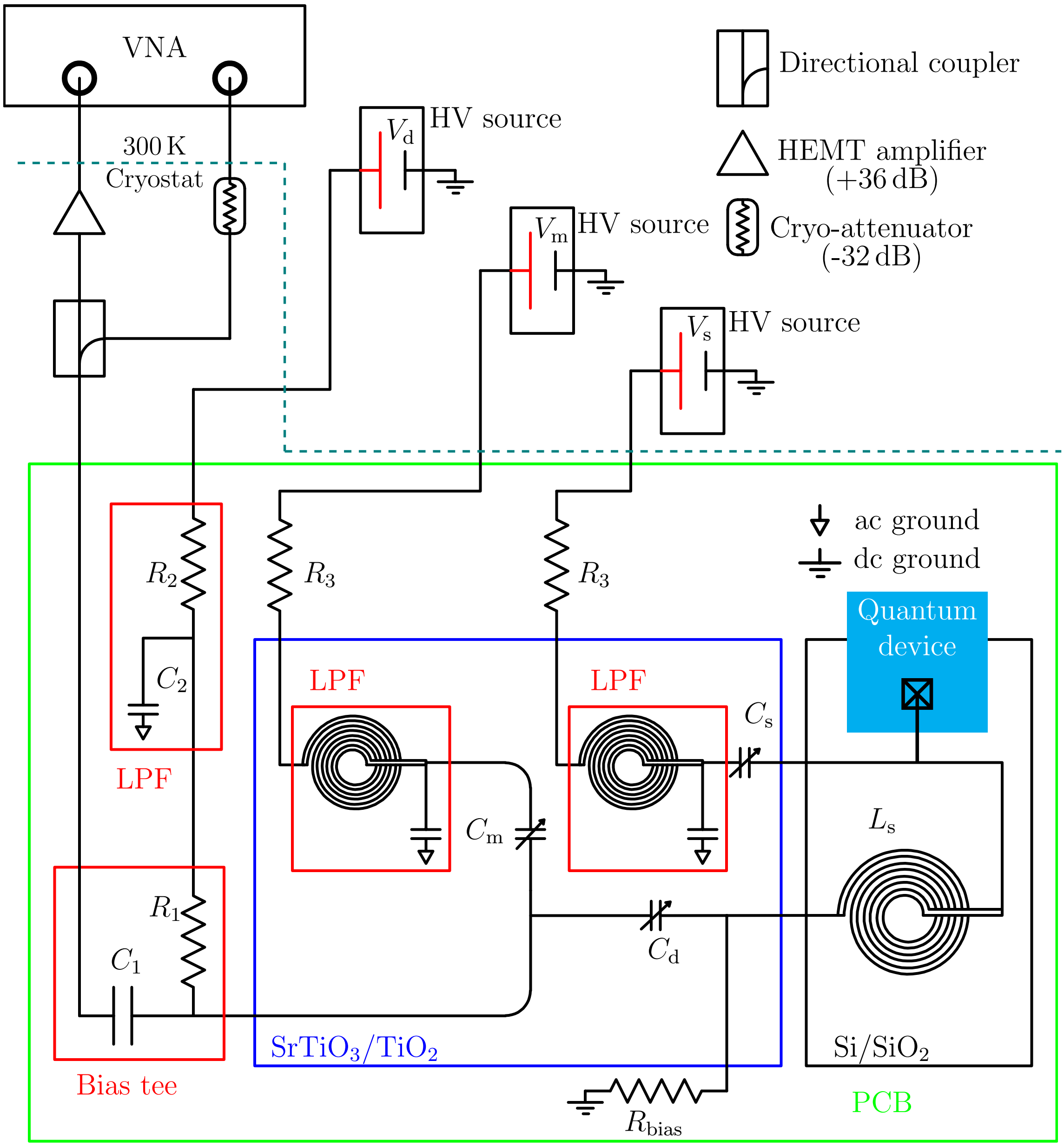

Figure 4.4: Experimental setup for impedance matching network. This is a direct implementation of the simulated design (figure 4.1). If there were a device to measure, it would be connected to L_s as shown in the figure. Every component inside the green box is at 10 mK. $R_1 = 50\,\mathrm{k\Omega}$; $C_1 = 10\,\mathrm{nF}$; $R_2 = 1\,\mathrm{k\Omega}$; $C_2 = 1\,\mathrm{nF}$; $R_3 = R_{\mathrm{bias}} = 5\,\mathrm{k\Omega}$; LPF: low pass filter; VNA: vector network analyser; PCB: printed circuit board; HV: high voltage; HEMT: high electron mobility transistor.

I have used a 14-turns spiral inductor with an inner radius of 300 µm and there is a circular pad of radius 250 µm in the center used for wire-bonding. The presence of a superconducting circular pad in the center of the inductor lowers the inductance.

Go to Contents↑

Hence, the inductance value calculated using an online tool [79] is no longer valid. I simulated the capacitance of different structures in ANSYS [80], but from chapter 3, we know that the same structures can have different values of capacitance. Hence, one way to find the resonance frequency, f_s (assuming that there appear many unwanted parasitic resonances) is by tuning C_s. Therefore, the plan of action is to find the resonance frequency (f_s) first by varying C_s by applying a dc voltage V_s across the capacitor. Once f_s is found, keeping C_s constant, C_m needs to be varied (by applying V_m) to find the perfect match point, where the reflected signal has the minimum amplitude. After finding the matching point, C_d can be tuned to search for critical coupling.

According to the plan, V_s is varied from 0 V to +60 V while monitoring the reflection coefficient (S_{11}) in VNA. A frequency sweep from 10 to 500 MHz (expected range of f_s) is performed in the VNA with a constant power of -80 dBm at the input of the device (including 33 dB attenuation along the refrigerator line and 12 dB attenuation by the directional coupler).

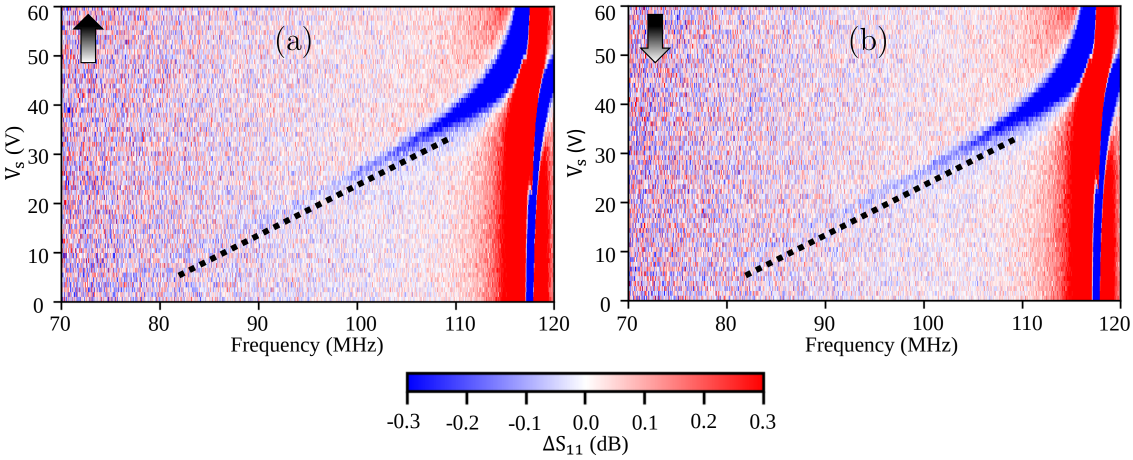

Figure 4.5: Finding f_s by tuning V_s. (a) forward sweep (from 0 V to +60 V) of V_s (b) reverse sweep (from +60 V to 0 V) of V_s. The dashed lines are to trace f_s. The arrows denote the voltage scan directions.

Figure 4.5a shows that there is a resonance that changes with V_s. However, the signal is so faint that it is barely visible in the spectrum. To detect the change, I plotted ΔS_{11} (= actual S_{11} - average S_{11} along the voltage axis) instead of actual

S_{11} on the colour axis. The frequency change is highlighted by the dotted line in figure 4.5a. Upon sweeping V_s from +60 V to 0 V, it produces a similar result as shown in figure 4.5b.

A similar pattern is found between 300 and 350 MHz as shown in figure 4.6 where the change is indicated by the dashed line. There are two parasitic resonances near 332 MHz and 340 MHz which are not affected by the change in C_s. The difference between the resonance near 70 MHz (figure 4.5) and the resonance near 320 MHz (figure 4.6) is that the former one does not show any signal at $V_\mathrm{s} = 0$, while the latter is visible.

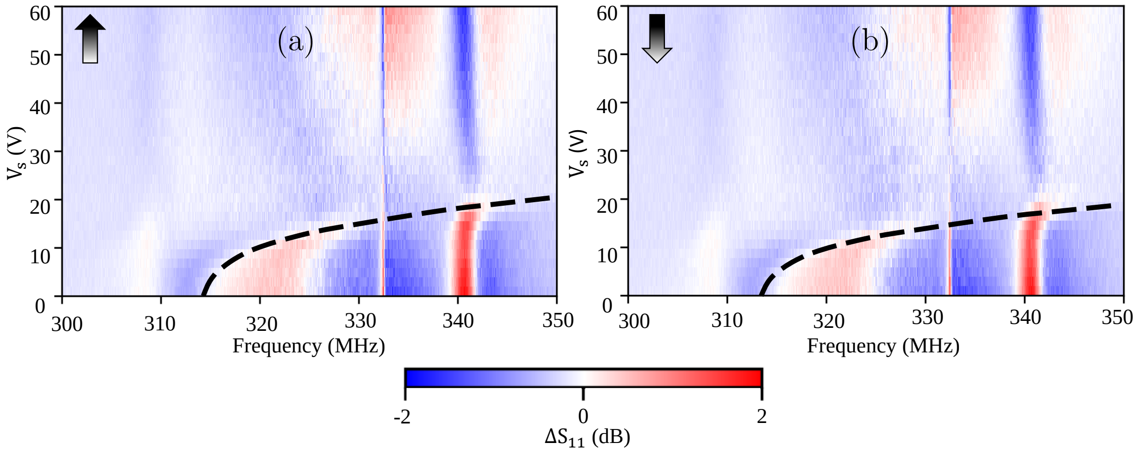

Figure 4.6: Finding f_s by tuning V_s. (a) forward sweep (from 0 V to +60 V) of V_s (b) reverse sweep (from +60 V to 0 V) of V_s. The dashed lines indicate the changes in f_s. The arrows dictate the scanning directions.

To confirm if any of these resonances is the resonance of the in situ LC resonator, I extend the voltage span from +60 V to −60 V. For the resonance near 70 MHz, it does not show any sign of resonance for $V_\mathrm{s} < 0$, while the other one produces an interesting plot shown in figure 4.7. This is quite promising, as the plot can be fitted with a model developed from the LGD theory [30, 45].

Repetition of the measurement as shown in figure 4.7 produces a different result. The reflected signal becomes very faint and shifts its position towards higher frequency. This is due to the application of negative voltages, as it permanently changes the capacitance. We learnt from chapter 3 that after applying a negative

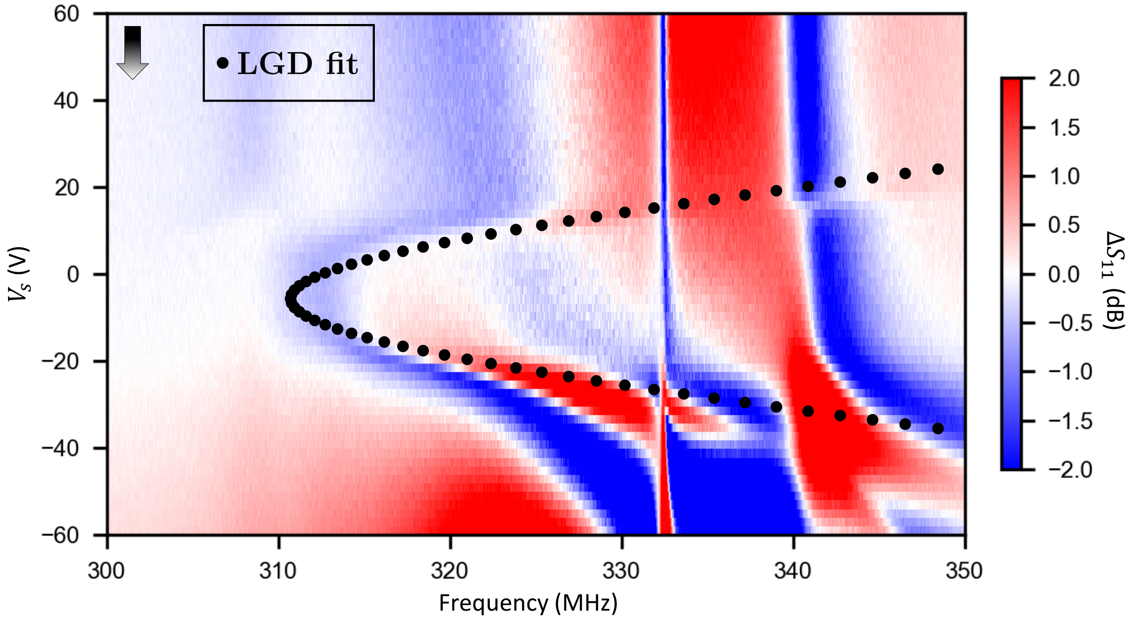

Figure 4.7: Measurement of reflected signal as a function of V_s in order to trace f_s. The change in f_s with respect to voltage is fitted using equation 2.5 from Landau-Ginzburg-Devonshire (LGD) model [81]. For the fit, the dielectric constant at zero electric field is chosen to be 27400 and the electric field tunability parameter is set as a free parameter. To take account of the hysteresis, an offset term is introduced to the model.

voltage the dielectric constant cannot be completely restored upon removal of the applied voltage. This is the reason why the resonance frequency shifts upwards at $V_\mathrm{s} = 0$. In other words, after applying the negative voltage, C_s decreases, resulting in a higher f_s. As the system remains partially polarised even when V_s is set to zero, the initial capacitance value cannot be retrieved and it causes a permanent change (until the device undergoes a thermal cycle up to room temperature which restores its initial state) in f_s.

Bear in mind that the device is not 50 Ω matched assuming that the geometrical capacitance of C_m is far from the value required for the perfect matching point. Hence, a weak signal is what we expect. As we now know the frequency range for f_s to appear, I next tune C_m to the correct value for which the signal has the minimum reflection. Another point to remember is that by applying voltage (of any polarity), we can only lower the capacitance value. Hence, the geometrical capacitance is the highest value, which could only be lowered by applying a voltage of any polarity.

Unfortunately, no significant change in reflected signal power in that frequency range is observed when adjusting C_m by voltage ranging between +60 V and -60 V. This indicates that the device cannot achieve the matching point. A probable reason could be that the matching capacitance required for impedance matching is beyond the geometrical capacitance of C_m. Therefore, by applying the voltage on C_m, the matching point can never be obtained. In addition, it is possible that part of the signal is lost through R_bias.

There are a few drawbacks of this device discussed here which I improved in the next generation of devices.

1. The sputtered niobium does not stick well with the TiO_2 terminated $SrTiO_3$ chip. This causes some lumps on the conducting line as shown in figure 4.8. This raises the requirement for an adhesive layer during fabrication.
2. R_bias used in this circuit is a thin film resistor mounted on the PCB. It can be improved by fabricating an on-chip resistor.
3. The spiral inductor can be surrounded by a ground plane to avoid floating charges.

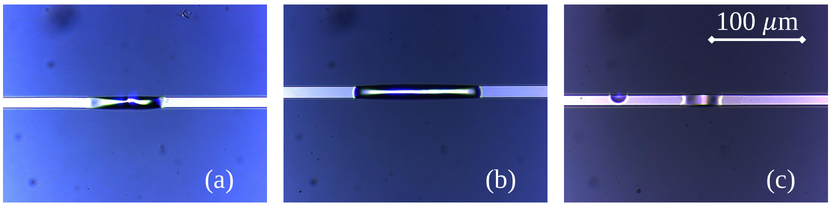

Figure 4.8: (a), (b), and (c) show different distorted parts of the conducting line.

4.3.2 Second generation device characterisation

The second-generation device is modified in such a way that the space on the $SrTiO_3$ chip is fully utilised by accommodating two devices. One chip contains two matching devices with different C_m values (indicated as C_{m1} and C_{m2} in figure 4.9). In case one matching device does not work, the other one could be tested without further fabrication delay. Another modification for second-generation devices is that R_{bias} is fabricated on the chip to reduce signal loss through that path.

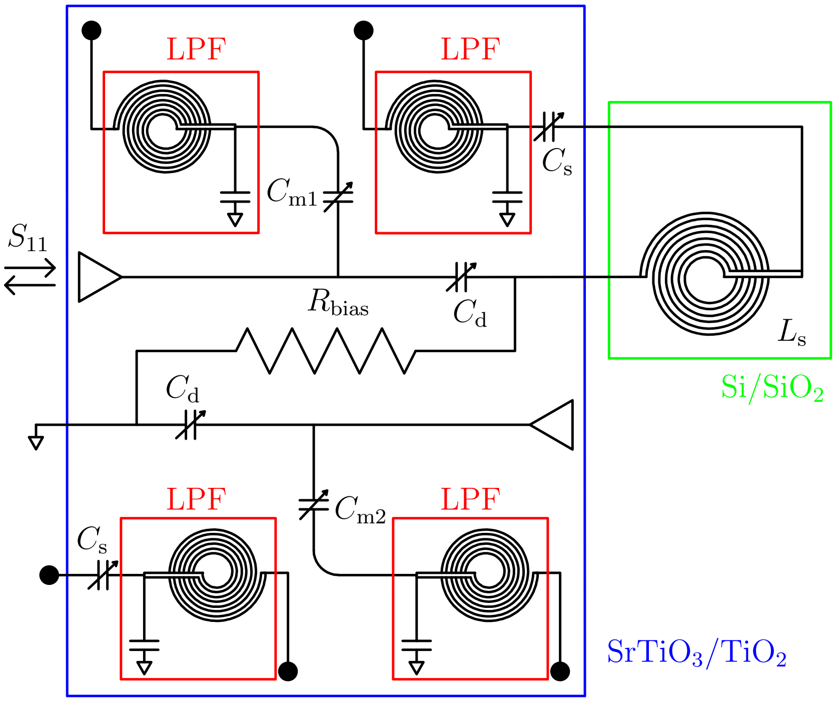

Figure 4.9: Schematic of two impedance matching devices on one $SrTiO_3$ chip. They share the same R_{bias} to save space. The top device is drawn in an operational mode when the bottom one is electrically disconnected.

A significant difference between first- and second-generation devices is that, except for the spiral inductor, the matching device is made of 200 nm thick Au on TiO_2 terminated $SrTiO_3$, where 10 nm thick titanium (Ti) is used as an adhesive layer. L_s is still made of 165 nm thick niobium on a SiO_2 terminated Si chip. However, L_s is surrounded by a ground plane to define a constant potential around the inductor. One limitation of this device is that both the networks cannot be used at the same time for impedance matching as they both share a common R_{bias} (10 kΩ, measured at room temperature).

Following the same measurement scheme mentioned in section 4.3.1, the devices are characterised one at a time. However, both devices do not show any sign of reflected signal. Even a faint signal, as in the case of a first-generation device, does not appear which could be traced by adjusting C_{s}. The change in C_{m} and C_{d} also did not make the suppressed signal appear. This means that not only does the matching network not function, but also the energy from the resonator is highly dissipated along the signal path.

One of the probable causes is the resistive conducting lines. Unlike a first-generation device, the signal in these devices suffers from two main loss mechanisms–the dielectric loss and the dissipation due to resistivity. Due to the high loss tangent of $SrTiO_3$, the signal weakens while propagating in both the first- and second-generation devices. In addition, the second-generation device uses a resistive conducting path, which dissipates the signal. Moreover, the way R_{bias} is placed next to the signal-carrying path [shown in figure 4.10] introduces a large parasitic capacitance parallel to C_{m}. These are likely to be the main reasons why the reflected signal does not appear in the reflection measurements.

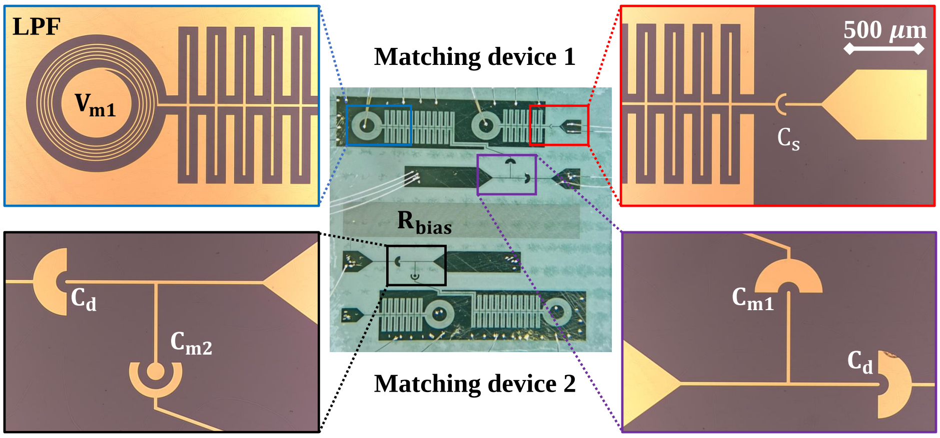

Figure 4.10: Image of 2^{nd} generation devices.

To improve the 3rd generation device, the following modifications are made:

1. Dedicate an entire $SrTiO_3$ chip to each impedance matching network to reduce parasitic components.
2. Maximise the tunability of C_m.
3. Reduce parasitic capacitance between the conducting line and on-chip R_bias by placing them as far away as possible from each other.
4. For both first- and second-generation devices, C_m, C_d, and C_s are electrically connected in such a way that when C_d is tuned by applying voltage through the bias tee (on PCB) or through R_bias, the electric field across C_m or C_s changes, respectively. To avoid this, in third-generation devices, I replace the variable C_s with a fixed C_s for voltage-independent f_s.
5. Reduce the resistive path length.

4.3.3 Third generation device characterisation

Implementing these modifications, the final version of the device is shown in figure 4.11. L_s and C_s are fixed, while C_m and C_d are tuned by voltages, V_m and V_d, respectively, as shown in figure 4.12.

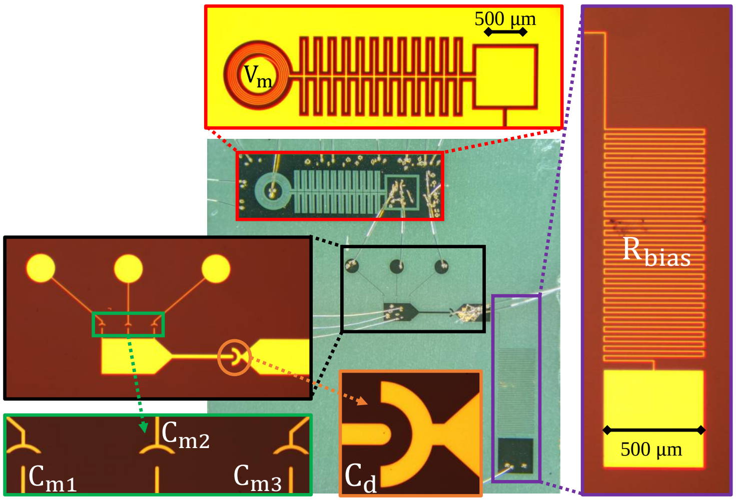

Figure 4.11: Optical image of 3rd generation fabricated device.

The measurement setup (figure 4.12) allows the reflected signal to be measured simultaneously with the values of C_m and C_d. The plan is to find the value of C_m for which the reflected signal is minimum. Then, to ensure that the critical coupling is achieved, C_d can be varied.

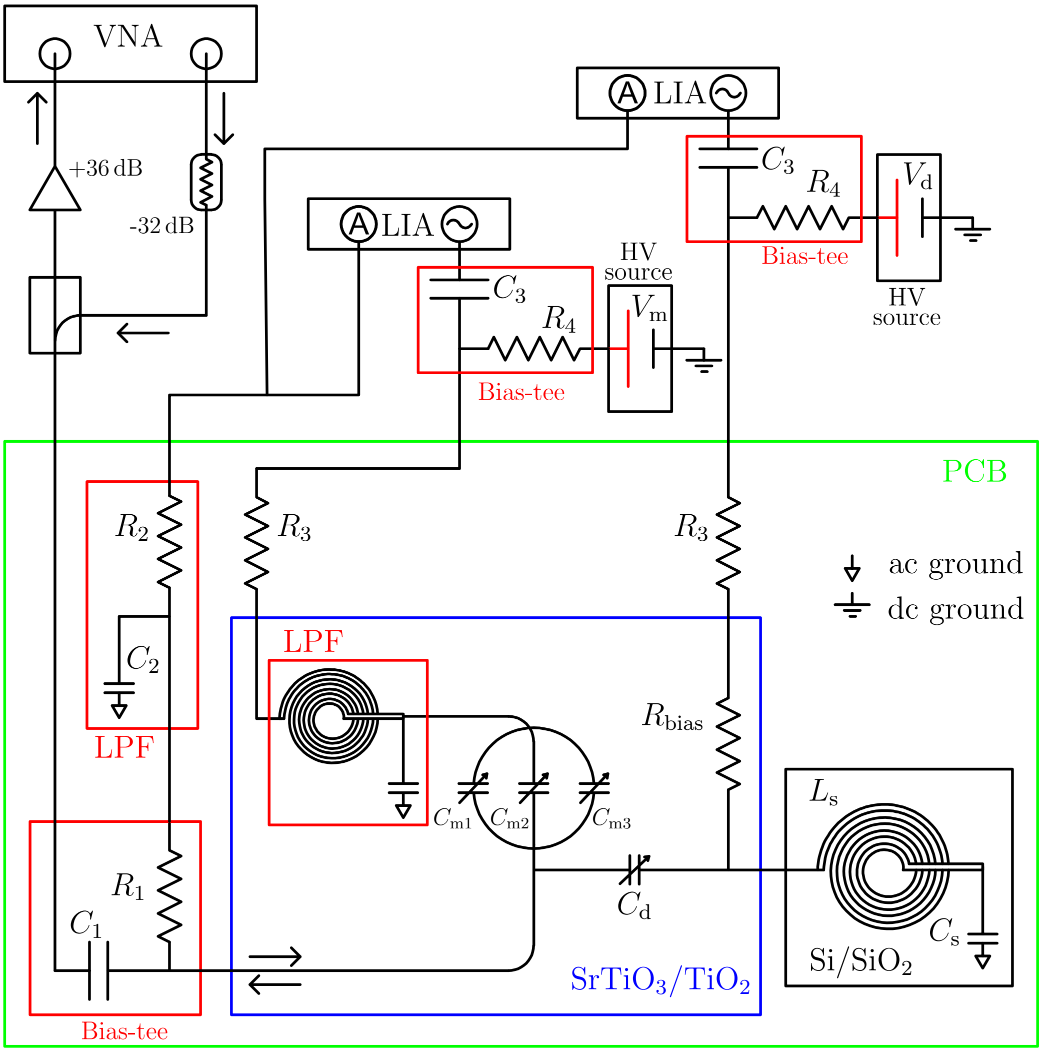

Figure 4.12: Experimental setup for reflectometry measurement. Every component inside the green box is at 10 mK. $R_1 = 50\,\mathrm{k\Omega}$; $C_1 = 10\,\mathrm{nF}$; $R_2 = 1\,\mathrm{k\Omega}$; $C_2 = 1\,\mathrm{nF}$; $R_3 = 5\,\mathrm{k\Omega}$; $R_4 = 500\,\mathrm{k\Omega}$; $C_3 = 1\,\mathrm{\mu F}$; LPF: low pass filter; VNA: vector network analyser; PCB: printed circuit board; HV: high voltage; LIA: lock-in amplifier.

Figure 4.13a shows that when $V_\mathrm{m} \sim 6.5\,\mathrm{V}$, the reactance of C_m ($C_\mathrm{m1} + C_\mathrm{m2} + C_\mathrm{m3}$) makes the impedance of the entire circuit close to $50\,\Omega$ resulting in a better impedance match and consequently the strongest signal, which is denoted by the blue region in figure 4.13a. To confirm that impedance matching is happening, I extend the voltage span to -15 V. As a result, we can see in figure 4.13b that for both polarities of V_{m}, the signal gets stronger. This could be illustrated in the following way: when $V_{\mathrm{m}} = 0\,\mathrm{V}$, the impedance of the circuit is far from the matching point; increase in $|V_{\mathrm{m}}|$ brings the impedance closer to the matching point, thus enhancing the signal; a further increase in $|V_{\mathrm{m}}|$ pushes the impedance away from the matching point, causing the signal to fade away. This is good evidence that the circuit is capable of adjusting the impedance and therefore will be useful for impedance matching when incorporated with a high-impedance device. Although in principle $|V_{\mathrm{m}}^{+}| = |V_{\mathrm{m}}^{-}|$ (where V_{m}^{+} and V_{m}^{-} are, respectively, the positive and negative voltages applied on C_{m} at the perfect matching points), due to the hysteric nature of the material (as discussed in chapter 3) $|V_{\mathrm{m}}^{-}| - |V_{\mathrm{m}}^{+}| \neq 0$.

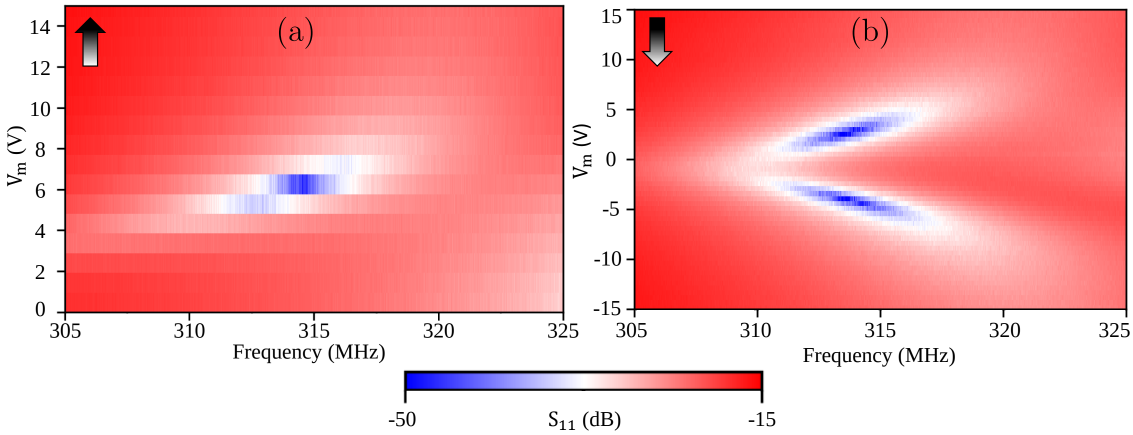

Figure 4.13: Plot of the measured reflection coefficient (S_{11}) as a function of frequency and V_{m}. (a) V_{m} is swept from 0 V to +15 V (forward sweep). (b)V_{m} is lowered from +15 V to −15 V (reverse sweep).

Similarly to the 1st generation device, after the application of negative voltages, the resonance is no longer retrievable (due to the permanent change in capacitance value). Therefore, the sample is given a thermal cycle up to room temperature and cooled to 10 mK to restore its original state. The signal is rediscovered with a slight change in frequency, as shown in figure 4.14a. Since it is known from the previous experiment, I focus on the voltage region where the perfect matching is obtained. In figure 4.14a, at $V_{\mathrm{m}} = 5.5\,\mathrm{V}$, the reflection is minimum. This result is reproducible as long as the negative-polarity voltage is not applied. Simultaneously, the values of C_{m} and C_{d} are measured for different V_{m} as shown in figure 4.14b and 4.14c. Ideally, the change in C_{d} with V_{m} should be zero. But figure 4.14c shows a slight change in C_{d} with V_{m}. This behaviour can be explained by the impact of stray field as discussed in chapter 3

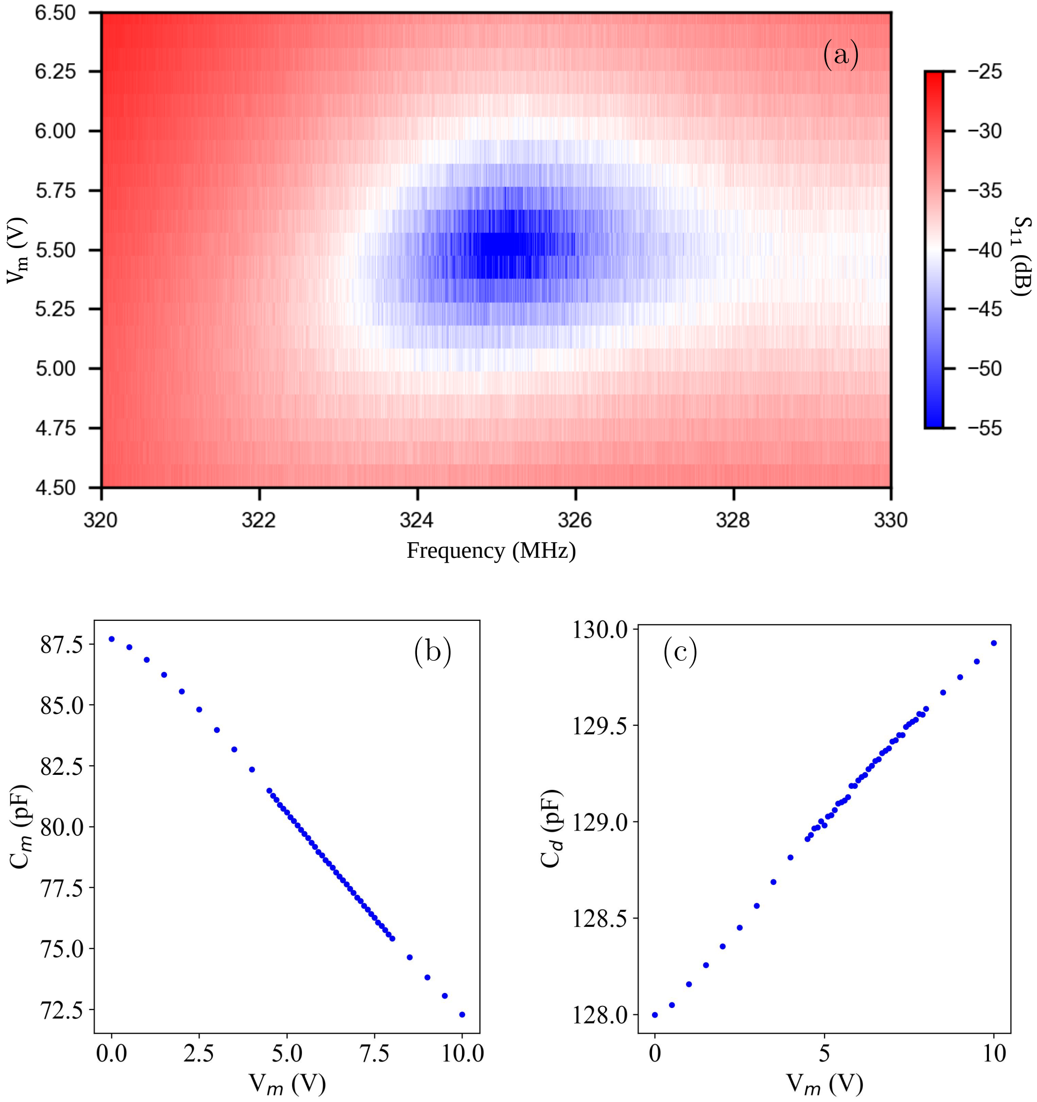

Figure 4.14: Perfect impedance match point where the reflected signal is minimum. (a) Reproducible colour plot of S_{11} as a function of V_{m} and frequency. (b) and (c) show the impact of V_{m} on C_{m} and C_{d}, respectively when $V_{\mathrm{d}} = 0\,\mathrm{V}$.

Now it is time to assess the critical coupling point by tuning C_{d}. In figure 4.15 V_{d} is varied from 0 V to +50 V. However, there is no change in the reflected signal for different values of C_{d}. This indicates that the value of C_{d} (even at $V_{\mathrm{d}} = 50\,\mathrm{V}$) is too high to have an effect on the reflected signal. This can be explained in the following way. The value of C_d (at $V_d = 0\,\mathrm{V}$) is almost 100 times larger than the value of C_s. C_d will have an impact on the reflected signal only when its value is comparable to C_s.

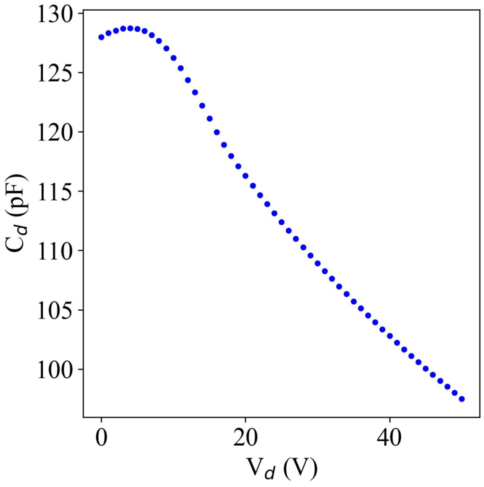

Figure 4.15: C_{d} as a function of V_{d} when $V_{\mathrm{m}} = 0\,\mathrm{V}$.

4.4 Conclusion

In this chapter a lumped element impedance matching network based on a quantum paraelectric material ($\mathrm{SrTiO_3}$) is thoroughly studied. Starting with a simulation for optimising the device parameters, this chapter ends with a promising demonstration of impedance matching. Therefore, the matching network is now ready to integrate with a high-impedance device. This chapter can be summarised as follows.

- The simulation in AWR Microwave Office software [78] gives insight into the functions of different elements in the matching network (that is, C_{s} controls the resonance frequency and C_{m} adjusts the impedance of the circuit).

- A tunable LC resonator is successfully made out of $SrTiO_3$, whose frequency can be tuned by voltage. The experimental data are in good agreement with the LGD theory [45].
- Finally, a successful impedance matching device based on $SrTiO_3$ has been demonstrated, which is capable of adjusting the impedance of the circuit. Since this matching network is controlled by a dc voltage, one must be careful about applying a dc voltage to this material due to its hysteric nature in polarizability. It is shown that the impedance matching condition is achievable by the voltage of both polarity. Therefore, it is better to avoid applying a negative voltage since it has more impact than a positive voltage on changing the initial polarisation state.

In general, this chapter is about optimising readout sensitivity to changes in device impedance, which is very useful for studying high-impedance devices (such as quantum dots [28–30]). The response of the quantum paraelectric material to the high-frequency electromagnetic field is investigated in the next chapter.

Chapter 5

Wave mixing in a quantum paraelectric medium

The study of quantum paraelectric (QPE) materials can now be extended to the wave mixing regime to observe the nonlinear response to a radio frequency (rf) signal. This chapter is focused on mixing two high-frequency electromagnetic waves by leveraging the intrinsic nonlinearity of these materials. This is a step towards parametric amplification. It allows for on-chip frequency generation and modulation/demodulation. The experiment is performed by probing a superconducting

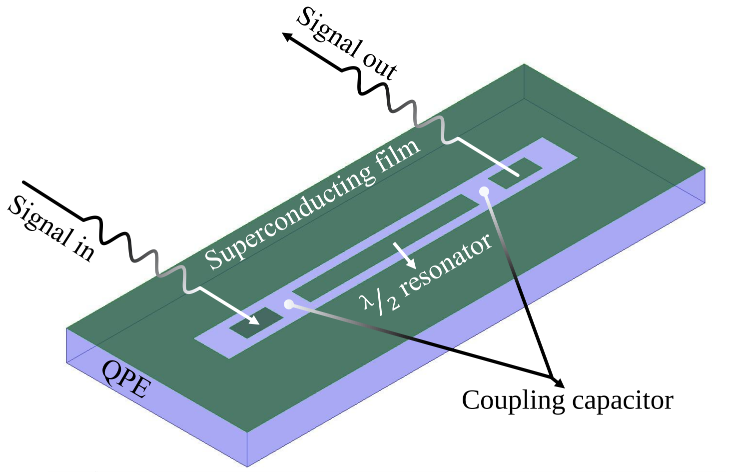

Figure 5.1: A $\lambda/2$ CPW resonator on a QPE chip capacitively coupled to both the input and output ports.

half-wave ($\lambda/2$) coplanar waveguide (CPW) resonator in a transmission mode setup (figure 5.1). In a $\lambda/2$ resonator, electromagnetic waves inserted to the input port travel through the central strip-line and exit from the output port only when the electromagnetic wavelength is twice the length of the strip-line or a multiple.

5.1 Simulation of a CPW resonator in ANSYS

In order to guide the design of the mixer this section describes the simulation of a superconducting $\lambda/2$ CPW resonator on top of a quantum paraelectric material to evaluate the S-parameters by HFSS (high frequency structure simulator) in the ANSYS Electronic Desktop [80]. The fundamental frequency of a $\lambda/2$ CPW resonator [82] is

$$f_0 = \frac{c}{\sqrt{\epsilon_{\text{eff}}}}\frac{1}{2l} \tag{5.1}$$

where c is the speed of light, l is the length of the resonator, $\epsilon_{\text{eff}} = \frac{\epsilon_{\text{r}}+1}{2}$ is the effective dielectric constant, and ϵ_{r} is the dielectric constant of the substrate. Equation 5.1 is

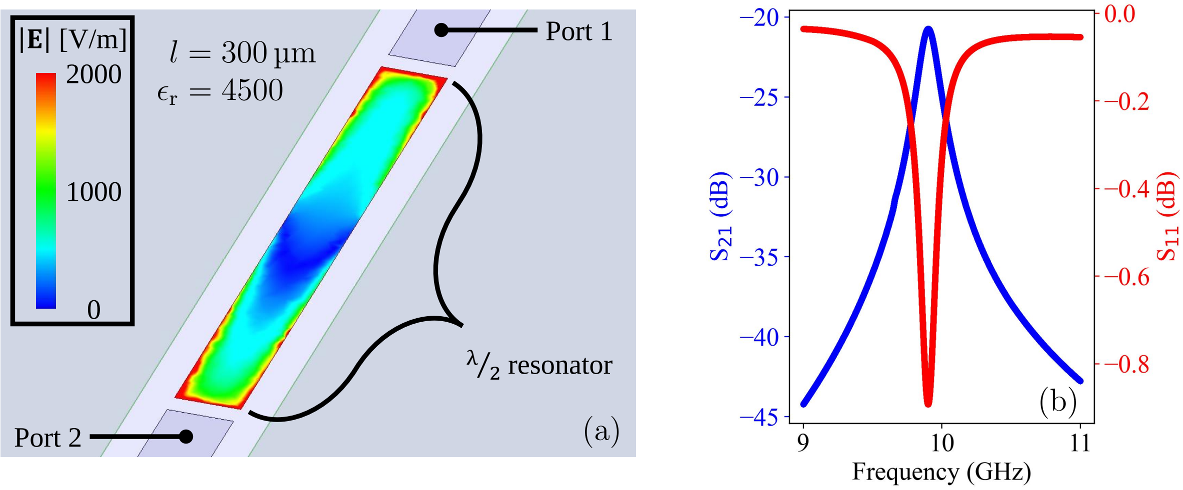

Figure 5.2: Products of a HFSS simulation of a $\lambda/2$ CPW resonator model in ANSYS. (a) Electric field distribution along the central strip-line. The intensity of the electric field is maximal at the ends while the minimum is located at the center. (b) S-parameters plot. The peak in S_{21} and the dip in S_{11} indicate the fundamental resonance $\sim 10\,\text{GHz}$ (expected at 10.5 GHz using equation 5.1).

true for a one-dimensional model, and assuming ϵ_r is constant. A detailed discussion of a CPW resonator can be found in appendix B.

Description of the model [figure 5.2]: The length of the resonator is 300 µm. The substrate is potassium tantalate ($\mathrm{KTaO_3}$) with a uniform dielectric constant $\epsilon_\mathrm{r} = 4500$. The thickness of the substrate is 500 µm. The resonator is coupled to the input and output ports by 5 µm gap capacitors. The width of the strip-line is 30 µm and the ground plane spacing is 15 µm.

Figure 5.2 contains the simulation results of the electric field distribution and S-parameters. An electromagnetic wave is sent to port 1 and received from port 2. The transmission is highest at resonance. Therefore, for all frequencies except f_0, the value of the transmission coefficient (S_{21}) should ideally be zero and at f_0, S_{21} should have the highest value. On the other hand, the reflection coefficient (S_{11}) should be minimal at f_0.

As shown in figure 5.2a, the electric field distribution on the resonator agrees with the theory that says that for a $\lambda/2$ resonator, the voltage is zero at the center of the strip-line while the maximum voltage is experienced on both ends. Figure 5.2b demonstrates S_{21} and S_{11} of the resonator for a frequency sweep from 9 to 11 GHz. The maximum S_{21} or the minimum S_{11} indicates that the fundamental mode (f_0^{300}) for a 300 µm long resonator is ~ 10 GHz. Hence for a 30000 µm long resonator, the resonance frequency is (using equation 5.1),

$$f_0^{30\mathrm{k}} = f_0^{300} \times \frac{300}{30,000} \simeq 100\,\mathrm{MHz} \tag{5.2}$$

Possible conflicts may occur between the simulated model and a practical device for the following reasons – (1) The fundamental resonance frequency (f_0) could be different depending on the dielectric constant of the substrate. (2) The loaded quality factor ($Q_\mathrm{L} = f_0/\Delta f_\mathrm{FWHM}$, where FWHM stands for full-width half maxima) may vary depending on the coupling strength (alternatively coupling capacitor). (3) The insertion loss may differ for different values of the loss tangent of the substrate at different frequencies.

5.2 Electrostatic simulation in MATLAB

In this section the discussion highlights the response of a CPW resonator on $KTaO_3$ (KTO) when the central strip-line experiences a dc electric field. As shown in chapter 3, the application of a dc voltage modifies the dielectric constant, resulting in the change of capacitance between the central strip-line and the ground planes (figure 5.3b). To simulate this, I use a 2-dimensional model based on the Landau-Ginzburg-Devonshire (LGD) theory [81], in which the dielectric constant of KTO ($\epsilon_{\mathrm{r}}^{\mathrm{KTO}}$) is a function of an electric field (E).

$$\epsilon_{\mathrm{r}}^{\mathrm{KTO}}(E) = 1 + \frac{\epsilon_{\mathrm{r}}^{\mathrm{KTO}}(0)}{[1+(E/E_0)^2]^{1/3}} \tag{5.3}$$

where E_0 is a tunability parameter of the dielectric constant for an applied electric field. This 2-dimensional model helps to know the value of dielectric constant everywhere inside the geometry (figure 5.3b) and the dependence of capacitance on voltage.

A MATLAB script is written to perform a 2-dimensional electrostatic simulation of a CPW resonator in a GROUND-VOLTAGE-GROUND configuration (figure 5.3b). The purpose is to analyse how the effective dielectric constant of $KTaO_3$ changes under various externally applied voltages. The simulation uses the Partial Differential Equation (PDE) Toolbox to solve for electric potential and electric field distribution and compute corresponding dielectric properties.

Geometry and model setup The dimensions of the simulation box, the coplanar structure and the mesh size are defined. An electrostatic model is initialised using createpde('electromagnetic','electrostatic'). The regions (vacuum and $KTaO_3$) are defined by constructing multiple rectangular blocks (upper and lower background layers, central signal line (voltage applied) and ground planes on either side of the signal line). The geometries are then assembled and combined using Boolean operations to form the final simulation domain.

Mesh generation A quadratic mesh is generated with defined mesh size in order to access each nodal point inside the geometry. The mesh elements and nodes associated with different faces are identified for post-processing and visualisation.

Material definition The materials for different regions are defined by their permittivities. The vacuum has a fixed permittivity while $KTaO_3$ is characterised by a nonlinear field-dependent permittivity (equation 5.3).

Boundary conditions and voltage sweep To simulate multiple bias conditions, a range of voltages is applied on the central strip-line. Boundary conditions are imposed on the edges representing the signal and ground planes.

Solving the model For each applied voltage, the electrostatic PDE is solved to obtain the electric potential distribution. From this solution, the nodal electric field is evaluated and the local field magnitude is used to determine the effective permittivity based on the nonlinear field-dependent dielectric model.

Post-processing Effective permittivity distribution is plotted as shown in figure 5.3b. In order to assess the voltage-dependent resonance frequency of the CPW resonator, energy stored per unit length (U_l) is calculated as follows.

$$U_l = \sum_i (\text{Energy density } (i) \times \text{Area}(i)) \tag{5.4}$$

We know, energy density for i-th node $= \frac{\epsilon_i E_i^2}{2}$, where ϵ_i is the dielectric constant at i-th node and E_i is the electric field at i-th node. Both ϵ_i and E_i are known from the PDE solution. Due to the quadratic mesh configuration, the area associated with i-th node is an area of a triangle. Thus, using equation 5.4 energy density is calculated by integrating the permittivity-weighted field energy over all the mesh elements. Since the resonance frequency of a CPW resonator is inversely proportional to the square root of the energy stored per unit length, figure 5.3a is plotted using equation 5.4 for different voltages.

This model helps to understand the nonlinear dielectric response of $KTaO_3$ under varying bias voltages. By simulating the structure of a CPW resonator, one can predict how the dielectric constant and hence the resonance frequency will respond to an applied electric field.

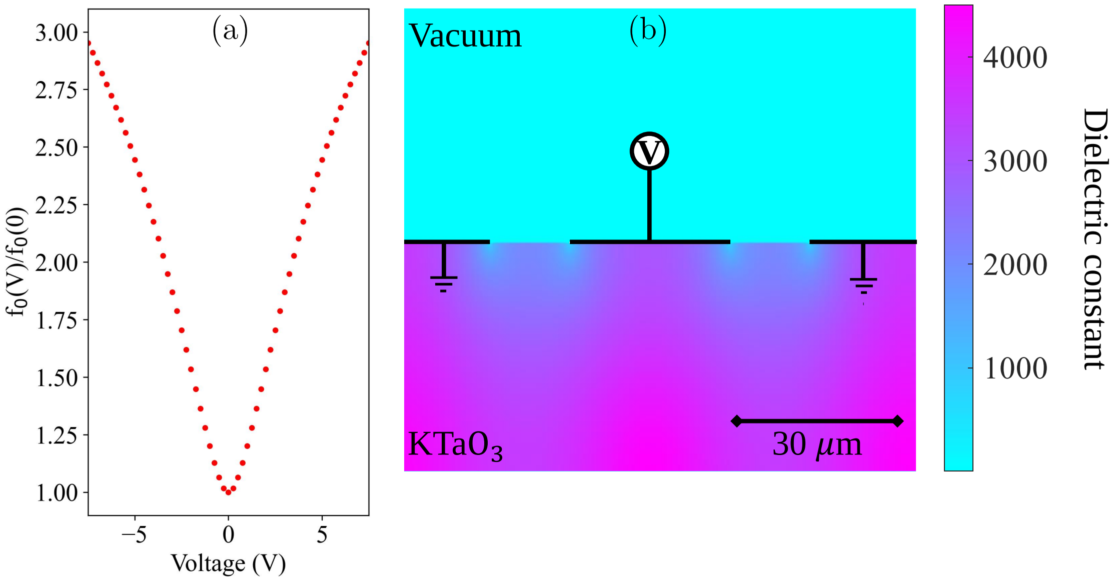

Figure 5.3: MATLAB simulation results for a 2-dimensional CPW model. (a) The tunability of the fundamental mode for different dc voltages is plotted where the voltage is applied on the central line. (b) Cross-sectional view of the CPW model. The colour bar refers to the dielectric constant of the substrate ($KTaO_3$) under an applied dc voltage of 5 V.

A complete MATLAB code of the model is given in appendix D. Figure 5.3a shows how the fundamental frequency (f_0) of the CPW resonator changes with the applied voltage. In summary, the simulation results show how the dielectric constant and consequently the resonance frequency can be varied with voltages in a controlled way. This analysis would be beneficial for assessing 3-wave mixing in quantum paraelectric materials.

5.3 Analytical optimisation of device parameters

This section tells us how to find the optimised parameters such as the length of the resonator, the value of coupling capacitance.

5.3.1 Length l of the resonator

The fundamental resonance frequency of a $\lambda/2$ CPW resonator is given by,

$$f_0 = \frac{c}{\sqrt{\epsilon_{\text{eff}}}} \frac{1}{2l} \tag{5.5}$$

Considering the available measurement setup, f_0 is desired to be 100 MHz. From [43], we know that below 4 K, the relative permittivity ($\epsilon_{\text{r}}^{\text{KTO}}$) of $KTaO_3$ (KTO) is approximately 4500. Hence, the effective relative permittivity is given by,

$$\epsilon_{\text{eff}} = \frac{\epsilon_{\text{r}}^{\text{KTO}} + 1}{2} \simeq 2250 \tag{5.6}$$

Therefore, for $f_0 = 100\,\text{MHz}$ the length of the resonator required is $\sim 31.5\,\text{mm}$.

5.3.2 Coupling capacitance C_{K} for critical coupling

The loaded quality factor (Q_{L}) of a system is dominated by either internal (Q_{int}) or external (Q_{ext}) quality factor depending on the coupling condition (see appendix B for a detailed discussion), as shown in equation 5.7.

$$\frac{1}{Q_{\text{L}}} = \frac{1}{Q_{\text{int}}} + \frac{1}{Q_{\text{ext}}} \tag{5.7}$$

At critical coupling, $Q_{\text{ext}} = Q_{\text{int}}$. The loss tangent ($\tan\delta$) of a resonator, which incorporates both surface losses and dielectric losses can interchangeably be used for $\frac{1}{Q_{\text{int}}}$. An earlier experiment [44] shows that at 3 GHz, $\tan\delta$ of $KTaO_3$ ($\tan\delta_{\text{KTO}}$) is 4.2 x 10 $^{-5}$ at 5.4 K. Assuming this is true for 100 MHz at 10 mK, the internal quality factor is given by,

$$Q_{\text{int}} = \frac{1}{\tan\delta_{\text{KTO}}} = 23,800 \tag{5.8}$$

Hence, at critical coupling, $Q_{\text{int}} = Q_{\text{ext}} = 23,800$. The coupling capacitance ($\mathrm{C_K}$) at each port for a two-port circuit is [82]

$$C_{\mathrm{K}} = \frac{\sqrt{\pi/Q_{\text{ext}}}}{2\omega_0 Z_0} \tag{5.9}$$

where Z_0 is the characteristic impedance of the resonator which depends on the relative permittivity of the substrate ($\epsilon_{\mathrm{r}}^{\mathrm{KTO}}$), thickness of the substrate (t), the trace width (w) and the ground plane spacing (s). For $\epsilon_{\mathrm{r}}^{\mathrm{KTO}} = 4500$, $w = 30\,\mu\mathrm{m}$, $s = 15\,\mu\mathrm{m}$ and $t = 0.5\,\mathrm{mm}$, the characteristic impedance (Z_0) is $2.5\,\Omega$ (calculated using an online tool [83]). For overcoupling, I choose the coupling capacitance to be 20 pF. The reason behind choosing overcoupling is the uncertainty in the value of $\epsilon_{\mathrm{r}}^{\mathrm{KTO}}$. The dimensions of the coupling capacitor are optimised for $\epsilon_{\mathrm{r}}^{\mathrm{KTO}} = 4500$ in order to achieve critical coupling. If the value of $\epsilon_{\mathrm{r}}^{\mathrm{KTO}}$ is less than 4500, for a similar geometrical structure, the capacitance value decreases, resulting in undercoupling.

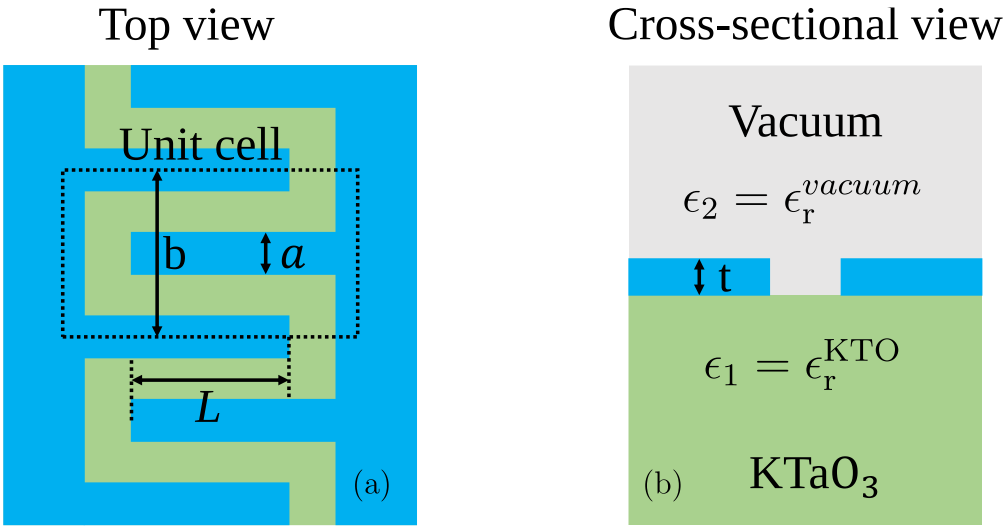

Figure 5.4: Schematic view (a: top view; b: cross-sectional view) of an interdigitated capacitor on a $\mathrm{KTaO_3}$ chip.

I choose interdigitated capacitors to connect the resonator to $50\,\Omega$ matched lines. The expression for an interdigitated capacitance [84] with N fingers of length L is

$$C_{\text{tot}} = (N-1)LC_{\text{uc}} \tag{5.10}$$

where

$$C_{\mathrm{uc}} = \epsilon_0(\epsilon_1 + \epsilon_2)\frac{K(\sqrt{1-(a/b)^2})}{K(a/b)} + 2\epsilon_0\epsilon_2\frac{t}{a} \tag{5.11}$$

where a, b, t, ϵ_1, and ϵ_2 are indicated in figure 5.4. $K(\star)$ is a complete elliptic integral of the first kind. For $a = 5\,\mu\mathrm{m}$, $b = 20\,\mu\mathrm{m}$ and $t = 200\,\mathrm{nm}$ the second term in equation 5.11 can be neglected. Therefore, to achieve, $C_{\mathrm{K}} = 20\,\mathrm{pF}$ with $C_{\mathrm{uc}} = 7 \times 10^{-8}\mathrm{F}$, I choose $N = 5$ and $L = 70\,\mu\mathrm{m}$.

5.4 Device design and fabrication

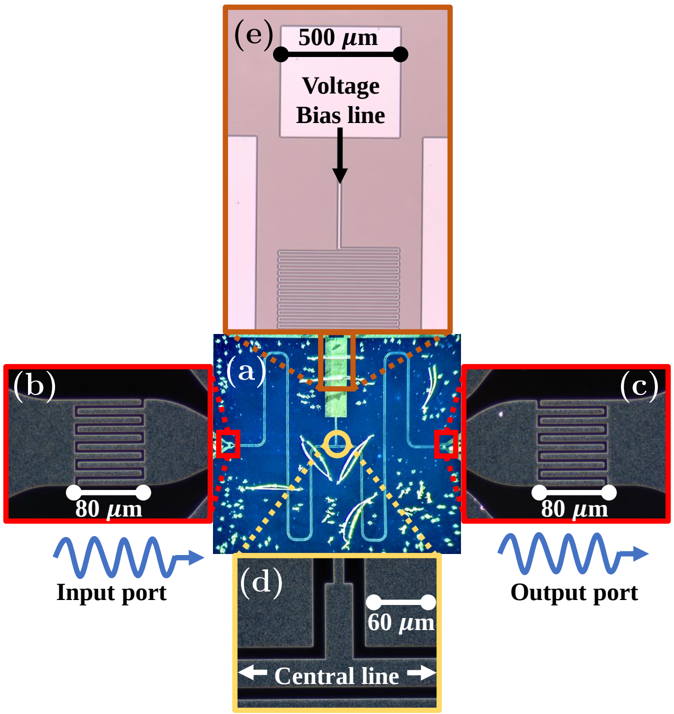

Figure 5.5: Overview and details about the device layout. (a) Photograph of the chip. (b), (c), and (d) are the darkfield images of the input port, the output port, and the center of the strip-line respectively. (e) Microscopic image of the voltage bias line.

The design of the superconducting $\lambda/2$ CPW resonator is based on the optimised parameters mentioned above. The resonator is made of superconducting thin film (Al) of thickness of 200 nm on top of a single-crystal 10 mm×10 mm×0.5 mm $KTaO_3$

chip. The length of the resonator is about 30 mm. The resonator is capacitively coupled to a 50 Ω matched line at both ends via interdigitated capacitors as shown in figure 5.5.

A voltage bias line is connected to the strip-line in the center. This is to apply a dc voltage on the central strip-line to change the effective dielectric constant. The fabrication recipe is described in detail in appendix C. The ground planes separated by the strip-line and the voltage bias line are connected by bonded wires.

5.5 Cryogenic characterisation

Initially, the resonator is characterised at 10 mK using a vector network analyser (VNA) to discover the fundamental resonance frequency, f_0 (expected at about 110 MHz). Figure 5.6 shows the data from a VNA where the fundamental resonance frequency (f_0) is found to be 126.264 MHz with a loaded quality factor (Q_L) of 676. Assuming Q_{int} = 23,800 [44], from equation 5.7, we know that the external quality

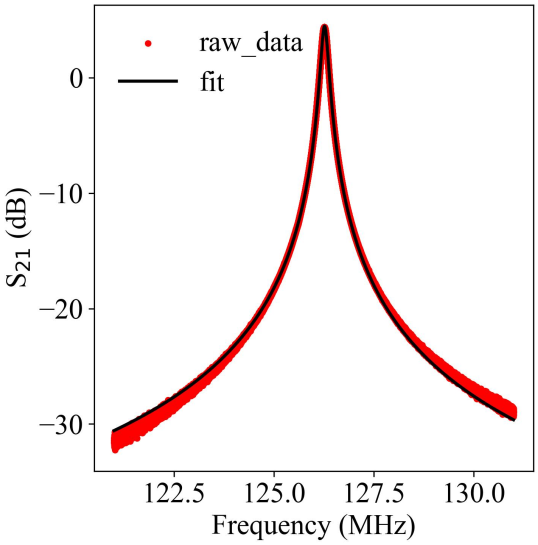

Figure 5.6: S_{21} transmission spectrum of a CPW resonator symmetrically coupled to both input and output lines. Data points (red) are fit with a Lorentzian line (black). The Lorentzian function looks like $S_{21} = 10\log_{10}\left(\frac{4Aw}{4(f-f_0)^2+w^2}\right) + y_0$ where $A = 3.592 \times 10^5$, $w = 1.868 \times 10^5$, $f_0 = 126.27 \times 10^6$, and $y_0 = -4.4$.

factor (Q_{ext}) is approximately 700. The measurement is performed with a signal power of -70 dBm at the input of the resonator.

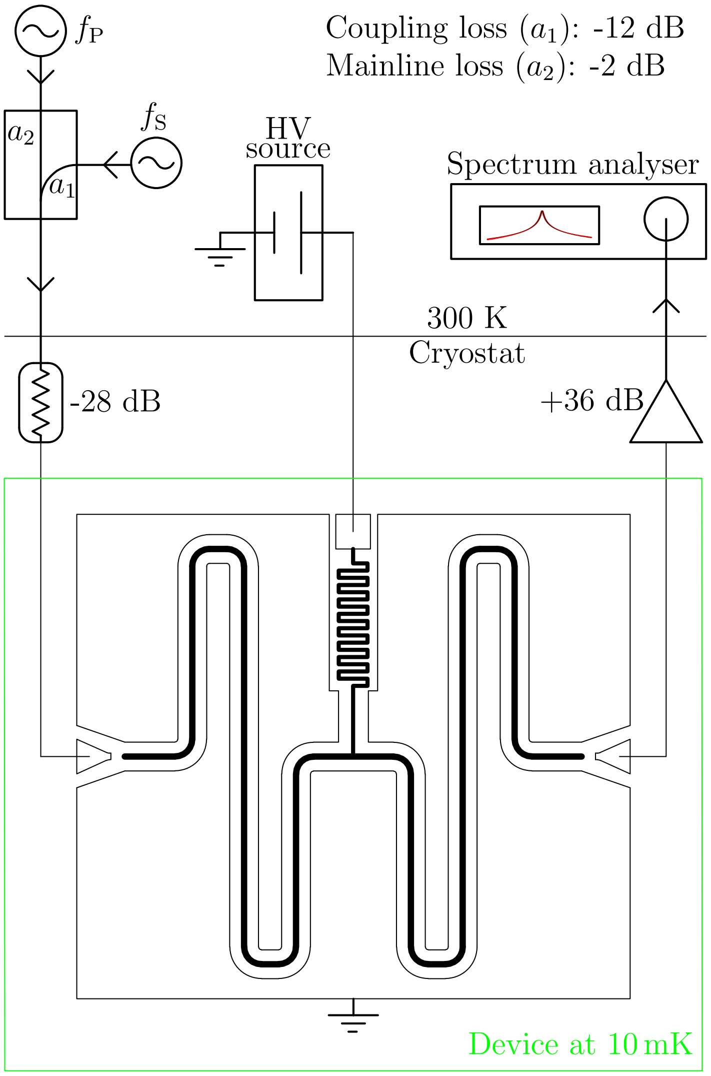

Figure 5.7: Experimental setup for wave mixing. The CPW resonator is coupled to an input line (with 28 dB attenuation) and a readout line (with 36 dB gain) via symmetrical interdigitated capacitors. A HV (high voltage) source is used to apply voltage on the central strip-line to tune f_0.

The device is then configured in a two-tone measurement setup as shown in figure 5.7 to explore nonlinear wave mixing in quantum paraelectric materials. Two electromagnetic waves (a strong pump tone and a weak signal) combined at room temperature are injected through a 28 dB attenuated coaxial cable to the input port of the resonator. The output port of the device is connected to a spectrum analyser via a 4 K HEMT (high electron mobility transistor) amplifier with a gain of 36 dB. For the 4-wave mixing scheme the high voltage source is set to 0 V while for 3-wave mixing the dc voltage is applied to the central strip-line through the voltage bias line as shown in figure 5.7.

5.5.1 4-wave mixing

Upon finding the resonance frequency, the device is now ready to explore wave mixing. The device is first examined for 4-wave mixing. I inject two tones, pump and signal. Typically, the pump tone is stronger than the signal tone. The frequency (f_P) of the pump tone is set to the fundamental mode of the resonator while the frequency (f_S) of the signal tone is swept around f_P. The spectrum at the output port is monitored by a spectrum analyser. The same process is run for different pump powers (P_P). The strength (P_S) of the weak signal tone is -100 dBm at the input of the resonator. As discussed in chapter 2, in 4-wave mixing the two tones generate an 'idler mode' of frequency f_I in such a way that their frequencies share the following relation,

$$2f_\mathrm{P} = f_\mathrm{S} + f_\mathrm{I} \tag{5.12}$$

Figure 5.8 is a graph for the power spectra for different weak signal frequencies (f_S) when the pump tone is set to f_0 (126.264 MHz) with a power of -55 dBm at the input of the resonator. From figure 5.8, it is evident that there appear idler modes associated with each weak signal frequency and they satisfy the 4-wave mixing condition,

$$|f_\mathrm{P} - f_\mathrm{S}| = \Delta f = |f_\mathrm{P} - f_\mathrm{I}| \tag{5.13}$$

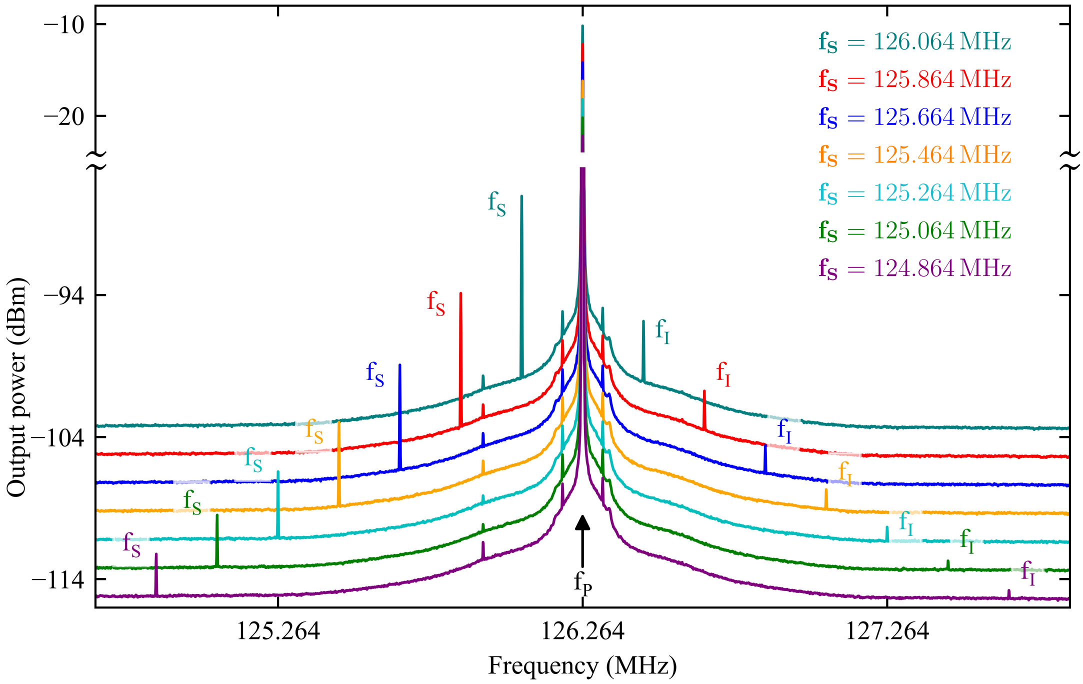

Figure 5.8: Demonstration of 4-wave mixing in quantum paraelectric material. The plot represents power spectra for different weak signal frequencies (f_S) when the pump tone is at f_0 (126.264 MHz) with a power of −55 dBm. The bottom trace (purple) shows the actual output power. Each subsequent trace is vertically offset by 2 dB from the one immediately below it to improve visibility. The appearance of the idler mode for each f_S in the presence of a strong pump tone is the evidence of 4-wave mixing. The red trace is plotted in figure 5.9.

To simplify the explanation, the red trace from figure 5.8 is drawn in figure 5.9. Figure 5.9 demonstrates the appearance of an idler mode at $f_I = 126.664$ MHz for a weak signal $f_S = 125.864$ MHz satisfying equation 5.13 with $\Delta f = 400$ kHz. This plot confirms that a quantum paraelectric material ($KTaO_3$) can exhibit the phenomenon of 4-wave mixing at 10 mK in the MHz frequency range with a certain pump tone strength.

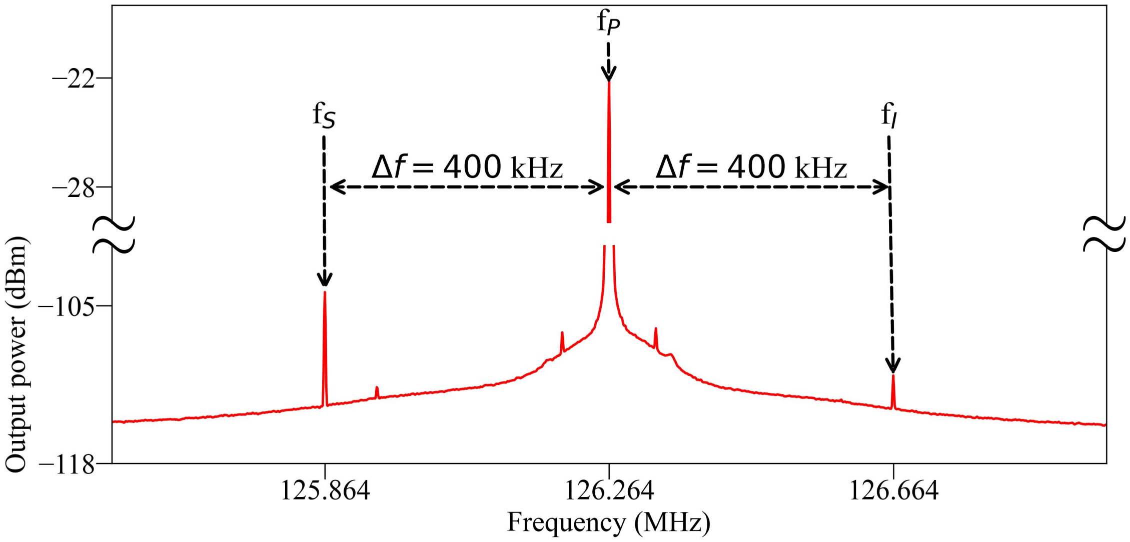

Figure 5.9: Power spectrum for a particular weak signal frequency ($f_\mathrm{S} = 125.864\,\mathrm{MHz}$) with $P_\mathrm{P} = -55\,\mathrm{dBm}$ and $f_\mathrm{P} = 126.264\,\mathrm{MHz}$. The plot shows the existence of the idler mode (f_I) at 126.664 MHz.

The idler modes remain prominent even at higher pump powers. Figure 5.10 depicts a measurement in which the pump power is increased to investigate parametric amplification in the 4-wave mixing regime. The gain in the weak signal

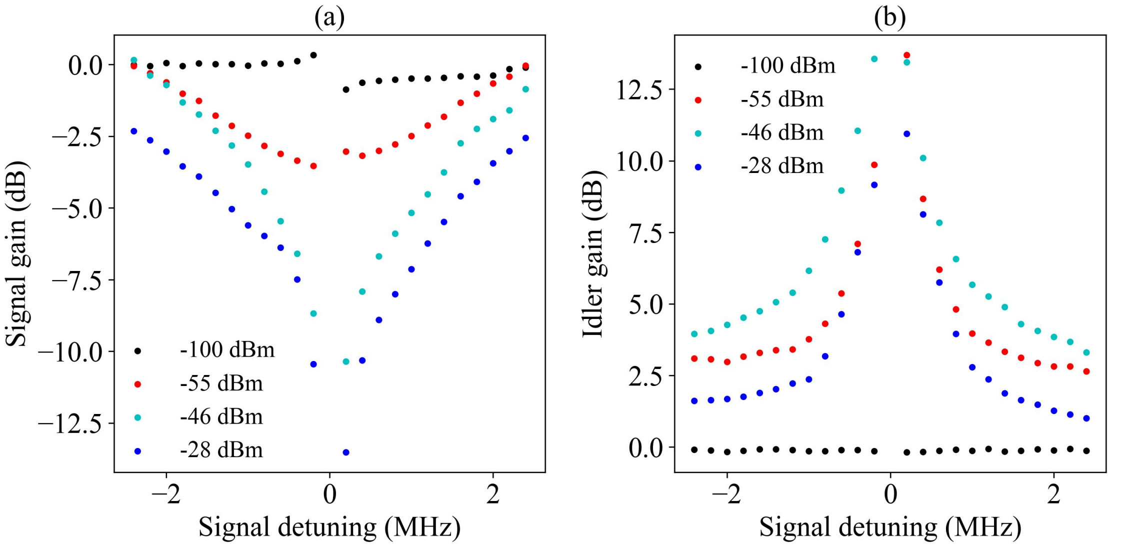

Figure 5.10: Gain as a function of signal detuning from the pump tone frequency, f_P (or f_0). (a) and (b) presents gain in weak signal and in idler mode, respectively, for different pump powers as indicated in the legends.

(defined as the difference between the output powers at f_S with pump on and off) and the gain in the associated idler mode (defined as the difference between the output powers at f_I with pump on and off) with respect to the signal detuning from f_P (or f_0) are plotted in figure 5.10 for different pump powers (P_P). When $P_\mathrm{P} = -100\,\mathrm{dBm}$, there is no sign of gain in both weak signal and idler mode. At $P_\mathrm{P} = -55\,\mathrm{dBm}$, the idler mode appears with a significant gain for different signal detunings. But the weak signal starts to lose its power. This may seem to be because the energy is transferred from the signal tone to the idler mode. The highest gain of the idler mode is observed at $P_\mathrm{P} = -46\,\mathrm{dBm}$ while the power loss of the signal mode continues for higher values of P_P. The gain of the idler mode drops drastically at $P_\mathrm{P} = -28\,\mathrm{dBm}$.

This could be due to two reasons.

1. The power of the signal at the input of the 4 K HEMT (high electron mobility transistor) amplifier is near the saturation level, and this causes an unstable (unreliable) gain from the HEMT amplifier.
2. The pump power is so high that the signal starts to leak to the ground plane, resulting in a lesser amount of energy propagation.

Since any pump power above $-55\,\mathrm{dBm}$ results in signal loss, it is not possible to observe if any amplification occurs at higher pump power. Therefore, it can be concluded that even though the paraelectric material ($\mathrm{KTaO_3}$) exhibits 4-wave mixing, for this specific design of the resonator and the pumping scheme, it is not possible to achieve the right nonlinear regime where the resonator can be characterised as a parametric amplifier.

5.5.2 Generation of a frequency comb

The experiment is pushed further by increasing the strength of the signal tone. The measurement is carried out in the following way. For a strong signal with a power of $-70\,\mathrm{dBm}$ (at the input of the resonator), the pump tone is set to the fundamental mode. The signal is detuned by $100\,\mathrm{kHz}$ from f_P and the measurement is performed over a range of pump powers (P_P) from -70 to $-50\,\mathrm{dBm}$, while monitoring the output powers in a spectrum analyser.

The results are shown in figure 5.11. Initially, when the pump power is fixed at $-70\,\mathrm{dBm}$, the spectrum analyser witnesses the onset of a comb-like resonance structure (figure 5.11a) with $100\,\mathrm{kHz}$ spacing. Further increase in P_P strengthens the comb resonance. At $P_\mathrm{P} = -60\,\mathrm{dBm}$, the maximum number of comb teeth appears in the frequency spectrum, as shown in figure 5.11c. This power is the critical power for which the comb resonance becomes the most prominent. For P_P above $-60\,\mathrm{dBm}$, the comb structures gradually disappear and the measurement is stopped at $P_\mathrm{P} = -50\,\mathrm{dBm}$ (figure 5.11b) as the saturation power level of the HEMT amplifier is reached.

Figure 5.11c describes a control experiment in order to investigate the origin of the frequency comb. Initially, two tones, pump and signal, are injected into the input of the resonator device on KTAO$_3$, while the output of the resonator is connected to a HEMT amplifier at $4\,\mathrm{K}$ as shown in Figure 5.7. For $P_\mathrm{P} = -60\,\mathrm{dBm}$, a frequency comb appears in the power spectrum. Then a similar measurement is made after the resonator is replaced with a $50\,\Omega$ matched coaxial cable (with attenuation $< 0.5\,\mathrm{dB}$). Since the resonator device is removed, the injected tones are directly amplified by the HEMT amplifier. But there is no sign of a comb-like structure in the power spectrum. Therefore, from the comparison in figure 5.11c, it can be said that the generation of comb resonances is due to the nonlinear wave mixing in the superconducting resonator made of aluminium (Al) on the quantum paraelectric chip (KTaO$_3$). The appearance of a frequency comb is reported in an earlier experiment [85] in a superconducting resonator made of niobium titanium

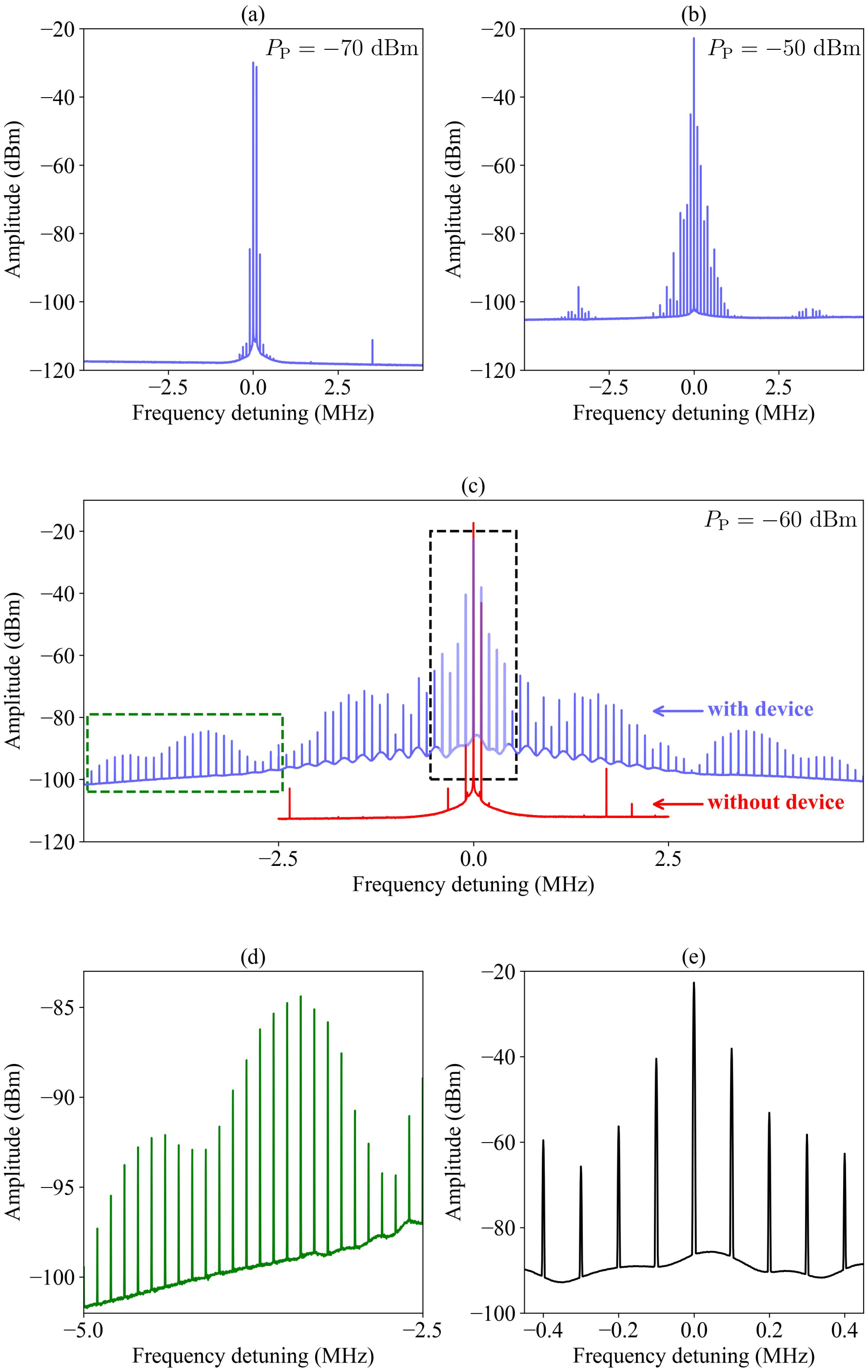

Figure 5.11: Frequency comb for different pump powers with $P_S = -70\,\text{dBm}$. (a) Onset ($P_P = -70\,\text{dBm}$) & (b) over-pumped version ($P_P = -50\,\text{dBm}$) of the frequency comb. (c) Frequency comb at $P_P = -60\,\text{dBm}$ with and without the resonator device. (d) & (e) are the data (with device) inside the green and black box of (c) respectively.

nitride (NbTiN) due to the kinetic inductance. As the resonator in my device is made of Al (the least favorable material for applications related to kinetic inductance due to its very low kinetic inductance value [82, 86, 87]), it is likely that the mechanism for wave mixing (or the generation of comb resonance) is the intrinsic nonlinearity of the quantum paraelectric medium ($KTaO_3$). The nature of this comb resonance is very similar to the optical frequency comb observed in a crystalline whispering gallery mode (WGM) resonator [88], a monolithic microresonator [89], and a soliton crystal comb [90], apart from the operating frequency range.

Figure 5.11d shows the wavy nature of the comb teeth in amplitude that has been observed in the soliton crystal [90] and a perfectly tuned crystalline calcium fluoride WGM resonator [88].

Figure 5.11e validates the equidistant frequency spacing of the comb teeth. The mechanism behind the comb generation can be illustrated in the following way. Due to 4-wave mixing, the pump tone (f_P) and the signal tone (f_S) give rise to an idler mode (f_I). Now, due to non-degenerate 4-wave mixing, the signal and the idler produce higher sidebands, which coalesce into a continuous frequency comb. The frequency relation for the higher order sidebands can be written in the following way

$$2^{\mathrm{nd}}\ \text{order signal},\ f_{\mathrm{S2}} = f_\mathrm{P} + f_\mathrm{S} - f_\mathrm{I} = f_\mathrm{P} + 2\Delta f \tag{5.14}$$

where $f_\mathrm{P} - f_\mathrm{S} = \Delta f = f_\mathrm{I} - f_\mathrm{P}$. Similarly,

$$2^{\mathrm{nd}}\ \text{order idler},\ f_{\mathrm{I2}} = f_\mathrm{P} + f_\mathrm{I} - f_\mathrm{S} = f_\mathrm{P} + 2\Delta f \tag{5.15}$$

Hence,

$$|f_\mathrm{P} - f_{\mathrm{SN}}| = N\Delta f = |f_\mathrm{P} - f_{\mathrm{IN}}| \tag{5.16}$$

where N is the order number. In brief, increasing the pump power leads to a cascading process which results in generating a frequency comb with multiple equispaced signal and idler sidebands.

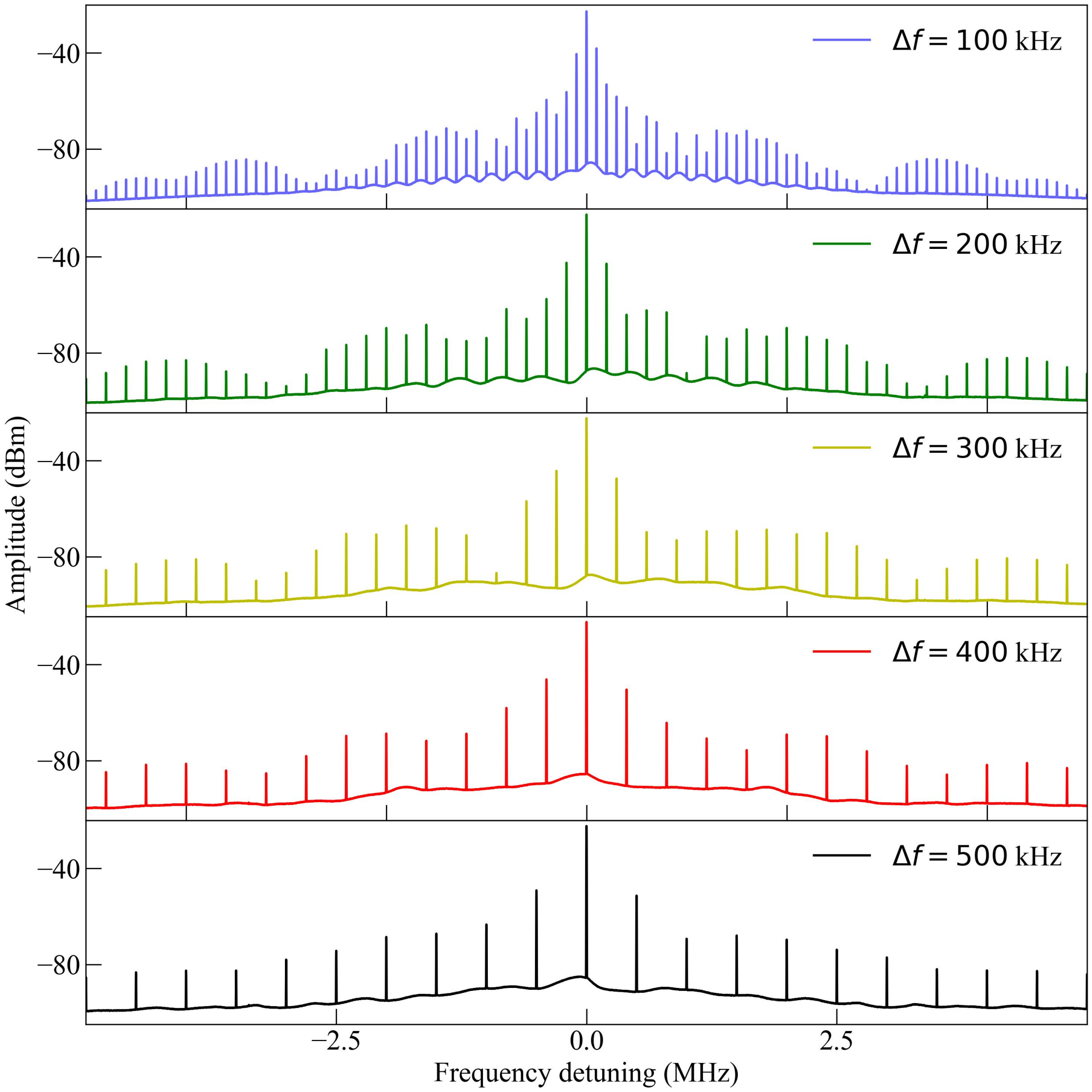

Figure 5.12: Pattern of the frequency comb around $f_\mathrm{P} = 126.264\,\mathrm{MHz}$ for five different signal detunings (or frequency spacing, Δf) at $P_\mathrm{P} = -60\,\mathrm{dBm}$.

Figure 5.12 provides an overview of how the shape of the frequency comb is modified with different frequency spacing (Δf). The data obtained are for $P_\mathrm{P} = -60\,\mathrm{dBm}$ at $f_\mathrm{P} = 126.264\,\mathrm{MHz}$ and $P_\mathrm{S} = -70\,\mathrm{dBm}$.

Figure 5.13 is plotted with the same parameters [$f_\mathrm{P} = 126.264\,\mathrm{MHz}$, $P_\mathrm{P} = -60\,\mathrm{dBm}$, signal detuning $(\Delta f) = 100\,\mathrm{kHz}$] as figure 5.11c, while measuring near 1st ($2f_\mathrm{P}$) and 2nd ($3f_\mathrm{P}$) harmonics of the pump tone. Although the amplitudes are different, both show a similar frequency comb pattern as in the fundamental mode (f_P).

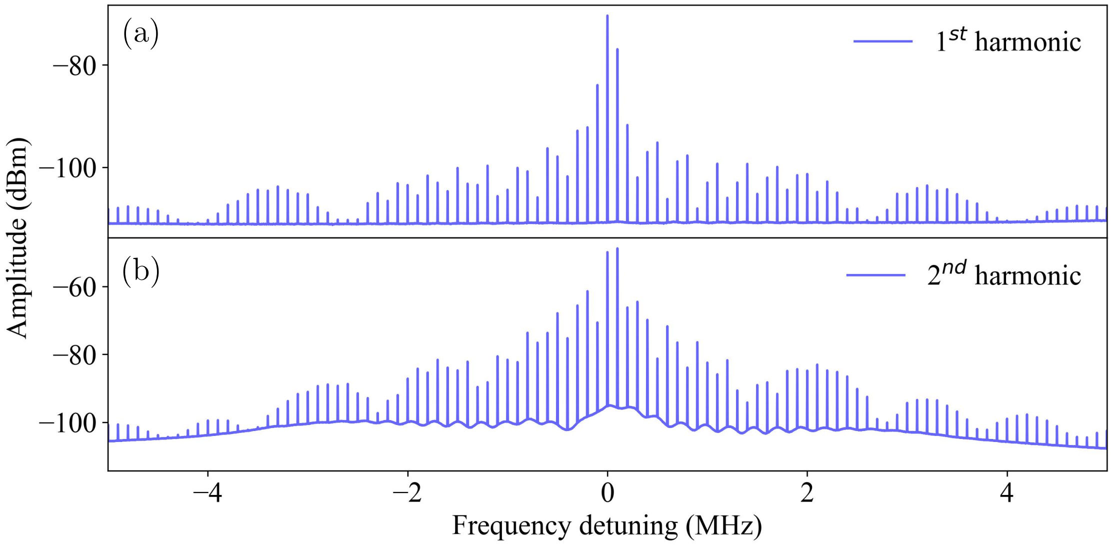

Figure 5.13: Overview of the generation of frequency comb at higher harmonics of the pump frequency ($f_\mathrm{P} = 126.264\,\mathrm{MHz}$) for $P_\mathrm{P} = -60\,\mathrm{dBm}$ and $\Delta f = 100\,\mathrm{kHz}$. (a) 1st harmonic ($2f_\mathrm{P} = 252.528\,\mathrm{MHz}$). (b) 2nd harmonic ($3f_\mathrm{P} = 378.792\,\mathrm{MHz}$).

The pump tone is also set to an off resonance frequency ($f_\mathrm{P} = 160\,\mathrm{MHz}$) where the strength of the transmitted wave is much weaker than that of the on resonance. Figure 5.14 is a proof that the generation of the frequency comb also occurs at an off-resonance frequency.

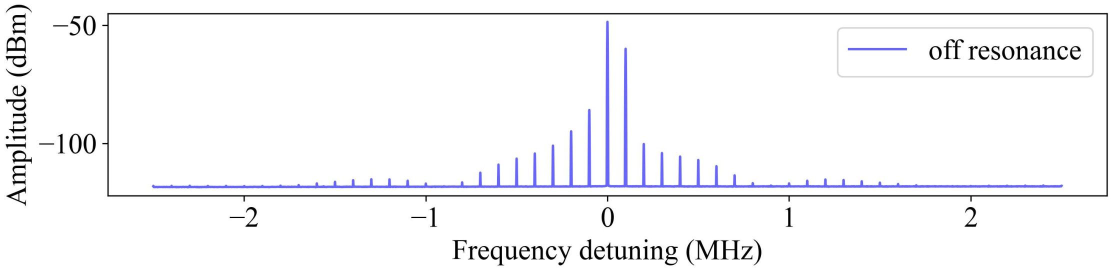

Figure 5.14: Nature of the frequency comb at an off resonance frequency of 160 MHz for $P_\mathrm{P} = -60\,\mathrm{dBm}$ with $\Delta f = 100\,\mathrm{kHz}$.

5.6 Conclusion

Quantum paraelectricity is probed by a superconducting $\lambda/2$ CPW resonator in this chapter. The successful fabrication of an aluminium resonator on $KTaO_3$ with optimised parameters, obtained from simulations, is followed by cryogenic characterisations at 10 mK. The resonator is investigated for nonlinear wave mixing via two-tone measurement. The chapter wraps up with a few key findings that make research in quantum paraelectric materials particularly fascinating.

- First, the material's Kerr nonlinearity allows the resonator to participate in a 4-wave mixing process. Therefore, a signal tone and a pump tone interact in the nonlinear medium and create an idler mode. This property of the material is advantageous for developing an on-chip cryogenic mixer.
- The device is then further investigated for parametric amplification with higher pump power in the 4-wave mixing regime. But this results in an ohmic leakage, and as a consequence the signal leaks to the ground. Therefore, with the current design of the resonator, it is not possible to inject higher pump power.
- The device has yet to be explored in the 3-wave mixing regime. For operating the device in 3-wave mixing mode, a dc voltage is required to be applied on the central strip-line through the voltage bias line as shown in figure 5.7. In this way, the system can be driven from the centro-symmetric part to the nonlinear part of the energy-voltage curve. We discussed in chapter 3 that for a gap smaller than 15 µm, dc current leaks through. Since the gap in the coupling capacitor is 5 µm in this design, it is not possible to apply a dc voltage on the strip-line. The raises a need for a new design which is discussed in chapter 6.
- Furthermore, it is observed that in the 4-wave mixing process when a strong signal tone is injected with the pump tone, it produces a frequency comb. This could potentially be useful in the field of quantum metrology in the radio frequency range.

Thus, this chapter ends with exciting experimental results and leaves some open questions and scope for future improvement.

Go to Contents↑

Chapter 6

Conclusion and future directions

This chapter summarises the thesis while underlining the experimental results and the scope of improvements of the devices described in different chapters. Quantum paraelectricity at low temperatures is studied by electrostatic characterisation of a concentric planar capacitor in chapter 3. The study tells us that a quantum paraelectric material ($SrTiO_3$) can be used to develop a cryogenic on-chip variable capacitor leveraging its two unique characteristics at low temperatures, namely a relatively high dielectric constant and electric field-tunable permittivity. However, it also reveals that for too small gap between the electrodes, beyond a certain voltage, a conductive path opens up, resulting in a leakage current. The threshold voltage (at which the current starts leaking) depends on the last electric field experienced by the substrate. Furthermore, the stray field has a large impact on the adjacent devices separated by $\sim 2\,\mathrm{mm}$.

Chapter 3 also tries to understand the dependence of temperature on the tunability of the dielectric constant and the mechanism of restoring the initial polarisation state. A further study could be carried out to understand the restoring mechanism in which the substrate is depolarised with a series of descending voltage sweeps (as shown in figure 6.1) instead of removing the electric field at once at low temperatures. This could potentially replace the conventional way (thermal cycle up to room temperature, which is very time-consuming) of retrieving the initial state of the quantum paraelectric materials.

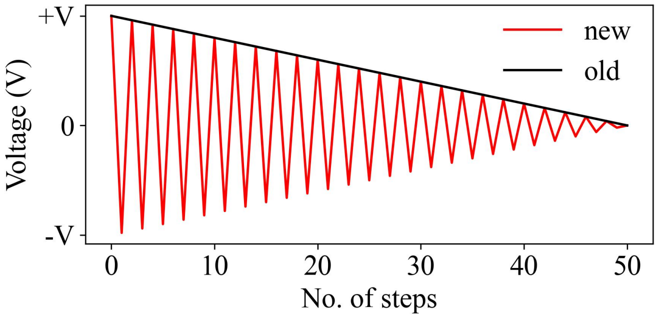

Figure 6.1: Depolarisation scheme (new: proposed way, old: discussed in chapter 3) for restoring the initial state, avoiding thermal cycles.

The discussion in chapter 4 focuses on the response of the quantum paraelectric material (SrTiO$_3$) when it experiences both dc and high-frequency signals at the same time. The investigation is conducted using a lumped element impedance matching network. The study shows the evolution of the devices, starting with an initial demonstration of a tunable LC resonator and ending with a successful impedance matching device. However, there is scope to improve the performance of matching devices even further by replacing the resistive conducting line with a superconducting line (Nb), as shown in figure 6.2.

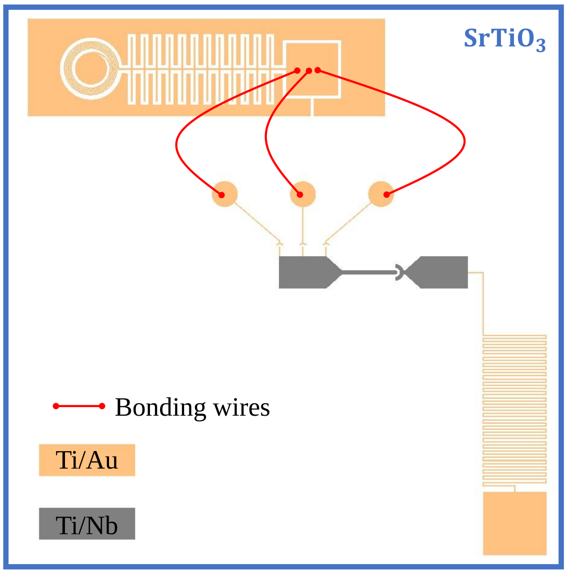

Figure 6.2: Proposed design of an impedance matching device.

Chapter 5 highlights the response of a quantum paraelectric material ($KTaO_3$) while interacting with two high-frequency signals. The quantum paraelectricity is probed by a superconducting half-wave coplanar waveguide resonator fabricated on top of $KTaO_3$. Initially, the material is characterised for the 4-wave mixing process and then used for generating a frequency comb. The study is conducted further towards parametric amplification in a 4-wave mixing regime. Unfortunately, no amplification is observed due to the limitations of the design of the device and the driving (pumping) scheme. However, the material has yet to be explored in the 3-wave mixing regime which requires some modifications in the experimental setup and device design, as depicted in figure 6.3.

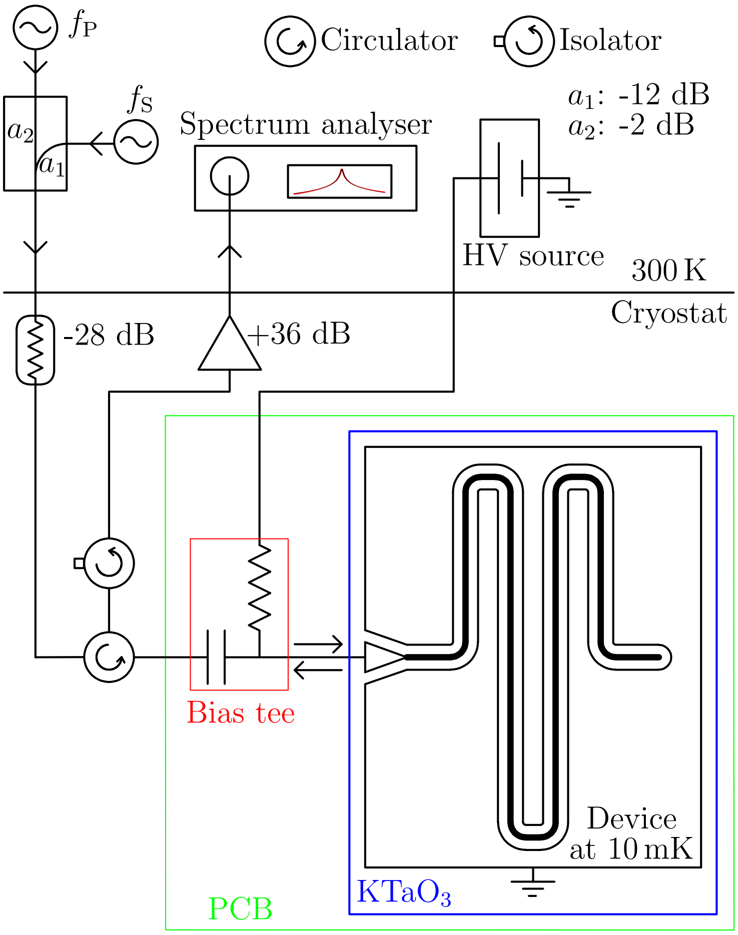

Figure 6.3: Proposed experimental setup for conducting 3-wave mixing process in a reflectometry mode to investigate parametric amplification.

This thesis contains a detailed discussion on the dielectric and high-frequency response of the quantum paraelectric materials in different situations (such as interaction with a static electric field, interaction with both the dc signal and the high-frequency signal, and interaction with two high-frequency tones) and concludes with the future directions of further investigations on improving the devices' performances. The experimental result shows the success of developing an on-chip impedance matching device using this material. Furthermore, the study identified its capability for wave mixing as a step toward parametric amplification. However, exploring the 3-wave mixing process could unveil the potential of this material to be the base of a parametric amplifier which could be operated in an external magnetic field. Overall, the work presented in this thesis demonstrates the potential of quantum paraelectric materials in the field of radio frequency (rf) measurements in a cryogenic environment to improve readout signals.

Appendix A

Wiring of a dry dilution refrigerator

This appendix contains information about the layout of a dry dilution refrigerator (Triton model, Oxford Instruments) and the cryogenic characterisation of a travelling wave parametric amplifier (TWPA from VTT, Finland). The wiring of two fridges and the noise temperature measurement of the TWPA are accomplished in collaboration with Patrick, while the fridge layout is designed by Edward.

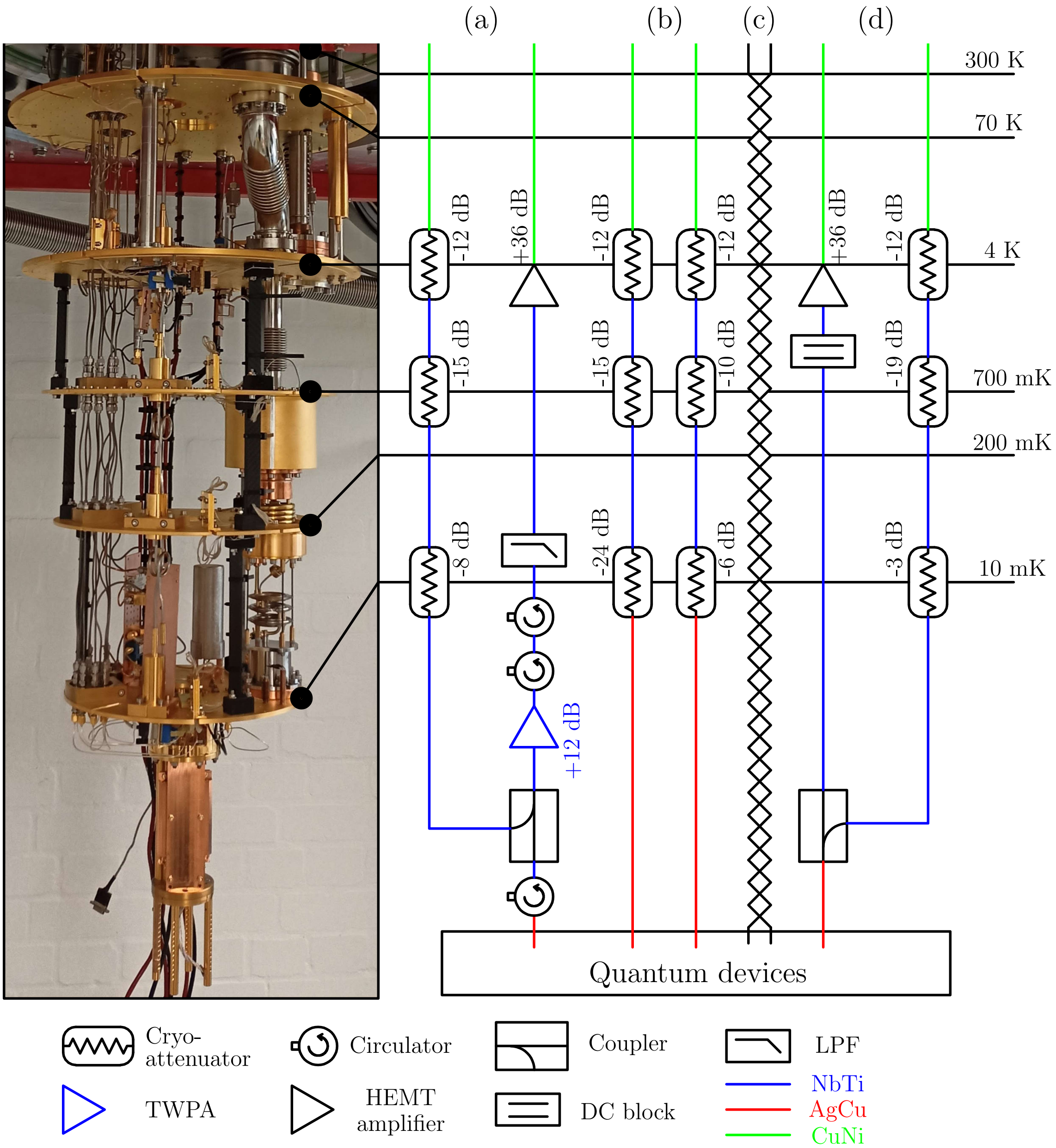

Figure A.1: Fridge layout. (a) Measurement with TWPA. (b) Radio frequency and microwave controls. (c) dc control and measurement. (d) Reflectometry setup.

Acronyms used in figure A.1: LPF: low pass filter; NbTi: semi-rigid niobium-titanium superconducting coaxial cable; AgCu: copper coaxial cable (with silver-plated inner conductor); CuNi: cupro nickel coaxial cable. **Labels for different thermal stages in figure A.1:** 300 K: room temperature; 70 K: pulse tube 1 (PT 1); 4 K: PT 2; 700 mK: still plate; 200 mK: cold plate; 10 mK: mixing chamber (MC) plate.

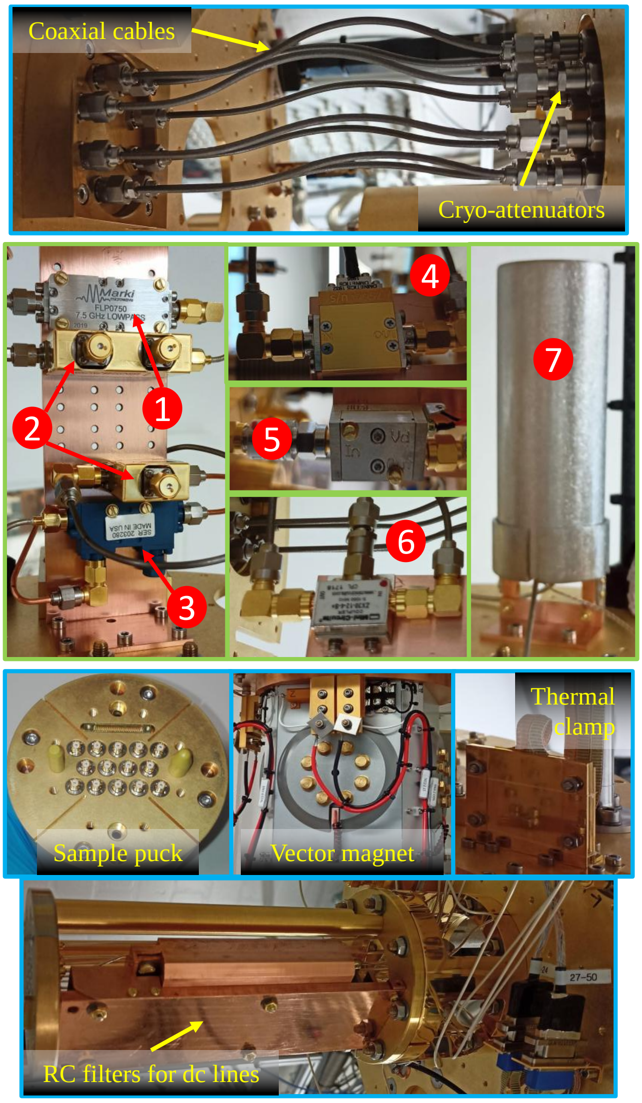

Figure A.2: Different parts inside the fridge. Mounted microwave components are (1) low pass filter, (2) circulator, (3) & (6) directional couplers, (4) & (5) HEMT (high electron mobility transistor) amplifiers and (7) Mu-metal magnetic shielding for TWPA.

A.1 Noise temperature characterisation of a TWPA

The Y-factor technique is used to characterise the noise temperature of a TWPA. A thermal noise of a specific temperature from a noise source (as shown in figure A.3a), whose temperature is adjusted in a controlled way through the fridge circuitry, is sent to the input of a TWPA. The linear noise power from the output of the TWPA through an amplification chain is measured in a spectrum analyser for different temperatures of the noise source (T_{NS}), for a noise spectrum over a range between 3.5 and 8 GHz. Figure A.3b is an example for a specific frequency of 5 GHz.

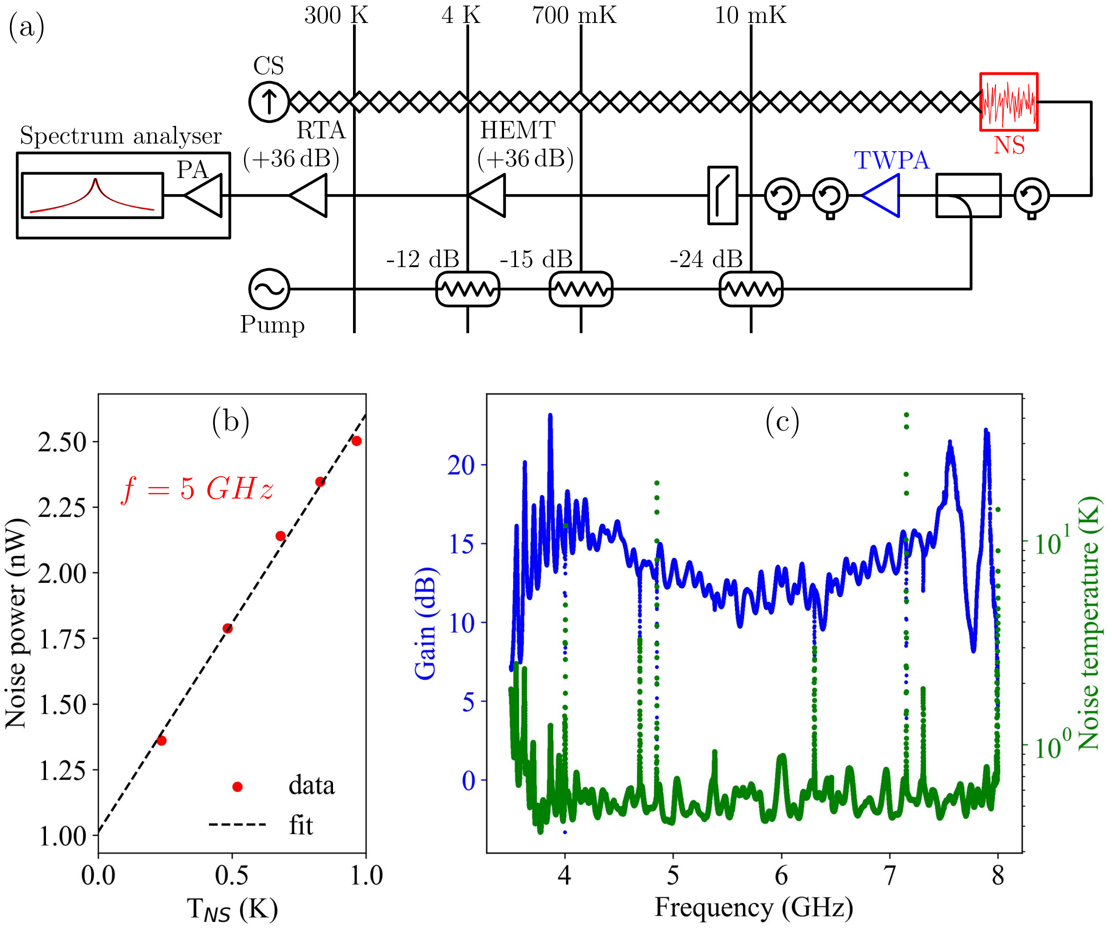

Figure A.3: Overview of the noise temperature measurement of a TWPA. (a) Experimental setup [Acronyms: PA (pre-amplifier), RTA (room temperature amplifier), NS (noise source), CS (current source)]. (b) Linear noise power as a function of the temperature of the noise source at a specific frequency (f) of 5 GHz. (c) Gain profile and noise temperature of the TWPA over the working bandwidth.

According to the Y-factor method, the slope of the fit line (in figure A.3b) is kBG_{DUT} [where, k = Boltzmann constant, B = measurement bandwidth (1 MHz) and G_{DUT} = gain of the device under test (DUT)] and the intercept equals the noise power of the DUT ($N_{\mathrm{DUT}} = kT_{\mathrm{DUT}}BG_{\mathrm{DUT}}$, where, T_{DUT} = noise temperature of the DUT). Therefore, the gain can be determined from the slope and sequentially the noise temperature can be derived from the intercept for a particular frequency.

Since the DUT includes other amplifiers in series with the TWPA (as shown in figure A.3a), to extract the gain and noise temperature of the TWPA, a similar measurement is performed while bypassing the TWPA. With an average gain of 12 dB within the working bandwidth, the TWPA maintains its noise temperature near 350 mK as shown in figure A.3c while the noise temperature of the HEMT amplifier is near 80 mK.

BLANK PAGE

Appendix B

Characterisation of a superconducting microwave resonator

A brief overview of the working principle of a superconducting resonator, especially a coplanar waveguide (CPW) structure, is described in this appendix. When a superconducting cavity is coupled to a 50 Ω matched transmission line, depending on the coupling condition, a standing wave is formed within the cavity and the shape of the waveform along the cavity length determines the nature of the resonator as shown in figure B.1.

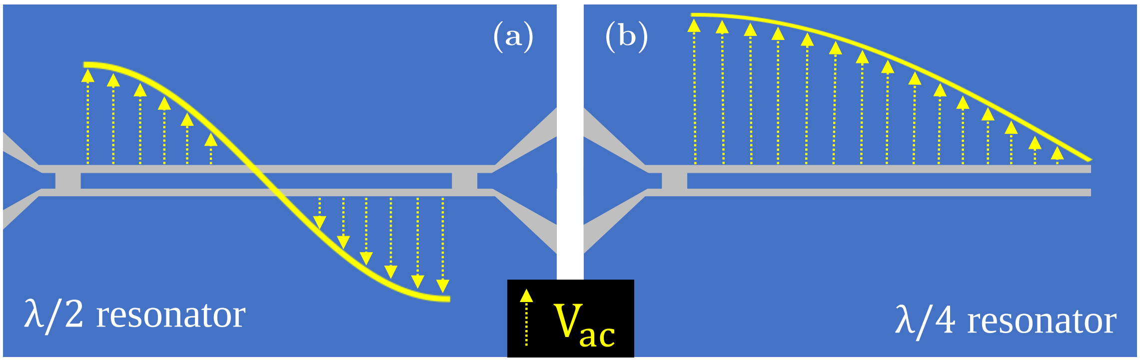

Figure B.1: Schematics of (a) a half-wave and (b) a quarter-wave CPW resonators. The voltage distribution (yellow line) at resonance is also drawn where the length of the arrow denotes the voltage amplitude of the ac signal.

The resonance occurs only when the cavity length matches half (or quarter) of the wavelength of the electromagnetic wave for the $\lambda/2$ (or $\lambda/4$) resonator. An important figure of merit for assessing the standard of a resonator is the loaded quality factor (Q_{L}) which is a function of the coupling strength [g: the ratio between the internal quality factor (Q_{int}) and the external quality factor (Q_{ext})].

- Undercoupling ($g < 1$): Q_{L} is governed by Q_{int}.
- Critical coupling ($g = 1$): $Q_{\mathrm{ext}} = Q_{\mathrm{int}} = 2Q_{\mathrm{L}}$.
- Overcoupling ($g > 1$): Q_{L} is governed by Q_{ext}.

Therefore, the coupling capacitor (C_{k}) plays a crucial role in the construction of a premium quality resonator.

Quality factor (Q)

$$Q = \omega \times \frac{\text{average energy stored}}{\text{energy loss per unit time}}$$

B.1 Relation between $C_{\mathbf{k}}$ and $Q_{\mathbf{ext}}$

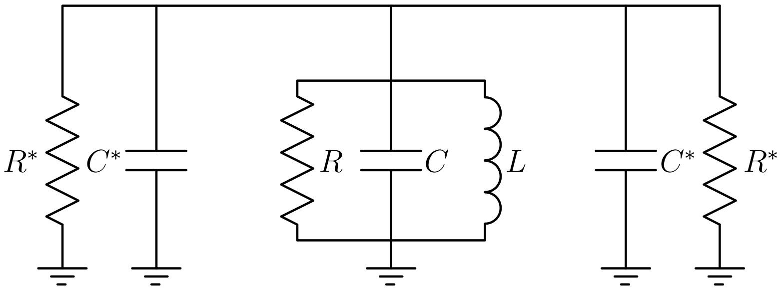

Figure B.2: Norton equivalent of symmetrically coupled parallel LCR resonator with two ports.

For symmetric input/output coupling as shown in figure B.2, the loaded quality factor ($Q_{\rm L}$) of a two-port circuit is given by

$$Q_{\rm L} = \omega^* \frac{C + 2C^*}{1/R + 2/R^*} \tag{B.1}$$

where,

$$\omega^* = \frac{1}{\sqrt{L(C + 2C^*)}} \simeq \frac{1}{\sqrt{LC}} \simeq \omega \ (\text{as } C^* << C) \tag{B.2}$$

Using equation B.2 in equation B.1 we have,

$$\frac{1}{Q_{\rm L}} = \frac{1}{\omega}[\frac{1}{RC} + \frac{2}{R^*C}] \tag{B.3}$$

Since the internal quality factor ($Q_{\rm int}$) of a parallel LCR resonator is defined as $Q_{\rm int} = \omega RC$ and $\frac{1}{Q_{\rm L}} = \frac{1}{Q_{\rm int}} + \frac{1}{Q_{\rm ext}}$, the external quality factor,

$$Q_{\rm ext} = \frac{\omega R^* C}{2} \tag{B.4}$$

where,

$$R^* = \frac{1 + \omega^2 C_\mathrm{k}^2 R_\mathrm{L}^2}{\omega^2 C_\mathrm{k}^2 R_\mathrm{L}} \tag{B.5}$$

At resonance, $R_\mathrm{L} = Z_0$ (characteristic impedance). Hence,

$$R^* = \frac{1 + \omega^2 C_\mathrm{k}^2 Z_0^2}{\omega^2 C_\mathrm{k}^2 Z_0} \tag{B.6}$$

Since $\omega^2 C_\mathrm{k}^2 Z_0^2 << 1$, $R^* = \frac{1}{\omega^2 C_\mathrm{k}^2 Z_0}$. From equation B.4, we have

$$Q_\mathrm{ext} = \frac{C}{2\omega C_\mathrm{k}^2 Z_0} \implies C_\mathrm{k}^2 = \frac{C}{2\omega Z_0 Q_\mathrm{ext}} \tag{B.7}$$

For a $\lambda/2$ coplanar waveguide resonator with two ports,

$$C = \frac{C_l l}{2} = \frac{\lambda/2}{2 Z_0 v_\mathrm{ph}} = \frac{\pi}{2\omega Z_0} \tag{B.8}$$

where, C_l is capacitance per unit length, l is the length of the resonator, phase velocity (v_ph) $= \frac{1}{\sqrt{L_l C_l}}$ and L_l is the inductance per unit length. Therefore from equation B.7, the mathematical relation between C_k and Q_ext can be described as

$$C_\mathrm{k} = \frac{\sqrt{\pi/Q_\mathrm{ext}}}{2\omega Z_0} \tag{B.9}$$

B.2 Device design and experimental setup

The device consists of a square wave-like strip-line and a meander-shaped CPW resonator made of 170 nm thick aluminium (Al) film (deposited in an electron beam evaporator) on a highly resistive silicon chip with silicon dioxide termination. The length of the resonator is approximately 13 mm. Therefore, according to $f_0 = \frac{c}{\sqrt{\varepsilon_\mathrm{eff}} \times 2l}$, the resonance frequency can be predicted near 5.05 GHz with $\varepsilon_\mathrm{eff} \simeq 5$ (simulated in ANSYS) [80]. The strip-line is used to determine the critical temperature of the superconducting thin film, while the resonator is characterised at 10 mK to study the microwave properties.

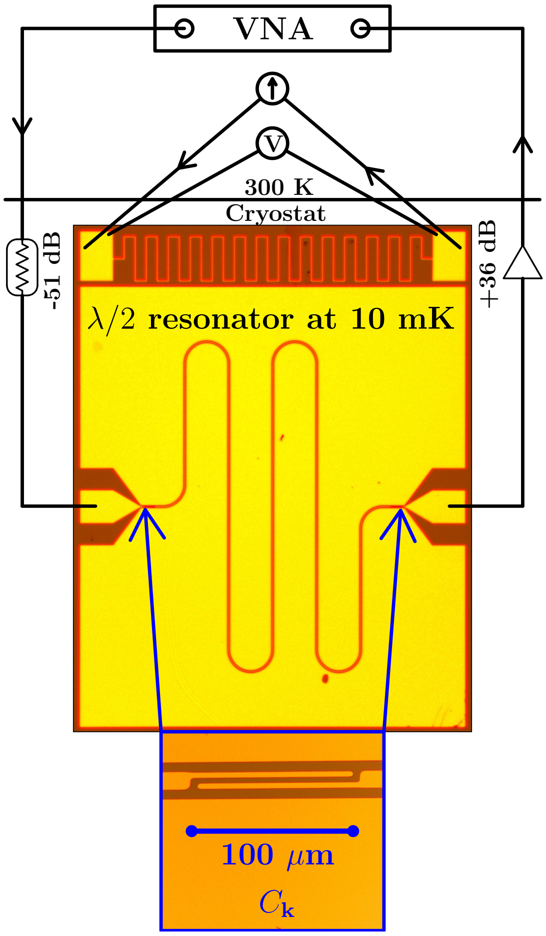

Figure B.3: Two-ports transmission measurement setup. The chip contains a $\lambda/2$ CPW resonator and a strip-line. The strip-line is configured into a four-probes measurement to find out the critical temperature of the thin film while the resonator is characterised at 10 mK using a vector network analyser (VNA). The resonator is symmetrically coupled to the input and the output lines through a finger capacitor (C_k).

B.3 Cryogenic characterisation

The resistance measurement (I-V characteristics) of the thin film (Al) is carried out using the square wave-shaped strip-line during the cool-down to determine the critical temperature (T_C). As shown in figure B.4a, for a specific current, the voltage decreases with temperature and at 1.2 K suddenly drops to zero. This indicates that the resistance of the thin film becomes zero at and below 1.2 K. Therefore, T_C of the film is 1.2 K where the transition occurs from a normal conducting state to a superconducting state. The residual resistance ratio ($RRR = \frac{R_{292\,\mathrm{K}}}{R_{2\,\mathrm{K}}}$, where $R_{292\,\mathrm{K}}$ and $R_{2\,\mathrm{K}}$ are resistances at 292 K and 2 K) is measured approximately 6 which defines the quality (purity and thermal conductivity) of the superconducting film.

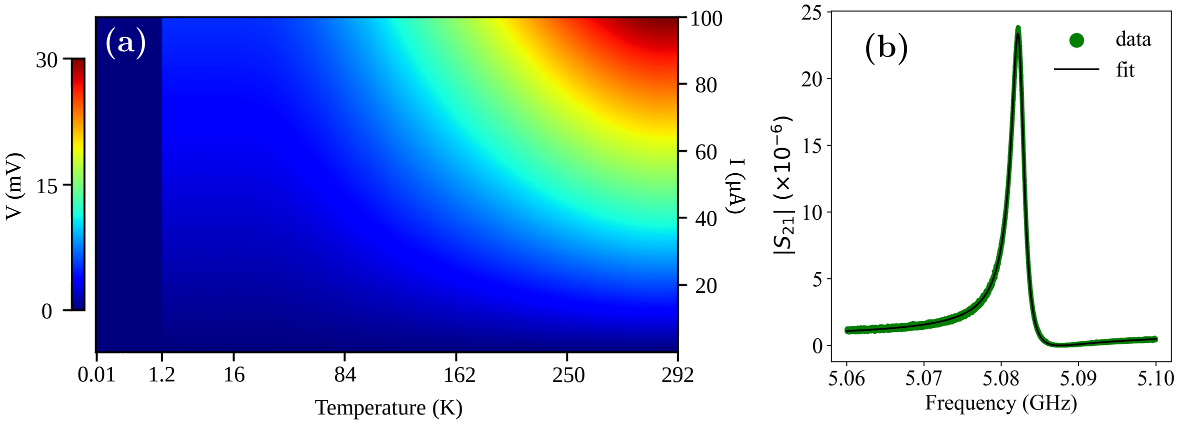

Figure B.4: Initial characterisation of the superconducting resonator. (a) I-V characteristics of the square wave-like strip-line at different temperatures. (b) Resonance peak in transmission coefficient (S_{21}) measurement. The fit is done using equation B.10.

At the base temperature ($\sim$ 10 mK), the transmission coefficient (S_{21}) of the resonator is measured and, as expected, the resonance frequency f_0 is found at 5.081 GHz. As shown in figure B.4b, the shape of the resonance peak is distorted from the Lorentzian shape to a asymmetric line-shape due to the presence of a Fano resonance [91, 92]. The most probable reason for the Fano resonance is the presence of a parallel parasitic path between the input and the output ports with a flat frequency response. This leads to a significant reduction of Q_L due to the resistive loss from the normal-conducting PCB and dissipation in the substrate. However, the asymmetric line-shape can be fit with the following function [93].

$$|S_{21}| = \frac{(\frac{f-f_0}{g}+q)^2}{(\frac{f-f_0}{g})^2+1} \times H + \sigma_0 + t \times f \tag{B.10}$$

where, f = frequency, f_0 = resonance frequency, g = curve width, q = asymmetric factor,H = gain parameter, σ_0 = an offset, $t \times f$ = frequency dependent part of the baseline. The Q_L of the resonator is approximately 750 derived from

$$Q_\mathrm{L} = (1-\sqrt{|q|})\frac{f_0}{2g\sqrt{\sqrt{2}-1}} + \sqrt{|q|}\frac{f_0^2+g^2}{2gf_0} \tag{B.11}$$

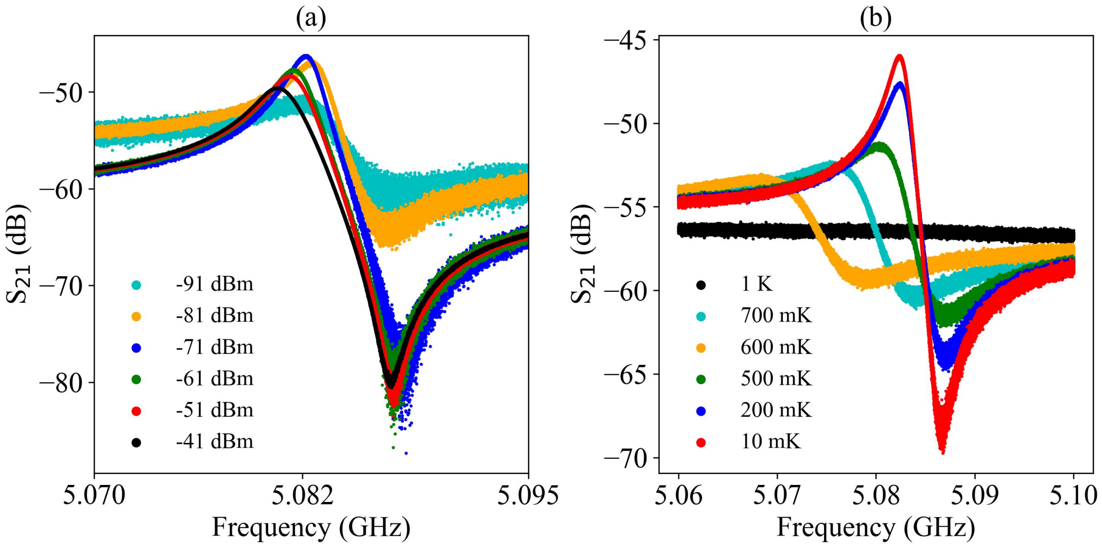

Figure B.5: (a) Input power and (b) temperature dependence of the quality of the resonance peak.

Figure B.5a depicts the power dependence of the loaded quality factor and the line-shape of the resonance peak at 10 mK. When the power at the input of the resonator is −71 dBm, the resonance peak is the strongest. Further increase in input power degrades the quality of the resonance peak. Moreover, below −71 dBm the quality is also poor. This can be explained by an well established loss mechanism at low power and low temperatures, where defects or two-level systems (TLSs) in the resonator dielectric absorb microwave photons, resulting in power loss [94].

The resonance frequency and the loaded quality factor also depend on the temperature below the critical temperature (T_C) of the superconducting thin film (Al). As the temperature approaches zero, the quasiparticle excitations become fewer, reducing the losses. This is why the distortion in the line shape disappears and the resonance peak becomes prominent as the temperature is reduced to 10 mK from 1 K, as shown in figure B.5b.

BLANK PAGE

Appendix C

Fabrication recipe

In this appendix, I have described the fabrication recipes that I used to make the devices discussed in chapter 3, chapter 4, and chapter 5. For the fabrication of my devices, I used the nanofabrication facilities of Lancaster Quantum Technology Centre.

C.1 Generic photolithography recipe

- **Cleaning:** Sonicate for 2 min in acetone, spray nitrogen. Sonicate for 2 min in isopropanol (IPA), spray nitrogen (N_2). Bake for 2 min at 110 °C.
- **1st layer spin coating:** Spin LOR3A photo-resist for 30 s at 3000 rpm. Bake for 5 min at 170 °C.
- **2nd layer spin coating:** Spin S1813 photo-resist for 45 s at 6000 rpm. Bake for 2 min at 118 °C.
- **Exposing:** Write the design pattern using a PicoMaster 100 laser writer with the following parameters:
  Exposure energy = 150 mJ/cm^2; Step resolution = 225 nm; Spot size = 550 nm; Laser power = 130 μW (for SiO_2/Si), 200μW (for $SrTiO_3$ and $KTaO_3$).
- **Developing:** Develop for 30 s in MFCD-26 developer, rinse in water. Bake for 5 min at 125 °C. Develop for 45 s in MFCD-26 developer, rinse in water. Bake for 5 min at 125 °C.

C.2 Fabrication details for device in chapter 3

- **Photo-lithography:** Follow the bilayer coating recipe and define the design pattern using the laser writer as described in section C.1.
- **Metal deposition:** Evaporate in Moorfield thermal evaporator
  10 nm titanium (Ti) at 1 Å/s
  100 nm gold (Au) at 7.5 Å/s

- **Lift off:** Dip in Remover-1165 for overnight. Rinse with acetone and IPA. Spray N_2.

C.3 Fabrication details for device in chapter 4

C.3.1 Device on $SrTiO_3$

The device was fabricated on a 10 mm×10 mm $SrTiO_3$ chip following the same recipe as mentioned in section C.2.

C.3.2 Device on SiO_2/Si

- **Metal deposition:** 165 nm thick niobium film sputtered at the cleanroon in University College London by Dr. Ed Romans' group.
- **Photo-lithography:** Follow the same recipe as section C.1 with a single layer of S1813 resist coating.
- **Dry etch:** Etch Nb with a rate of 55 nm/min in Oxford Instruments Reactive Ion Etcher (RIE). The gas used : SF_6 (40 sccm) + Ar (10 sccm). O_2 ashing (40 sccm) for 3 min to remove any residual resist from the etched surface.
- **Cleaning:** Dip in Remover-1165 at 75 °C for 2 min. Rinse in acetone and IPA. Spray N_2.

C.4 Fabrication details for device in chapter 5

- **Photo-lithography:** Follow the bi-layer spin coating recipe from section C.1.
- **Metal deposition:** Evaporate 200 nm thick aluminium (Al) in a Moorfield electron beam evaporator with a rate of 5 Å/s on a $KTaO_3$ chip.
- **Lift off:** Dip in Remover-1165 for overnight. Rinse with acetone and IPA. Spray N_2.

C.5 Specification of the substrates

- **$SrTiO_3$:**

  Manufactured by SurfaceNet [UK distributor : PI-KEM Limited]

  TiO_2-terminated single-crystal $SrTiO_3$

  Crystal orientation: (001)

  Dimension: 10 mm×10 mm×0.5 mm

  One side epi polished

  Dielectric constant: 300 at room temperature

- **$KTaO_3$:**

  Manufactured by SurfaceNet [UK distributor : PI-KEM Limited]

  Single-crystal $KTaO_3$

  Crystal orientation: (001)

  Dimension: 10 mm×10 mm×0.5 mm

  one side epi polished

- **Si/SiO_2:**

  Manufactured by inseto

  1 µm thick SiO_2-terminated 0.5 mm thick Si wafer

  Resistivity: $>$ 10,000 Ω-cm

Appendix D

Electrostatic simulation

This appendix provides a MATLAB code for the two dimensional electrostatic simulation for finding the change in dielectric constant with different voltages applied on the central strip-line of a coplanar waveguide resonator.

```
% MATLAB Simulation for GROUND-VOLTAGE-GROUND configuration :-
d1 = 500E-6; % x coordinate of the box
d2 = 500E-6; % y coordinate of the box
d3 = 0.2E-6; % width of the blocks
M = 3E-6; % max mesh size
% Create a model :-
emagmodel = createpde(‘electromagnetic’,‘electrostatic’);
% Draw a geometry with multiple shapes :-
% Draw each shape :-
R1 = [3,4,-d1,d1,d1,-d1,0,0,d2,d2]’;
R2 = [3,4,-d1,d1,d1,-d1,0,0,-d2,-d2]’;
R3 = [3,4,-5E-6,5E-6,5E-6,-5E-6,0,0,d3,d3]’;
R4 = [3,4,-d1,-11.6E-6,-11.6E-6,-d1,0,0,d3,d3]’;
R5 = [3,4,d1,11.6E-6,11.6E-6,d1,0,0,d3,d3]’;
% Make the length of the row of all the shapes equal :-
R2 = [R2;zeros(length(R1) - length(R2),1)];
R3 = [R3;zeros(length(R1) - length(R3),1)];
R4 = [R4;zeros(length(R1) - length(R4),1)];
R5 = [R5;zeros(length(R1) - length(R5),1)];
% Combine all the geometries :-
gm = [R1,R2,R3,R4,R5];
sf = ‘(R1+R2)-(R3+R4+R5)’;
ns = char(‘R1’,‘R2’,‘R3’,‘R4’,‘R5’);
ns = ns’;
% Create the final geometry :-
```

```
g = decsg(gm,sf,ns);
geometryFromEdges(emagmodel,g);
% Plot the geometry :-
pdegplot(emagmodel,‘EdgeLabels’,‘on’,‘FaceLabels’,‘on’);
axis equal;
% Create the mesh :-
mesh = generateMesh(emagmodel,‘GeometricOrder’,‘quadratic’,‘Hmax’,M,‘Hmin’,1E-14);
% Find the mesh electents and nodes associated with each face :-
Ef1 = findElements(mesh,‘region’,‘Face’,1);
Ef2 = findElements(mesh,‘region’,‘Face’,2);
Nf1 = findNodes(mesh,‘region’,‘Face’,1);
Nf2 = findNodes(mesh,‘region’,‘Face’,2);
% Plot the mesh with/without Node and Element numbers :-
figure;
pdemesh(mesh,‘ElementLabels’,‘off’);
hold on;
pdemesh(mesh.Nodes,mesh.Elements(:,Ef1),‘EdgeColor’,‘r’,”ElementLabels”,”off” ,”NodeLabels”,”off”);
hold on;
pdemesh(mesh.Nodes,mesh.Elements(:,Ef2),‘EdgeColor’,‘b’,”ElementLabels”,”off” ,”NodeLabels”,”off”);
% Define material properties :-
emagmodel.VacuumPermittivity = 8.8541878128E-12;
electromagneticProperties(emagmodel,‘RelativePermittivity’,1,‘Face’,2);
perm = @(region,state) 1+27400./power((1.+((state.ux. ˆ 2 + state.uy. ˆ 2)./71500 ˆ 2)),(1/3));
electromagneticProperties(emagmodel,‘RelativePermittivity’,perm,‘Face’,1);
% Define the boundary conditions :-
L1 = [];
```

```
for j = -3:1:5
        L1 = [L1,j];
end
L2 = [];
L3 = [];
for i = L1
        vv = 0; % Always should be zero for this particular model
        VOL = i;
        electromagneticBC(emagmodel,‘Voltage’,-vv,‘Edge’,[14 9 5]);
        electromagneticBC(emagmodel,‘Voltage’,VOL,‘Edge’,[11 15 4 3]);
        electromagneticBC(emagmodel,‘Voltage’,-vv,‘Edge’,[13 16 6]);
        % Solve the model :-
        R1 = solve(emagmodel);
        V1 = R1.ElectricPotential;
        EX = R1.ElectricField.Ex;
        EY = R1.ElectricField.Ey;
        E1_2 = EX. ^ 2 + EY. ^ 2;
        % Write a table containing all electric fields :-
        ep = [];
        for j = 1:length(mesh.Nodes)
            if mesh.Nodes(2,j)>0
                ep = [ep,1];
            end
            if mesh.Nodes(2,j)<=0
                E = sqrt(EX(j).^2 + EY(j).^2);
                Ep = 1.+27400./power((1.+power(E/71500,2.)),(1/3));
                ep = [ep,Ep];
            end
        end
```

```
figure;
pdeplot(emagmodel,‘XYData’,ep)
I = 0;
for i = 1:length(mesh.Elements(:,Ef1))
    T = [];
    ElementNumber = i;
    T = mesh.Elements(:,i)’;
    x = [];
    y = [];
    z = 0;
    for j = T
        x = [x,mesh.Nodes(1,j)];
        y = [y,mesh.Nodes(2,j)];
        E = sqrt(EX(j).^2 + EY(j).^2);
        Ep = 1.+27400./power((1.+power(E/71500,2.)),(1/3));
        Ep_E = E1_2(j).*Ep;
        z = z + Ep_E;
    end
    z = (z/6);
    Area = 0.5*abs(det([x(1),x(2),x(3);y(1),y(2),y(3);1,1,1]));
    I = I + z*Area;
end
for i = length(mesh.Elements(:,Ef1))+1:length(mesh.Elements)
    T = [];
    ElementNumber = i;
    T = mesh.Elements(:,i)’;
    x = [];
    y = [];
    z = 0;
```

```
            for j = T
                x = [x,mesh.Nodes(1,j)];
                y = [y,mesh.Nodes(2,j)];
                Ep = 1;
                Ep_E = E1_2(j).*Ep;
                z = z + Ep_E;
            end
            z = (z/6);
            Area = 0.5*abs(det([x(1),x(2),x(3);y(1),y(2),y(3);1,1,1]));
            I = I + z*Area;
        end
        UpL = (I*8.854E-12)/2
        CpL = (I*8.854E-12)/VOL^2
        L2 = [L2,CpL];
        L3 = [L3,UpL];
end
```

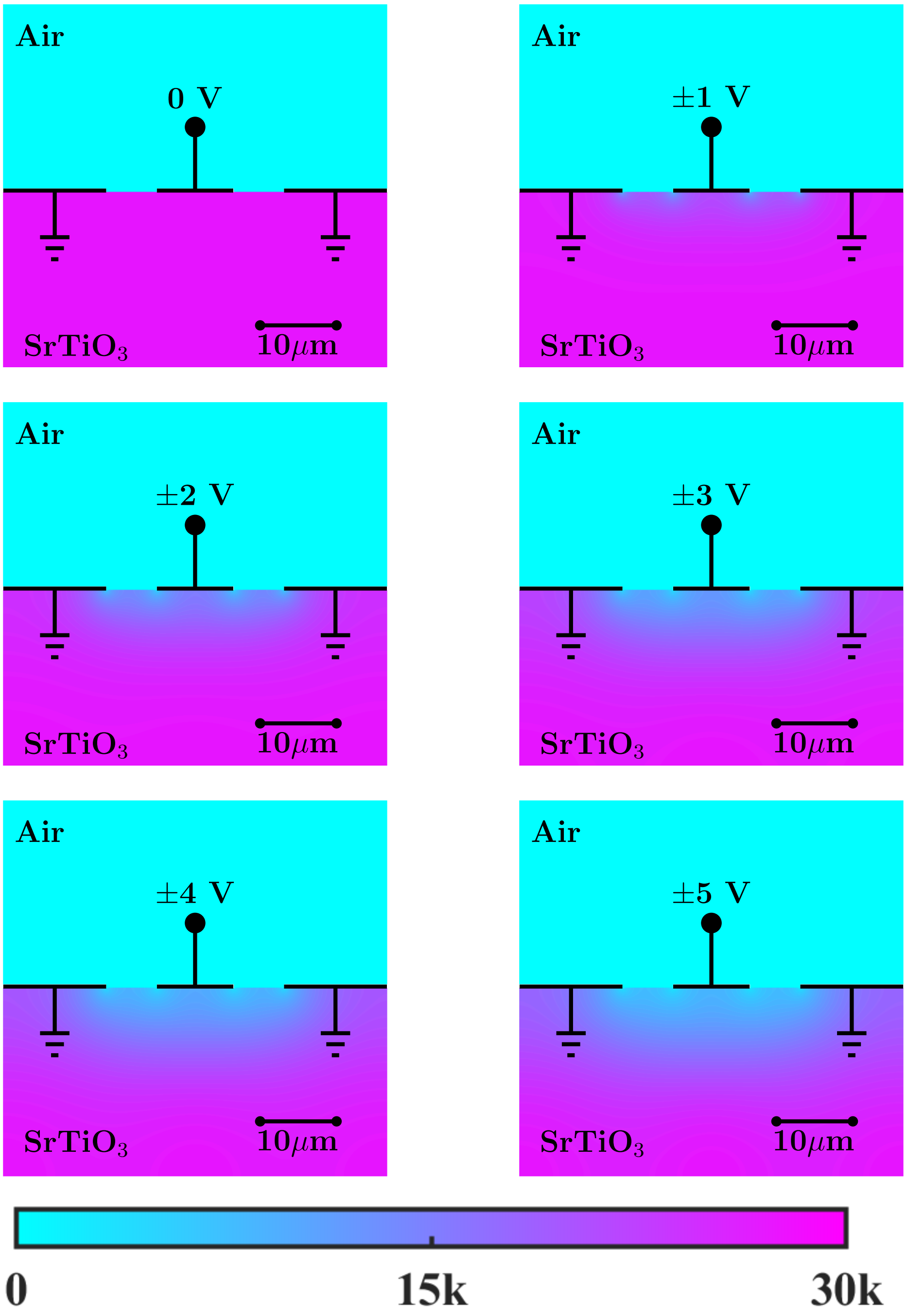

Figure D.1: The impact of different voltages on the relative permittivity of $SrTiO_3$. The colour bar at the bottom represents the value of ϵ_{STO}.

BLANK PAGE

References

[1] C. Macklin et al. “A near–quantum-limited Josephson traveling-wave parametric amplifier”. In: *Science* 350 (6258 Oct. 2015), pp. 307–310. ISSN: 0036-8075. DOI: 10.1126/science.aaa8525. URL: https://www.science.org/doi/10.1126/science.aaa8525.

[2] Tanay Roy et al. “Broadband parametric amplification with impedance engineering: Beyond the gain-bandwidth product”. In: *Applied Physics Letters* 107 (26 Dec. 2015). ISSN: 0003-6951. DOI: 10.1063/1.4939148. URL: https://pubs.aip.org/apl/article/107/26/262601/235920/Broadband-parametric-amplification-with-impedance.

[3] Jose Aumentado. “Superconducting Parametric Amplifiers: The State of the Art in Josephson Parametric Amplifiers”. In: *IEEE Microwave Magazine* 21 (8 Aug. 2020), pp. 45–59. ISSN: 1527-3342. DOI: 10.1109/MMM.2020.2993476. URL: https://ieeexplore.ieee.org/document/9134828/.

[4] Martina Esposito et al. “Perspective on traveling wave microwave parametric amplifiers”. In: *Applied Physics Letters* 119 (12 Sept. 2021). ISSN: 0003-6951. DOI: 10.1063/5.0064892. URL: https://pubs.aip.org/apl/article/119/12/120501/1065091/Perspective-on-traveling-wave-microwave-parametric.

[5] P. Krantz et al. “A quantum engineer’s guide to superconducting qubits”. In: *Applied Physics Reviews* 6 (2 June 2019). ISSN: 1931-9401. DOI: 10.1063/1.

5089550. URL: https://pubs.aip.org/apr/article/6/2/021318/570326/A-quantum-engineer-s-guide-to-superconducting.

[6] Slawomir Simbierowicz et al. "A flux-driven Josephson parametric amplifier for sub-GHz frequencies fabricated with side-wall passivated spacer junction technology". In: *Superconductor Science and Technology* 31 (10 Oct. 2018), p. 105001. ISSN: 0953-2048. DOI: 10.1088/1361-6668/aad4f2. URL: https://iopscience.iop.org/article/10.1088/1361-6668/aad4f2.

[7] Joydip Sarkar et al. "Quantum-noise-limited microwave amplification using a graphene Josephson junction". In: *Nature Nanotechnology* 17 (11 Nov. 2022), pp. 1147–1152. ISSN: 17483395. DOI: 10.1038/s41565-022-01223-z.

[8] Guilliam Butseraen et al. "A gate-tunable graphene Josephson parametric amplifier". In: *Nature Nanotechnology* 17 (11 Nov. 2022), pp. 1153–1158. ISSN: 17483395. DOI: 10.1038/s41565-022-01235-9.

[9] M. R. Vissers et al. "Low-noise kinetic inductance traveling-wave amplifier using three-wave mixing". In: *Applied Physics Letters* 108 (1 Jan. 2016). ISSN: 0003-6951. DOI: 10.1063/1.4937922. URL: https://pubs.aip.org/apl/article/108/1/012601/30805/Low-noise-kinetic-inductance-traveling-wave.

[10] L. Ranzani et al. "Kinetic inductance traveling-wave amplifiers for multiplexed qubit readout". In: *Applied Physics Letters* 113 (24 Dec. 2018). ISSN: 0003-6951. DOI: 10.1063/1.5063252. URL: https://pubs.aip.org/apl/article/113/24/242602/36444/Kinetic-inductance-traveling-wave-amplifiers-for.

[11] S. Chaudhuri et al. "Broadband parametric amplifiers based on nonlinear kinetic inductance artificial transmission lines". In: *Applied Physics Letters* 110 (15 Apr. 2017). ISSN: 0003-6951. DOI: 10.1063/1.4980102. URL: https://pubs.aip.org/apl/article/110/15/152601/32963/Broadband-parametric-amplifiers-based-on-nonlinear.

[12] Samuel Goldstein et al. “Four wave-mixing in a microstrip kinetic inductance travelling wave parametric amplifier”. In: *Applied Physics Letters* 116 (15 Apr. 2020). ISSN: 0003-6951. DOI: `10.1063/5.0004236`. URL: `https://pubs.aip.org/apl/article/116/15/152602/38118/Four-wave-mixing-in-a-microstrip-kinetic`.

[13] M. Malnou et al. “Three-Wave Mixing Kinetic Inductance Traveling-Wave Amplifier with Near-Quantum-Limited Noise Performance”. In: *PRX Quantum* 2 (1 Jan. 2021), p. 010302. ISSN: 2691-3399. DOI: `10.1103/PRXQuantum.2.010302`. URL: `https://link.aps.org/doi/10.1103/PRXQuantum.2.010302`.

[14] Kevin O’Brien et al. “Resonant Phase Matching of Josephson Junction Traveling Wave Parametric Amplifiers”. In: *Physical Review Letters* 113 (15 Oct. 2014), p. 157001. ISSN: 0031-9007. DOI: `10.1103/PhysRevLett.113.157001`. URL: `https://link.aps.org/doi/10.1103/PhysRevLett.113.157001`.

[15] Arpit Ranadive et al. “Kerr reversal in Josephson meta-material and traveling wave parametric amplification”. In: *Nature Communications* 13 (1 Apr. 2022), p. 1737. ISSN: 2041-1723. DOI: `10.1038/s41467-022-29375-5`. URL: `https://www.nature.com/articles/s41467-022-29375-5`.

[16] J. Stehlik et al. “Fast Charge Sensing of a Cavity-Coupled Double Quantum Dot Using a Josephson Parametric Amplifier”. In: *Physical Review Applied* 4 (1 July 2015), p. 014018. ISSN: 2331-7019. DOI: `10.1103/PhysRevApplied.4.014018`. URL: `https://link.aps.org/doi/10.1103/PhysRevApplied.4.014018`.

[17] Z. R. Lin et al. “Single-shot readout of a superconducting flux qubit with a flux-driven Josephson parametric amplifier”. In: *Applied Physics Letters* 103 (13 Sept. 2013). ISSN: 0003-6951. DOI: `10.1063/1.4821822`. URL: `https://pubs.aip.org/apl/article/103/13/132602/130068/Single-shot-readout-of-a-superconducting-flux`.

[18] Z.R. Lin et al. “Josephson parametric phase-locked oscillator and its application to dispersive readout of superconducting qubits”. In: *Nature Communications* 5 (1 July 2014), p. 4480. ISSN: 2041-1723. DOI: 10.1038/ncomms5480. URL: https://www.nature.com/articles/ncomms5480.

[19] S. Frasca et al. “Three-wave-mixing quantum-limited kinetic inductance parametric amplifier operating at 6 T near 1 K”. In: *Physical Review Applied* 21 (2 Feb. 2024), p. 024011. ISSN: 2331-7019. DOI: 10.1103/PhysRevApplied.21.024011. URL: https://link.aps.org/doi/10.1103/PhysRevApplied.21.024011.

[20] The MADMAX Working Group et al. “Dielectric Haloscopes: A New Way to Detect Axion Dark Matter”. In: *Physical Review Letters* 118 (9 Nov. 2016). ISSN: 10797114. DOI: 10.1103/PhysRevLett.118.091801. URL: http://arxiv.org/abs/1611.05865%20http://dx.doi.org/10.1103/PhysRevLett.118.091801.

[21] Junu Jeong et al. “Search for invisible axion dark matter with a multiple-cell haloscope”. In: *Physical Review Letters* 125 (22 Aug. 2020). ISSN: 10797114. DOI: 10.1103/PhysRevLett.125.221302. URL: http://arxiv.org/abs/2008.10141%20http://dx.doi.org/10.1103/PhysRevLett.125.221302.

[22] K. M. Backes et al. “A quantum enhanced search for dark matter axions”. In: *Nature* 590 (7845 Feb. 2021), pp. 238–242. ISSN: 0028-0836. DOI: 10.1038/s41586-021-03226-7. URL: https://www.nature.com/articles/s41586-021-03226-7.

[23] K. Wurtz et al. “A cavity entanglement and state swapping method to accelerate the search for axion dark matter”. In: (July 2021). URL: https://doi.org/10.1103/PRXQuantum.2.040350.

[24] A. Alsulami et al. “QSHS: An Axion Dark Matter Resonant Search Apparatus”. In: (Apr. 2025). URL: http://arxiv.org/abs/2504.12257.

[25] J. F. Schooley et al. "Dependence of the Superconducting Transition Temperature on Carrier Concentration in Semiconducting $SrTiO_3$". In: *Phys. Rev. Lett.* 14 (9 Mar. 1965), pp. 305–307. DOI: 10.1103/PhysRevLett.14.305. URL: https://link.aps.org/doi/10.1103/PhysRevLett.14.305.

[26] Dongbin Shin et al. "Quantum paraelectric phase of $SrTiO_3$ from first principles". In: *Physical Review B* 104 (6 Aug. 2021). ISSN: 24699969. DOI: 10.1103/PhysRevB.104.L060103.

[27] K. A. Müller and H. Burkard. "$SrTiO_3$: An intrinsic quantum paraelectric below 4 K". In: *Phys. Rev. B* 19 (7 Apr. 1979), pp. 3593–3602. DOI: 10.1103/PhysRevB.19.3593. URL: https://link.aps.org/doi/10.1103/PhysRevB.19.3593.

[28] P. Apostolidis et al. "Quantum paraelectric varactors for radiofrequency measurements at millikelvin temperatures". In: *Nature Electronics* 7 (9 Aug. 2024), pp. 760–767. ISSN: 2520-1131. DOI: 10.1038/s41928-024-01214-z. URL: https://www.nature.com/articles/s41928-024-01214-z.

[29] N. Ares et al. "Sensitive Radio-Frequency Measurements of a Quantum Dot by Tuning to Perfect Impedance Matching". In: *Physical Review Applied* 5 (3 Mar. 2016), p. 034011. ISSN: 2331-7019. DOI: 10.1103/PhysRevApplied.5.034011. URL: https://link.aps.org/doi/10.1103/PhysRevApplied.5.034011.

[30] Rafael S. Eggli et al. "Cryogenic hyperabrupt strontium titanate varactors for sensitive reflectometry of quantum dots". In: *Physical Review Applied* 20 (5 Nov. 2023), p. 054056. ISSN: 2331-7019. DOI: 10.1103/PhysRevApplied.20.054056. URL: https://link.aps.org/doi/10.1103/PhysRevApplied.20.054056.

[31] Yutian Wen et al. "Measuring carbon nanotube vibrations using a single-electron transistor as a fast linear amplifier". In: *Applied Physics Letters* 113 (15 Oct. 2018). ISSN: 0003-6951. DOI: 10.1063/1.5052185. URL: https:

//pubs.aip.org/apl/article/113/15/153101/35016/Measuring-carbon-nanotube-vibrations-using-a.

[32] Yutian Wen et al. “A coherent nanomechanical oscillator driven by single-electron tunnelling”. In: *Nature Physics* 16 (1 Jan. 2020), pp. 75–82. ISSN: 1745-2473. DOI: 10.1038/s41567-019-0683-5. URL: https://www.nature.com/articles/s41567-019-0683-5.

[33] David M. Pozar. *Microwave Engineering.* Wiley, 2012. DOI: ISBN:978-1-118-21363-6.

[34] Robert E. Collin. *Foundations for Microwave Engineering.* Wiley, 2001. DOI: ISBN:978-0-780-36031-0.

[35] Robert E. Collin. *The Optimum Tapered Transmission Line Matching Section.* 1956. DOI: 10.1109/JRPROC.1956.274938.

[36] R. W. Klopfenstein. *A Transmission Line Taper of Improved Design.* 2007. DOI: 10.1109/JRPROC.1956.274847.

[37] Harry E. Weaver. “Dielectric properties of single crystals of $SrTiO_3$ at low temperatures”. In: *Journal of Physics and Chemistry of Solids* 11 (1959), pp. 274–277. URL: https://api.semanticscholar.org/CorpusID:95911492.

[38] S. E. Rowley et al. “Ferroelectric quantum criticality”. In: *Nature Physics* 10 (5 May 2014), pp. 367–372. ISSN: 1745-2473. DOI: 10.1038/nphys2924. URL: https://www.nature.com/articles/nphys2924.

[39] Tobias Esswein and Nicola A. Spaldin. “Ferroelectric, quantum paraelectric, or paraelectric? Calculating the evolution from $BaTiO_3$ to $SrTiO_3$ to $KTaO_3$ using a single-particle quantum mechanical description of the ions”. In: *Physical Review Research* 4 (3 July 2022), p. 033020. ISSN: 2643-1564. DOI: 10.1103/PhysRevResearch.4.033020. URL: https://link.aps.org/doi/10.1103/PhysRevResearch.4.033020.

[40] Mitsuru Itoh and Ruiping Wang. "Quantum ferroelectricity in $SrTiO_3$ induced by oxygen isotope exchange". In: *Applied Physics Letters* 76 (2 Jan. 2000), pp. 221–223. ISSN: 0003-6951. DOI: 10.1063/1.125708. URL: https://pubs.aip.org/apl/article/76/2/221/518424/Quantum-ferroelectricity-in-SrTiO$_3$-induced-by.

[41] M. Itoh et al. "Ferroelectricity Induced by Oxygen Isotope Exchange in Strontium Titanate Perovskite". In: *Phys. Rev. Lett.* 82 (17 Apr. 1999), pp. 3540–3543. DOI: 10.1103/PhysRevLett.82.3540. URL: https://link.aps.org/doi/10.1103/PhysRevLett.82.3540.

[42] J. H. Haeni et al. "Room-temperature ferroelectricity in strained $SrTiO_3$". In: *Nature* 430 (7001 Aug. 2004), pp. 758–761. ISSN: 0028-0836. DOI: 10.1038/nature02773. URL: https://www.nature.com/articles/nature02773.

[43] Hideshi Fujishita et al. "Quantum paraelectric states in $SrTiO_3$ and $KTaO_3$: Barrett model, Vendik model, and quantum criticality". In: *Journal of the Physical Society of Japan* 85 (7 July 2016). ISSN: 13474073. DOI: 10.7566/JPSJ.85.074703.

[44] Richard G. Geyer et al. "Microwave dielectric properties of single-crystal quantum paraelectrics $KTaO_3$ and $SrTiO_3$ at cryogenic temperatures". In: *Journal of Applied Physics* 97 (10 May 2005). ISSN: 0021-8979. DOI: 10.1063/1.1905789. URL: https://pubs.aip.org/jap/article/97/10/104111/316711/Microwave-dielectric-properties-of-single-crystal.

[45] D. Davidovikj et al. "Quantum paraelectricity probed by superconducting resonators". In: *Physical Review B* 95 (21 June 2017), p. 214513. ISSN: 2469-9950. DOI: 10.1103/PhysRevB.95.214513. URL: http://link.aps.org/doi/10.1103/PhysRevB.95.214513.

[46] Nicolaas Bloembergen. *Nonlinear Optics*. 1996. DOI: https://doi.org/10.1142/3046.

[47] Y. R. Shen. *The Principles of Nonlinear Optics*. DOI: https://www.wiley.com/en-us/The+Principles+of+Nonlinear+Optics-p-9780471430803#download-product-flyer.

[48] Robert W. Boyd. *Nonlinear Optics*. 2008. DOI: https://www.sciencedirect.com/book/9780123694706/nonlinear-optics.

[49] Geoffrey New. *Introduction to Nonlinear Optics*. 2011. DOI: https://doi.org/10.1017/CBO9780511975851.

[50] A. Bienfait et al. "Reaching the quantum limit of sensitivity in electron spin resonance". In: *Nature Nanotechnology* 11 (3 Mar. 2016), pp. 253–257. ISSN: 1748-3387. DOI: 10.1038/nnano.2015.282. URL: https://www.nature.com/articles/nnano.2015.282.

[51] David M.P. Smith et al. "Low noise amplifier for radio astronomy". In: *International Journal of Microwave and Wireless Technologies* 5 (4 Aug. 2013), pp. 453–461. ISSN: 1759-0787. DOI: 10.1017/S1759078712000840. URL: https://www.cambridge.org/core/product/identifier/S1759078712000840/type/journal_article.

[52] C. Bockstiegel et al. "Development of a Broadband NbTiN Traveling Wave Parametric Amplifier for MKID Readout". In: *Journal of Low Temperature Physics* 176 (3-4 Aug. 2014), pp. 476–482. ISSN: 0022-2291. DOI: 10.1007/s10909-013-1042-z. URL: http://link.springer.com/10.1007/s10909-013-1042-z.

[53] M. A. Castellanos-Beltran and K. W. Lehnert. "Widely tunable parametric amplifier based on a superconducting quantum interference device array resonator". In: *Applied Physics Letters* 91 (8 Aug. 2007). ISSN: 0003-6951. DOI: 10.1063/1.2773988. URL: https://pubs.aip.org/apl/article/91/8/083509/326765/Widely-tunable-parametric-amplifier-based-on-a.

[54] N. Roch et al. "Widely Tunable, Nondegenerate Three-Wave Mixing Microwave Device Operating near the Quantum Limit". In: *Physical Review Letters* 108 (14 Apr. 2012), p. 147701. ISSN: 0031-9007. DOI: 10.1103/PhysRevLett.108.147701. URL: https://link.aps.org/doi/10.1103/PhysRevLett.108.147701.

[55] T. Yamamoto et al. "Flux-driven Josephson parametric amplifier". In: *Applied Physics Letters* 93 (4 July 2008). ISSN: 0003-6951. DOI: 10.1063/1.2964182. URL: https://pubs.aip.org/apl/article/93/4/042510/324175/Flux-driven-Josephson-parametric-amplifier.

[56] Luca Planat et al. "Understanding the Saturation Power of Josephson Parametric Amplifiers Made from SQUID Arrays". In: *Physical Review Applied* 11 (3 Mar. 2019), p. 034014. ISSN: 2331-7019. DOI: 10.1103/PhysRevApplied.11.034014. URL: https://link.aps.org/doi/10.1103/PhysRevApplied.11.034014.

[57] J. Y. Mutus et al. "Strong environmental coupling in a Josephson parametric amplifier". In: *Applied Physics Letters* 104 (26 June 2014). ISSN: 0003-6951. DOI: 10.1063/1.4886408. URL: https://pubs.aip.org/apl/article/104/26/263513/983058/Strong-environmental-coupling-in-a-Josephson.

[58] G. Liu et al. "Josephson parametric converter saturation and higher order effects". In: *Applied Physics Letters* 111 (20 Nov. 2017). ISSN: 0003-6951. DOI: 10.1063/1.5003032. URL: https://pubs.aip.org/apl/article/111/20/202603/34485/Josephson-parametric-converter-saturation-and.

[59] N. Bergeal et al. "Phase-preserving amplification near the quantum limit with a Josephson ring modulator". In: *Nature* 465 (7294 May 2010), pp. 64–68. ISSN: 0028-0836. DOI: 10.1038/nature09035. URL: https://www.nature.com/articles/nature09035.

[60] O. Yaakobi et al. "Parametric amplification in Josephson junction embedded transmission lines". In: *Physical Review B* 87 (14 Apr. 2013), p. 144301. ISSN:

1098-0121. DOI: 10.1103/PhysRevB.87.144301. URL: https://link.aps.org/doi/10.1103/PhysRevB.87.144301.

[61] Byeong Ho Eom et al. "A wideband, low-noise superconducting amplifier with high dynamic range". In: *Nature Physics* 8 (8 Aug. 2012), pp. 623–627. ISSN: 1745-2473. DOI: 10.1038/nphys2356. URL: https://www.nature.com/articles/nphys2356.

[62] M. T. Bell and A. Samolov. "Traveling Wave Parametric Amplifier based on a chain of Coupled Asymmetric SQUIDs". In: *Physical Review Applied* 4 (2 Sept. 2015). ISSN: 23317019. DOI: 10.1103/PhysRevApplied.4.024014. URL: http://dx.doi.org/10.1103/PhysRevApplied.4.024014.

[63] A. B. Zorin. "Josephson Traveling-Wave Parametric Amplifier with Three-Wave Mixing". In: *Physical Review Applied* 6 (3 Sept. 2016), p. 034006. ISSN: 2331-7019. DOI: 10.1103/PhysRevApplied.6.034006. URL: https://link.aps.org/doi/10.1103/PhysRevApplied.6.034006.

[64] Luca Planat. "Resonant and traveling-wave parametric amplification near the quantum limit". Theses. Université Grenoble Alpes [2020-....], June 2020. URL: https://theses.hal.science/tel-03137118.

[65] X. Zhou et al. "High-gain weakly nonlinear flux-modulated Josephson parametric amplifier using a SQUID array". In: *Physical Review B* 89 (21 June 2014), p. 214517. ISSN: 1098-0121. DOI: 10.1103/PhysRevB.89.214517. URL: https://link.aps.org/doi/10.1103/PhysRevB.89.214517.

[66] N. E. Frattini et al. "3-wave mixing Josephson dipole element". In: *Applied Physics Letters* 110 (22 May 2017). ISSN: 0003-6951. DOI: 10.1063/1.4984142. URL: https://pubs.aip.org/apl/article/110/22/222603/33972/3-wave-mixing-Josephson-dipole-element.

[67] Patrick Winkel et al. "Nondegenerate Parametric Amplifiers Based on Dispersion-Engineered Josephson-Junction Arrays". In: *Physical Review Applied* 13 (2 Feb. 2020), p. 024015. ISSN: 2331-7019. DOI: 10.1103/PhysRevApplied.13.

024015. URL: https://link.aps.org/doi/10.1103/PhysRevApplied.13.024015.

[68] C. Eichler et al. "Quantum-Limited Amplification and Entanglement in Coupled Nonlinear Resonators". In: *Physical Review Letters* 113 (11 Sept. 2014), p. 110502. ISSN: 0031-9007. DOI: 10.1103/PhysRevLett.113.110502. URL: https://link.aps.org/doi/10.1103/PhysRevLett.113.110502.

[69] B. Yurke et al. "Observation of parametric amplification and deamplification in a Josephson parametric amplifier". In: *Phys. Rev. A* 39 (5 Mar. 1989), pp. 2519–2533. DOI: 10.1103/PhysRevA.39.2519. URL: https://link.aps.org/doi/10.1103/PhysRevA.39.2519.

[70] T. C. White et al. "Traveling wave parametric amplifier with Josephson junctions using minimal resonator phase matching". In: *Applied Physics Letters* 106 (24 June 2015). ISSN: 0003-6951. DOI: 10.1063/1.4922348. URL: https://pubs.aip.org/apl/article/106/24/242601/27555/Traveling-wave-parametric-amplifier-with-Josephson.

[71] C. Eichler, D. Bozyigit, and A. Wallraff. "Characterizing quantum microwave radiation and its entanglement with superconducting qubits using linear detectors". In: *Physical Review A* 86 (3 Sept. 2012), p. 032106. ISSN: 1050-2947. DOI: 10.1103/PhysRevA.86.032106. URL: https://link.aps.org/doi/10.1103/PhysRevA.86.032106.

[72] Baleegh Abdo et al. "Josephson Amplifier for Qubit Readout". In: *Applied Physics Letters* 99 (16 Mar. 2011). ISSN: 00036951. DOI: 10.1063/1.3653473. URL: http://arxiv.org/abs/1103.1405%20http://dx.doi.org/10.1063/1.3653473.

[73] Philip Krantz et al. "Single-shot read-out of a superconducting qubit using a Josephson parametric oscillator". In: *Nature Communications* 7 (1 May 2016), p. 11417. ISSN: 2041-1723. DOI: 10.1038/ncomms11417. URL: https://www.nature.com/articles/ncomms11417.

[74] P. A. Franken et al. "Generation of Optical Harmonics". In: *Physical Review Letters* 7 (4 Aug. 1961), pp. 118–119. ISSN: 0031-9007. DOI: 10.1103/PhysRevLett.7.118. URL: https://link.aps.org/doi/10.1103/PhysRevLett.7.118.

[75] M. A. Castellanos-Beltran et al. "Amplification and squeezing of quantum noise with a tunable Josephson metamaterial". In: *Nature Physics* 4 (12 Dec. 2008), pp. 929–931. ISSN: 1745-2473. DOI: 10.1038/nphys1090. URL: https://www.nature.com/articles/nphys1090.

[76] J. M. Hornibrook et al. "Frequency multiplexing for readout of spin qubits". In: *Applied Physics Letters* 104 (10 Mar. 2014). ISSN: 0003-6951. DOI: 10.1063/1.4868107. URL: https://pubs.aip.org/apl/article/104/10/103108/130884/Frequency-multiplexing-for-readout-of-spin-qubits.

[77] Florian Vigneau et al. "Probing quantum devices with radio-frequency reflectometry". In: *Applied Physics Reviews* 10 (2 June 2023). ISSN: 1931-9401. DOI: 10.1063/5.0088229. URL: https://pubs.aip.org/apr/article/10/2/021305/2885320/Probing-quantum-devices-with-radio-frequency.

[78] *AWR Microwave Office*. URL: https://www.cadence.com/en_US/home/tools/system-analysis/rf-microwave-design.html.

[79] *Single layer planar spiral coil inductor calculator*. URL: https://www.circuits.dk/calculator_planar_coil_inductor.htm.

[80] *ANSYS Electronics Desktop*. URL: https://www.ansys.com/academic/students/ansys-electronics-desktop-student.

[81] Chen Ang and Zhi Yu. "dc electric-field dependence of the dielectric constant in polar dielectrics: Multipolarization mechanism model". In: *Physical Review B* 69 (17 May 2004), p. 174109. ISSN: 1098-0121. DOI: 10.1103/PhysRevB.69.174109. URL: https://link.aps.org/doi/10.1103/PhysRevB.69.174109.

[82] M. Göppl et al. "Coplanar waveguide resonators for circuit quantum electrodynamics". In: *Journal of Applied Physics* 104 (11 Dec. 2008). ISSN: 0021-8979. DOI: 10.1063/1.3010859. URL: https://pubs.aip.org/jap/article/104/11/113904/145728/Coplanar-waveguide-resonators-for-circuit-quantum.

[83] *Characteristic impedance of a CPW resonator*. URL: https://www.microwaves101.com/calculators/864-coplanar-waveguide-calculator.

[84] Alaeddin S. Abu-Abed and Robert G. Lindquist. "CAPACITIVE INTERDIGITAL SENSOR WITH INHOMOGENEOUS NEMATIC LIQUID CRYSTAL FILM". In: *Progress in Electromagnetics Research B* 7 (2008), pp. 75–87. URL: https://api.semanticscholar.org/CorpusID:18543028.

[85] R. P. Erickson et al. "Frequency Comb Generation in Superconducting Resonators". In: *Physical Review Letters* 113 (18 Oct. 2014), p. 187002. ISSN: 0031-9007. DOI: 10.1103/PhysRevLett.113.187002. URL: https://link.aps.org/doi/10.1103/PhysRevLett.113.187002.

[86] Wenyuan Zhang et al. "Microresonators Fabricated from High-Kinetic-Inductance Aluminum Films". In: *Physical Review Applied* 11 (1 Jan. 2019), p. 011003. ISSN: 2331-7019. DOI: 10.1103/PhysRevApplied.11.011003. URL: https://link.aps.org/doi/10.1103/PhysRevApplied.11.011003.

[87] Lukas Grünhaupt et al. "Granular aluminium as a superconducting material for high-impedance quantum circuits". In: *Nature Materials* 18 (8 Aug. 2019), pp. 816–819. ISSN: 1476-1122. DOI: 10.1038/s41563-019-0350-3. URL: https://www.nature.com/articles/s41563-019-0350-3.

[88] Anatoliy A. Savchenkov et al. "Tunable Optical Frequency Comb with a Crystalline Whispering Gallery Mode Resonator". In: *Physical Review Letters* 101 (9 Aug. 2008), p. 093902. ISSN: 0031-9007. DOI: 10.1103/PhysRevLett.101.093902. URL: https://link.aps.org/doi/10.1103/PhysRevLett.101.093902.

[89] P. Del'Haye et al. "Optical frequency comb generation from a monolithic microresonator". In: *Nature* 450 (7173 Dec. 2007), pp. 1214–1217. ISSN: 0028-0836. DOI: 10.1038/nature06401. URL: https://www.nature.com/articles/nature06401.

[90] J. M. Chavez Boggio et al. "Efficient Kerr soliton comb generation in micro-resonator with interferometric back-coupling". In: *Nature Communications* 13 (1 Mar. 2022), p. 1292. ISSN: 2041-1723. DOI: 10.1038/s41467-022-28927-z. URL: https://www.nature.com/articles/s41467-022-28927-z.

[91] Ilya Golokolenov et al. "Microwave single-Tone optomechanics in the classical regime". In: *New Journal of Physics* 23 (5 May 2021). ISSN: 13672630. DOI: 10.1088/1367-2630/abf983.

[92] X. Zhou et al. "On-chip Thermometry for Microwave Optomechanics Implemented in a Nuclear Demagnetization Cryostat". In: *Physical Review Applied* 12 (4 Oct. 2019). ISSN: 23317019. DOI: 10.1103/PhysRevApplied.12.044066.

[93] Maik Bertke et al. "Analysis of asymmetric resonance response of thermally excited silicon micro-cantilevers for mass-sensitive nanoparticle detection". In: *Journal of Micromechanics and Microengineering* 27 (6 June 2017), p. 064001. ISSN: 0960-1317. DOI: 10.1088/1361-6439/aa6b0d. URL: https://iopscience.iop.org/article/10.1088/1361-6439/aa6b0d.

[94] J. M. Hornibrook, E. E. Mitchell, and D. J. Reilly. "Superconducting Resonators with Parasitic Electromagnetic Environments". In: (Mar. 2012). URL: http://arxiv.org/abs/1203.4442.